Silicon quantum dots for optical applications

A THESIS
SUBMITTED TO THE FACULTY OF THE GRADUATE SCHOOL
OF THE UNIVERSITY OF MINNESOTA
BY

Jeslin J Wu

IN PARTIAL FULFILLMENT OF THE REQUIREMENTS
FOR THE DEGREE OF
DOCTOR OF PHILOSOPHY

Uwe R Kortshagen

August, 2015

Acknowledgements

This dissertation would not be possible without the help of all the amazing people I have interacted with throughout the years.

First and foremost, I thank my advisor, Professor Uwe Kortshagen, for giving me the freedom to pursue various (creative) projects and his guidance throughout my scientific endeavors. I would also like to thank my committee members, Professor Peter Bruggeman, Professor Stephen Campbell, and Professor Rusen Yang for their time and helpful feedback on my dissertation.

I thank my colleagues in the High Temperature and Plasma Lab for their friendship; without whom, this journey would have been a dull one. I would especially like to thank my office mates, Katelyn Schramke and Daryl Lee, for all the fun times we have shared. I am extremely grateful to Rebecca Anthony, David Rowe, and Jihua Yang for all the knowledge they have passed on to me; I would have been lost without their guidance in my first year as a Ph.D. student. I also thank Ting Chen for all the valuable scientific conversations we had over the last five years. I am appreciative of the help from the staff members in the Mechanical Engineering Department, the University of Minnesota CSE Shop, and Minnesota Nano Center.

A special thanks to (Dr.) Indraneel Sircar for his patience and encouragement during these tempestuous Ph.D. years; without whom, I would have struggled to find motivation to complete this dissertation. Most importantly, none of this would be possible without the love and support of my family. I am grateful to my parents and brothers for their belief in me and their unwavering support in all my pursuits. I thank my grandparents for inspiring me to become a best version of myself. To my family, I dedicate this work.

Dedication

To my family...

Abstract

Luminescent silicon quantum dots (SiQDs) are emerging as attractive materials for optoelectronic devices, third generation photovoltaics, and bioimaging. Their applicability in the real world is contingent on their optical properties and long-term environmental stability; and in biological applications, factors such as water solubility and toxicity must also be taken into consideration.

The aforementioned properties are highly dependent on the QDs' surface chemistry. In this work, SiQDs were engineered for the respective applications using liquid-phase and gas-phase functionalization techniques. Preliminary work in luminescent downshifting for photovoltaic systems are also reported.

Highly luminescent SiQDs were fabricated by grafting unsaturated hydrocarbons onto the surface of hydrogen-terminated SiQDs via thermal and photochemical hydrosilylation. An industrially attractive, all gas-phase, nonthermal plasma synthesis, passivation (aided by photochemical reactions), and deposition process was also developed to reduce solvent waste.

With photoluminescence quantum yields (PLQYs) nearing 60 %, the alkyl-terminated QDs are attractive materials for optical applications. The functionalized SiQDs also exhibited enhanced thermal stability as compared to their unfunctionalized counterparts, and the photochemically-hydrosilylated QDs further displayed photostability under UV irradiation.

These environmentally-stable SiQDs were used as luminescent downshifting layers in photovoltaic systems, which led to enhancements in the blue photoresponse of heterojunction solar cells. Furthermore, the QD films demonstrated antireflective properties, improving the coupling efficiency of sunlight into the cell.

For biological applications, oxide, amine, or hydroxyl groups were grafted onto the surface to create water-soluble SiQDs. Luminescent, water-soluble SiQDs were produced in by microplasma treating the QDs in water. Stable QYs exceeding 50 % were obtained. Radical-based and catalytic hydrosilylation reactions were also investigated to engineer individually-dispersed SiQDs in water.

The results of this dissertation demonstrate the potential of SiQDs in optical applications. In the future, their application may lead to improvements in the efficiencies of photovoltaic devices and perhaps allow the cells to exceed the Shockley-Queisser limit. In biology, the stability of the SiQDs may allow long-term monitoring of biomolecules and perhaps lead to new discoveries.

Contents

List of Tables

List of Figures

Chapter 1

Introduction

Silicon has been the prevalent material in the semiconductor industry since the 1960s, and it will likely continue to play a significant role in our future (sustainable) technologies due to its earth abundance and low toxicity. In 1990, room-temperature light emission was observed from porous silicon (p-Si) (9), which further widened the range of potential silicon-based applications. The luminescence is attributed to quantum confinement; at the nanoscale, when its size approaches its Bohr exciton radius, silicon starts to exhibit unique, size-tunable electronic and optical properties (10). Since its discovery, luminescent silicon nanocrystals (SiNCs) have attracted much attention in the semiconductor industry for applications in electronic and optoelectronic devices, biological systems, and photovoltaics (PV).

1.1 Luminescent silicon quantum dots

Electrons in bulk materials are free to move in continuous energy states. At sizes smaller than or on the order of the Bohr exciton radius ($\sim$ 5 nm), the excitons in a SiNC are confined in all three dimensions. Trapped in a "box", excited electrons can relax and recombine with the holes in the ground state, emitting a photon while doing so.

The exciton energy of the photon, E_x, is strongly dependent on the SiNC's band gap, E_g, which is a function of the particle diameter, d (Å). The band gap energy has

been calculated from Schrodinger's equations by Wang and Zunger (1; 2):

$$E_g(d) = 1.167 + \frac{88.34}{d^{1.37}}(eV) \tag{1.1}$$

Zunger *et al.* also established the Coulomb interaction energy, E_c, between the excited electrons and the holes plays a significant role on the exciton energy as well (2). Similar to the band gap energy, the Coulomb energy is also a function of particle size:

$$E_c(R) = \frac{1.786}{\epsilon_s(R)R} \tag{1.2}$$

where ϵ_s is the screening dielectric constant, which is expressed as a function of R, the particle radius, in angstroms:

$$\epsilon_s(R) = 1 + \frac{\epsilon_b - 1}{1 + (6.9/R)^{1.37}} \tag{1.3}$$

Combining the bandgap energy and Coulomb interaction energy, the exciton energy of a photon can be estimated as follows:

$$E_x(R) = E_g(R) - E_c(R) - 0.248E_{Ry} \tag{1.4}$$

where E_{Ry} is the correlation energy correction ≈ 8.18 meV, E is the energy in Hartree, and R is the particle radius in Bohr radius.

Using the equations above, the size dependence of the exciton energy, specifically the emission wavelength, of SiNCs is plotted in Figure 1.1a. At sizes close to its Bohr radius, the SiNC emits in the red and near-infrared. However, as its size decreases, the emission blueshifts; blue emission can be achieved at ~ 2 nm.

1.2 Potential applications

1.2.1 Light-emitting devices

Lighting is one of the major consumers of electricity. In 2014, it comprised more than 11 % of electricity consumption in the U.S. residential and commercial sectors (11). To reduce energy consumption, investments have been made into the research and development of new lighting technologies to replace incandescent, halogen, or fluorescent lamps. Recently, the efficiencies of light-emitting devices (LEDs) have surpassed that of

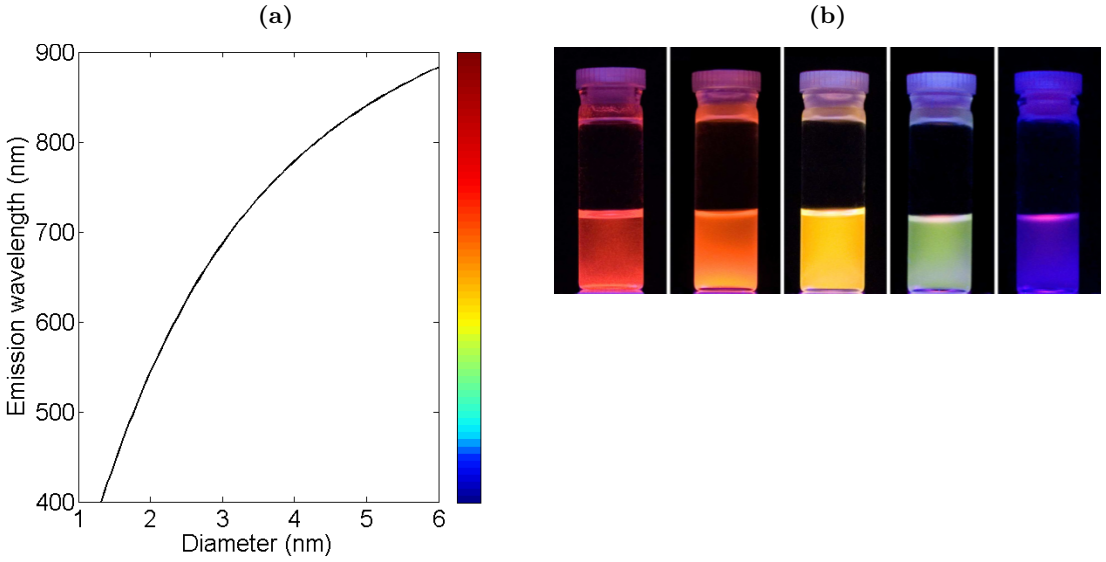

Figure 1.1: (a) Emission wavelength of SiNCs as a function of size. Modeled using equations from (1; 2). (b) Picture of size-tunable visible emission from colliodal SiNCs. Peak luminescence wavelength blue-shifts with decreasing NC size. Image taken from (3).

the conventional technologies. Recent developments by Isamu Akasaki, Hiroshi Amano, and Shuji Nakamura in blue InGaN LEDs have led to a breakthrough in lighting technologies. The advent of blue LEDs is vital in the production of the desired white LEDs for residential and commercial use.

White LEDs can be produced by mixing differently colored LEDs or using phosphors that can be photoactivated by a blue LED. By exploiting the size-tunable visible emission from silicon quantum dots (SiQDs) (Figure 1.1b), it is feasible to fabricate a white LED using a single material.

Quantum dot-based LEDs (QD-LEDs) have improved in external quantum efficiencies from 0.01 % to 18 % in the last 20 years (12). SiNC-based organic LEDs (OLEDs) with emissions in the near infrared (NIR) have demonstrated external quantum efficiencies (EQEs) up to 8.6 % (13; 14). Recently, improved coupling between the quantum dot and charge transport layers have significantly enhanced the efficiencies of QD-LEDs. Mashford et al. reported 18 % EQE from inorganic-organic hybrid LEDs and colloidal

CdSe-CdS core-shell QDs (15).

1.2.2 Photovoltaics

The world's energy demands is estimated to increase by more than 50 % in the next 20 years. The consequential doubling of greenhouse gas emissions detrimental to the earth (16). Renewable energy technologies are necessary to curb the negative impact of our energy demands. Solar photovoltaic (PV) has seen one of the largest growth in energy capacity in the last 5 years (17); however, they maintain as one of the more expensive power generation sources (18)—predominately a result of their low efficiencies and high manufacturing costs.

The efficiency of a photovoltaic (PV) device is constrained by thermodynamic losses. The maximum power conversion efficiency of a single-junction crystalline silicon solar cell under AM1.5G sun is $\sim$ 33 % (19). Almost 50 % of the losses occur due to the cell's inability to effectively convert incident high-energy photons to electrons (20). Excess energy greater than the semiconductor bandgap are lost through phonon emission, and energy is also lost as electron and holes recombine radiatively at the cell's surface. These losses can be overcome by taking advantage of spectrum conversion systems that modify the energy of incoming photons. As these are purely optical systems, no modification to the active layer is needed.

Luminescent downshifting

Silicon nanocrystals acting as luminescent downshifters (LDS) serve as a means to reduce radiative recombination losses. The LDS layer absorbs high-energy photons that are ineffectively used by the cell and emits them at a lower energy where the cell has a higher power conversion efficiency. Almost 10 % increase in EQE has been observed with the use of fluorescent dyes on CdTe solar cells (21). Other groups have reported enhanced internal quantum efficiencies with the application of SiNC LDS systems (22; 23). However, despite being a simple technique for improving PV performance, implementation of the LDS system is hindered by increased cell reflection from the LDS layer that can negate the LDS effects.

Carrier multiplication

Further increase in solar cell performance can be attained by harnessing the SiNC's capacity for generating multiple excitons for the absorption of a single photon in a process known as carrier multiplication (CM). Carrier multiplication has been reported in quantum dots, such as PbSe and PbS NCs, following the absorption of photons with energy that is at least twice the NCs' bandgap (24; 25; 26; 27; 28). While early work showed high CM quantum yields (29; 30), or number of excitons generated per absorbed photon, recent work with improved theoretical calculations and experimental methods indicate that CM efficiencies are lower than originally reported (31; 32). The low CM yields and high activation threshold energies diminishes its appeal as a solution for enhancing solar cell efficiencies.

Recently, a new CM mechanism has been observed in SiNCs embedded in a SiO_2 matrix that makes it an attractive material for PV devices. Contrary to previous findings that showed multiple excitons forming in a single NC, Gregorkiewicz *et al.* revealed, through ultrafast pump-probe spectroscopy, that multiple excitons are generated in neighboring NCs that are spatially-separated upon the absorption of a single high-energy photon (33; 34). This mechanism not only results in a reduction in threshold energy, but in a step-like enhancement of quantum yield that increases at a faster rate with increased energy. With such a mechanism, the maximum PV power conversion efficiency of ~ 44 % calculated by Beard *et al.* may be attainable (35).

1.2.3 Biological systems

Fluorescence imaging is an important technique in the study and analysis of biomolecules and has played an important role in biological research, gene technology, medical diagnostics, and drug delivery (36; 37; 38). Some molecules naturally fluoresce; however, molecules that do not can be labeled with fluorescent tags for imaging. Organic fluorophores—the conventional fluorescence labels—have several limitations (39). They are unstable and suffer from photodegradation within minutes of light exposure. Furthermore, their narrow absorption spectrum requires the use of very specific excitation sources, and their broad emission spectrum reduces the imaging resolution when multiple dyes are used.

On the other hand, QDs have narrow emission spectra, and their emission wavelengths can be tuned by varying the NC size. This is valuable in multiplexed imaging to monitor multiple biomolecules simultaneously (7). Additionally, their broad absorption spectra enables excitation of the differently-sized QDs using a single light source. Well-passivated quantum dots have also exhibited enhanced photostability in comparison to the most stable organic dyes (40), which allows prolonged monitoring of labeled biomolecules.

Furthermore, the use of QDs can potentially improve sensitivity and reduce signal-to-noise ratio. Higher emission intensities have been observed from quantum dots as they possess higher molar extinction coefficients and similar photoluminescence quantum yields (PLQYs) to organic dyes (41; 42). Indirect bandgap QDs also benefit from large Stokes shifts. The distinction between the excitation and emission spectra of the NCs can improve signal-to-noise ratio and also prevents re-absorption of the emitted light, which increases sensitivity.

1.3 Synthesis of luminescent silicon quantum dots

The crystallinity of silicon nanomaterials plays an important role in their optical properties (43). Several techniques have been employed in the synthesis of SiNCs, and each of these methods possesses its own advantages and disadvantages. The production of SiNCs through liquid-phase approaches are impeded by their substantial time demands and low yields (44; 45; 46; 47). Gas-phase techniques, such as pyrolysis in furnace flow reactors (48; 49) or using infrared lasers (50) and photolytic decomposition of silicon precursors (51), are prone to agglomeration. Synthesis of SiNCs in low-pressure, nonthermal plasmas overcomes the aforementioned challenges (52).

1.3.1 Nonthermal plasma synthesis of crystalline silicon nanomaterials

We synthesize silicon nanoparticles (SiNPs) in a low-pressure, nonthermal plasma reactor as shown in Figure 1.2. A 13.56 MHz radio-frequency (RF) power is capacitively coupled into the plasma through copper ring electrodes. An external network matches the impedance of the source to the load to reduce the power reflected. Lieberman and

Lichtenberg gives a brief introduction into the design of matching networks in Reference (53).

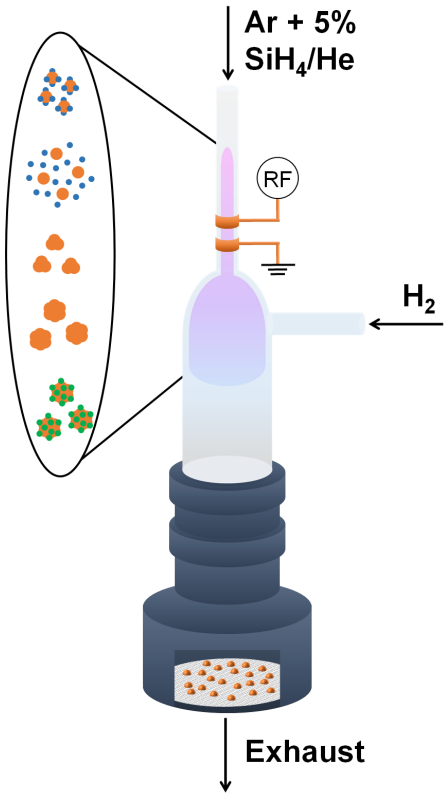

Figure 1.2: Experimental setup of nonthermal plasma reactor for SiNC synthesis.

A carrier gas, typically argon, and a silicon precursor, such as silane, are injected into the reactor. The electric field generated by the RF source ionizes the argon gas, and the hot electrons dissociate the precursor. SiNCs formed in the plasma are collected downstream of the synthesis region via diffusion or inertial impaction. The pressure in the reactor is maintained between 1 to 2 Torr either by adjustable orifices or feedback-controlled butterfly valve.

Crystallinity of the SiNPs is determined by the power input into the plasma (Figure 1.3). By varying the NPs' residence time in the plasma (e.g. changing the gas flow rates or the synthesis pressure), their sizes are tuned, which is an important advantage in the fabrication of NCs of different emission colors. Additionally, Wagner *et al.*

have shown that by operating in a regime where the plasma is constricted, cubic and cuboctahedral NCs can also be produced in addition to the spherical NCs (54).

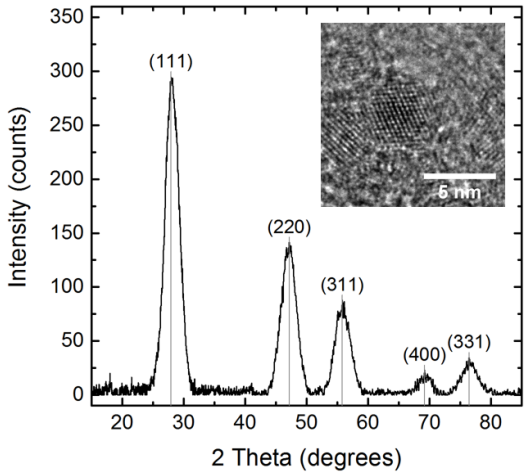

Figure 1.3: X-ray diffraction pattern of 4.2 nm SiNCs. Inset shows TEM of a single NC (image courtesy of Ting Chen).

Understanding dusty plasmas

Nonthermal plasmas are often characterized by their non-equilibrium thermodynamics. In capacitively-coupled plasmas (CCP), the electric field generated by an RF source accelerates electrons to high energies. These electrons play a key role in the excitation, ionization, and dissociation of the injected gases, and the resulting reactive species aid in the formation of SiNPs.

The non-equilibrium characteristic of a nonthermal plasma is beneficial for NP synthesis. Electron temperatures range from 2 to 5 eV and are significantly higher than the gas and ion temperatures, which remain close to room temperature (0.026 eV) (53; 55). This is advantageous in the SiNP synthesis process as high-temperature environments have been found to lead to the coagulation of particles (56).

The unipolar charging of the NPs also aid in the prevention of particulate agglomeration. As the highly energetic electrons impart negative charges to the plasma species, a repulsion force is generated between the NPs. Furthermore, as the reactor walls are also negatively charged, the NPs tend to remain confined in the discharge.

Particle charging. High-energy electrons in the low-pressure plasma not only play a key role in the chemical kinetics but also in particle charging. The electrons' higher mobility (relative to the cold ions) gives rise to more frequent collisions and consequently, imparts a net negative charge to the NPs. A resulting repulsion force is generated between the NPs, preventing agglomeration. This allows the production of NPs with a narrow size distribution, which is important in the fabrication of semiconductor devices. Furthermore, a negative charge is also generated at the walls as the hot electrons collide with the surfaces. The repulsive force between the negatively-charged NPs and the reactor walls reduces diffusion losses onto the walls and improves synthesis efficiency.

The charging of NPs is traditionally described by the orbital motion limited (OML) theory (57). However, recently, the validity of the theory has been questioned with simulations demonstrating an overestimation of particle charge. For example, in their experimental work, Ratynskaia *et al.* observed particle charges several times lower than predicted by the OML theory (58).

Several authors attribute the large discrepancies between the OML theory and experimental data to the neglect of charge-exchange collisions between ions and neutrals based on the significantly longer ion mean free paths to the Debye length (59; 60). However, negatively-charged particles can attract positive ions, and as the ions collide with neutrals in the particle sheath, trapped ions are generated in the particle's potential well (61; 62). With further collisions, these ions can be collected by the particle, resulting in an increase in ion flux to the particle. This leads to less negatively-charged particles than traditionally described by the OML theory.

Gatti *et al.* developed a model based on the ion-capture radius concept that accurately depicts the dependence of particle charge on particle sizes over a wide range of pressures (63). The ion current was modeled based on three components: the collisionless OML theory at low pressures, a transition region of enhanced collision and the high-collision hydrodynamic regime at high pressures. Gatti *et al.* determined the probability of collisions using the Knudsen number, which was defined by the particle's capture radius. They found that the ion current is enhanced when the ions perform more than one collision within the capture radius of the particle. Results of the model was in close relation with molecular dynamic simulations and several experimental results.

Formation of silicon nanoparticles. The synthesis of NPs in an argon-silane non-thermal plasma has been studied extensively in the 1990s by Bouchoule *et al.* (64; 65; 66; 67). Bouchoule and Boufendi *et al.*suggests particle formation proceeds in three steps: small particles are first created through the nucleation of clusters of atoms ($\sim$ 2 nm). Subsequently, the coalescence of the small particles leads to the formation of larger particles. Finally, as SiH_x radicals deposit onto the particle surfaces, large particles are grown (68).

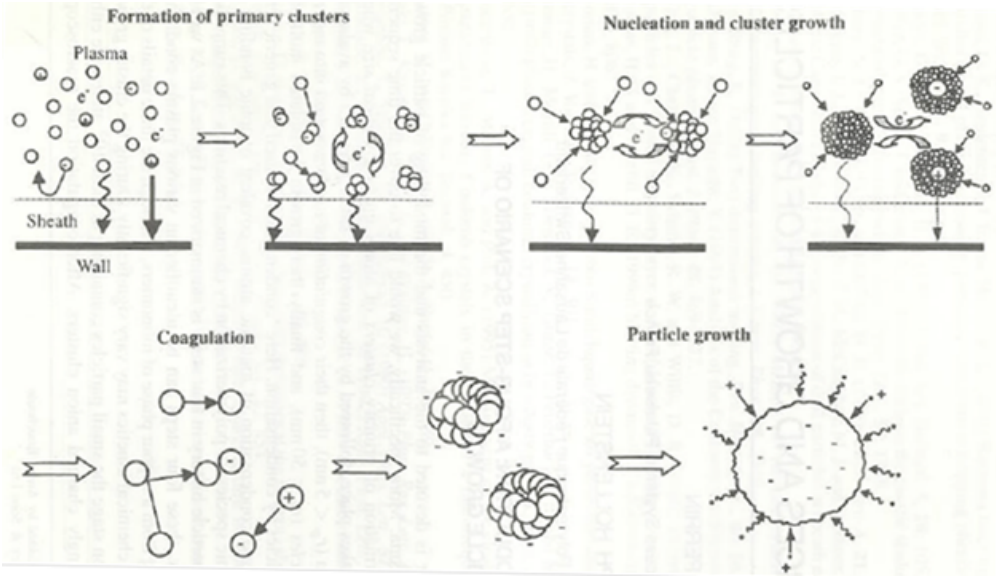

Figure 1.4: Schematic illustrating the steps of SiNP formation in a nonthermal plasma. Reproduced from (4).

The initial clustering process that leads to particle nucleation is highly debated. A popular hypothesis is that the negative ions function as precursors to particle formation. As the anions remain electrostatically trapped in the plasma potential, they would have time to cluster; however, cations and neutrals have short lifetimes in the plasma due to higher diffusion to the reactor walls. Hollenstein *et al.* proved this theory via mass spectrometry studies of the plasma (69; 70). The group observed the formation of powder when anions are trapped in the discharge (70). Furthermore, negatively-charged clusters, comprising of up to sixteen silicon atoms, with significantly higher masses than the positively-charged and neutral clusters were detected (69).

In the second stage, the negatively and positively-charged particles coagulate to form larger particles ($\sim$ 50 nm). Boufendi *et al.* saw a rapid increase in particle sizes and decrease in particle concentration in the first four seconds (71). However, as the particles grow in size, they become increasingly negatively charged, slowing down the coagulation rate. Kortshagen *et al.* observed that this phenomenon occurs when the particle density reaches the positive ion density (72). This implies that for coagulation to occur, the particle density must exceed the ion density.

In the final phase of growth, the particles experience a slower rate of growth despite a constant particle concentration in the plasma. This indicates that the surface deposition of SiH_x radicals is the key process in particle growth at this stage. Employing the same theory, Kortshagen *et al.* modeled the coagulation of silicon nanoparticles in a low-pressure argon-silane using the initial conditions based on the experimental values observed by Boufendi *et al.* (73). Similar trends were observed in their simulation, which validates the theory.

Crystallization of silicon nanoparticles. The crystallization temperature of SiNPs is size-dependent. For particles of 4, 6, 8 and 10 nm, crystallization occurs at 773, 1073, 1173 and 1273 K, respectively (74). The evident formation of SiNCs in nonthermal plasmas thus suggests that NPs are heated to relatively high temperatures (52). This is intriguing as gas temperatures in nonthermal discharges remain close to room temperature.

Bapat *et al.* extracted NPs from the reactor shown in Figure 1.2 at three different positions: (1) 5 cm upstream of the RF electrode, (2) 2.5 cm upstream of the RF electrode, and (3) 10 cm downstream of the RF electrode. Transmission electron microscopy (TEM) and diffraction patterns show the presence of amorphous cauliflower-shaped particles 5 cm upstream of the RF electrode. These are believed to be agglomerates of smaller primary particles. Further downstream in the plasma, polycrystalline particles are extracted, and finally the particles morph into single crystal NPs downstream of the RF electrode (75).

Mangolini *et al.* attributes the crystallization of NPs in the nonthermal plasma to the selective heating of the NPs (76). The group employed a Monte Carlo model to simulate the stochastic nature of electron-ion recombination and chemical reactions at

the particle surface. The collisionless OML theory was used to describe the electron and ion capture frequencies. Due to the relatively low particle temperatures, heat loss was assumed to proceed through conduction and convection only. The NPs in the plasma are able to attain instantaneous temperatures that significantly exceed the gas temperature. The authors attribute this phenomenon to exothermic surface reactions such as electron-ion recombination and hydrogen reactions at the NP surface. In a low-pressure environment, particle density is low; thus heat loss through conduction and convection is relatively inefficient, and particle heating through surface reactions dominates.

1.3.2 Functionalization of silicon quantum dots

In addition to crystallinity, the surface chemistry of a SiNC also plays an important role in their optical properties. At the nanoscale, 50 % of the atoms of a SiNC may lie at the surface (77). As the size of the NC decreases, the surface-to-volume ratio increases, and the surface properties begin to dictate the NC's properties. Surface defects, such as dangling bonds, or unpaired electrons, act as charge trap sites and degrade electron transport and optical properties (78; 79). These surface defects are believed to be the origins of weakened PLQYs, red-shifted emission peaks, and lengthened radiative lifetimes (80; 81).

Passivation of the surface dangling bonds with organic ligands or via oxidation have led to improved PLQYs (82; 83; 84; 85). Furthermore, enhanced stability has also been observed with functionalized surfaces. Silicon surfaces grafted with a monolayer of organic ligands have exhibited improved chemical and thermal stability (86; 87). Alkene and alkyne-terminated porous silicon (p-Si) have shown resistance against hydrolysis over a wide range of pH (86). Alkyl monolayers on Si(111) and Si(100) surfaces are also stable at elevated temperatures up to 615 K (88). SiNCs passivated with an oxy-fluoride shell have demonstrated stability in ambient conditions and against UV irradiation (89; 90).

Additionally, functionalization of the SiNCs can impart onto it new properties (91). Colloidal SiNCs can be obtained by grafting alkenes and alkynes onto the surface. The ability to disperse the SiNCs into non-polar solvents allows solution processing of thin films via drop casting, dip coating, spin coating, or spray coating. Hydrophilic SiNCs can

be produced by terminating the surface with amine or hydroxyl groups (92; 93; 94; 95) to engineer the NCs for biological applications.

Several functionalization techniques for silicon surfaces are discussed in Chapter 2.

1.4 Scientific objectives

The objectives of this dissertation are to:

1. Engineer environmentally-stable, luminescent SiQDs for optoelectronic, photovoltaic, and biological applications.
2. Develop all gas-phase SiQD synthesis and surface functionalization processe(s) to reduce/eliminate solvent waste.
3. Examine the potential of dual-purpose luminescent downshifting and antireflective SiQD films in enhancing solar cell efficiencies.

Chapter 2

Functionalization of silicon quantum dots

2.1 Hydrogen-terminated surface of nonthermal plasma-synthesized silicon nanocrystals

Silicon nanocrystals (SiNCs) produced in nonthermal plasmas are high in purity. FT-IR spectroscopy of SiNCs grown using silane as a precursor reveals their surface is solely passivated by hydrogen (Figure 2.1). The weak Si-O-Si absorbance at $\sim$ 1100 cm^{-1} suggests little to no oxidation occurred during synthesis. Their clean, hydrogen-rich surface removes the need for post-synthesis purification steps prior to surface engineering, and their high surface-to-volume ratio is an advantage in the characterization of their surface chemistries.

While the Si(111) or Si(100) surface consists of silicon monohydrides and dihydrides, trihydrides are found on the SiNC's surface (96). Figure 2.1 shows a deconvoluted FT-IR spectrum of the SiH_x stretching modes. Significant SiH_3, along with SiH_2 and SiH groups, exist on the NC's surface as depicted in Figure 2.2. The disordered surface is likely strained due to steric repulsion between neighboring moieties, and the weakened bonds may facilitate surface modification.

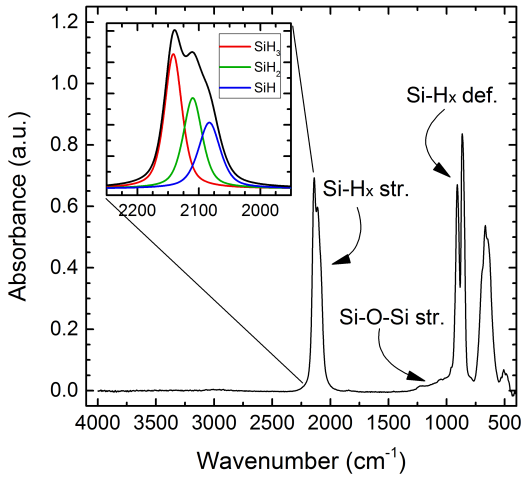

Figure 2.1: FT-IR spectrum of hydrogen-terminated nonthermal plasma-synthesized SiNCs. Inset shows a deconvoluted spectrum of the silicon hydride stretching modes: SiH_3 (red), SiH_2 (green), and SiH (blue).

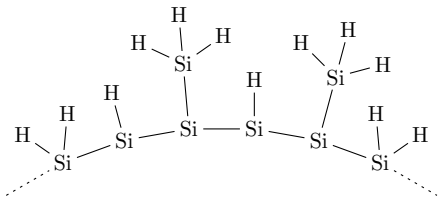

Figure 2.2: Hydrogen-terminated surface of nonthermal plasma-synthesized SiNCs.

2.2 Alkyl passivation

2.2.1 Thermal hydrosilylation

Hydrosilylation is a common technique used to attach organic molecules with unsaturated vinyl groups onto hydrogen-terminated silicon surfaces. The reaction can be initiated thermally at temperatures above 150 ^{o}C (97; 98), or photochemically using UV or white light at room temperature (85; 99; 100).

Thermal hydrosilylation is proposed to be a radical-based reaction (101). At elevated temperatures, the reaction occurs in the absence of catalysts and radical initiators (97), suggesting that heat is able to dissociate Si-H bonds on the silicon surface. The resulting

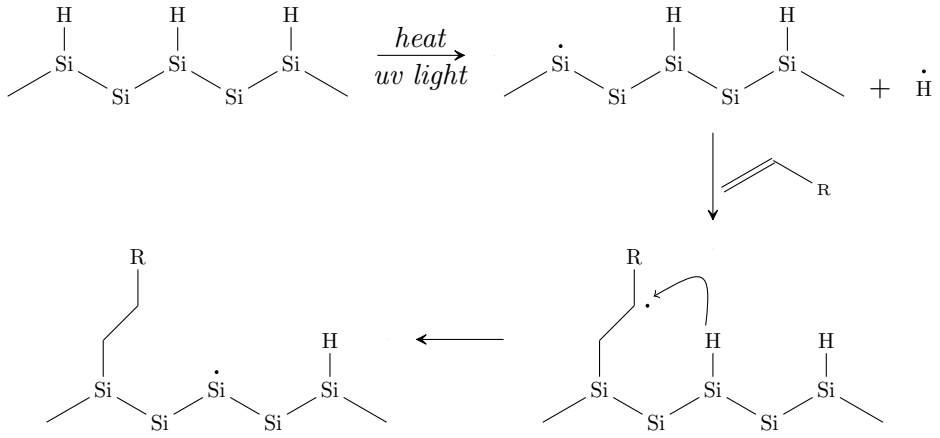

Figure 2.3: Mechanism for radical-based hydrosilylation of silicon surfaces.

dangling bonds are highly reactive, and insertion of an alkene into the dangling bond results in the formation of a Si-C bond and carbon-based radical. Abstraction of a hydrogen atom from a neighboring silicon by the carbon atom leaves a silicon radical on the surface, and the reaction propagates along the surface. The mechanism for the thermal hydrosilylation reaction is depicted in Figure 2.3.

Figure 2.4 depicts the experimental apparatus that is used for thermal hydrosilylation. We disperse hydrogen-terminated SiNCs in a mixture of 1-dodecene (the functional molecule) and mesitylene (a background solvent). The SiNC solution is placed in a sand bath maintained at 215 ^{o}C and heated for 3 h. A continuous flow of nitrogen is necessary to prevent oxidation, and solvent evaporation is reduced using a chilled water condenser. Post hydrosilylation, the unreacted solvents are evaporated, and the SiNCs are re-dispersed into non-polar solvents for liquid-phase processing.

The Fourier transform infrared (FT-IR) spectrum of the thermally-hydrosilylated SiNCs (Figure 2.5) show intense CH_x absorption from the organic ligands. The lack of absorption from C=C groups at $\sim$ 1600 cm^{-1} implies 1-dodecene molecules were successfully grafted onto the NC surface through the vinyl group. However, the alkyl surface coverage was incomplete—significant hydrides remained on the surface due to steric hindrance between the long ligands. The theoretical limit for alkyl surface coverage for the hydrosilylation reactions is $\sim$ 50 % (102). However, improved passivation of nonradiative defects led to enhanced optical properties—photoluminescence quantum

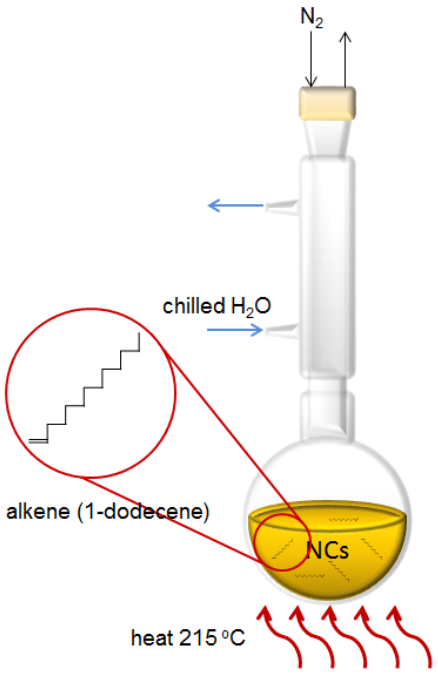

Figure 2.4: Experimental setup of thermal hydrosilylation reactor.

yields (PLQYs) exceeding 60 % were measured (83).

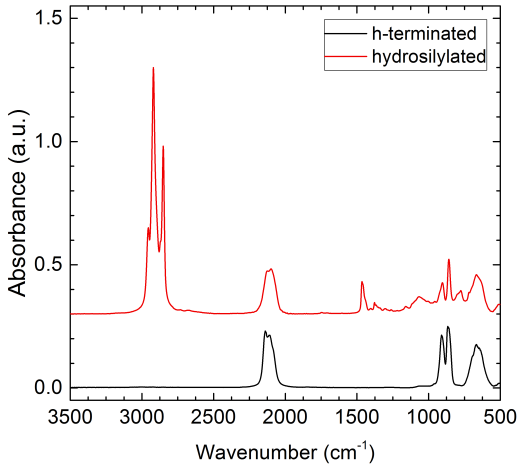

Figure 2.5: Typical FT-IR spectra of hydrosilylated SiNCs (a) and H-terminated SiNCs (b).

The hydrosilylated SiNCs exhibited enhanced thermal stability as compared to the hydrogen-terminated SiNCs. We investigated the desorption of surface moieties at elevated temperatures was via FT-IR spectroscopy. SiNCs were deposited onto an attenuated total reflectance (ATR) crystal and heated to 500 ^{o}C under vacuum (10^{-6} Torr); measurements were acquired at 50 ^{o}C intervals. For hydrogen-terminated SiNCs, the FT-IR spectra revealed initial desorption of surface hydrides under 100 ^{o}C (Figure 2.6). The surface of the hydrosilylated SiNCs is more robust; hydrogen and alkyl desorption only began between 200 ^{o}C and 250 ^{o}C. These results were similar to those observed on alkyl-terminated Si(111) and Si(110) surfaces by Sung *et al.* (88).

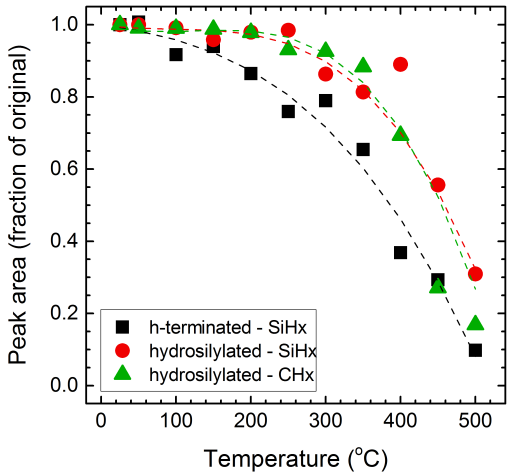

Figure 2.6: Change in integrated absorption of CH_x and SiH_x modes of hydrogen-terminated (black) and hydrosilylated SiNCs (red and green) at elevated temperatures.

The robustness of the hydrosilylated surface gave rise to the SiNCs' optical stability. While the PLQY of the hydrosilylated SiNCs decreased at elevated temperatures (Figure 2.7a), the photoluminescence recovered when the SiNCs were cooled to room temperature (Figure 2.7b). The photoluminescence measurements revealed redshifts in the peak emission wavelengths with increased temperature. A similar trend was observed by Wen *et al.*, which they attributed to thermal delocalization and an increase in nonradiative defect states. These changes in optical properties were temporary; complete recovery of the photoluminescence was observed for SiNCs heated up to 100

^{o}C—the maximum temperature a commercial solar cell would sustain.

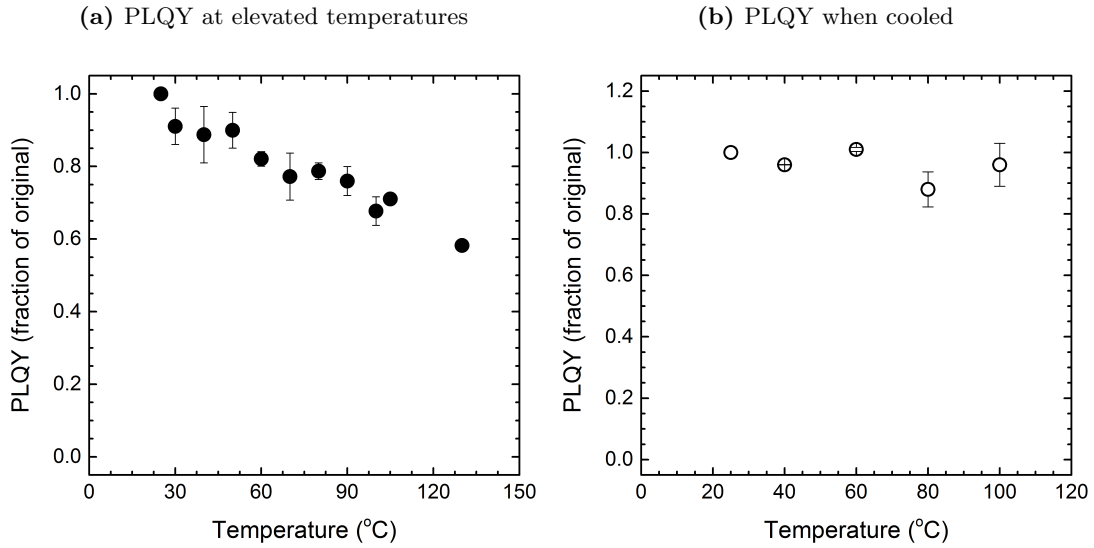

Figure 2.7: (a) PLQY of hydrosilylated SiNCs at elevated temperatures. (b) Restoration of PLQY when cooled to room temperature.

The photostability of the SiNCs is also an important property for real-world applications. The stability of the thermally-hydrosilylated SiNCs under UV irradiation is investigated in Chapter 3.

While thermal hydrosilylation has achieved favorable results, its use will likely be constrained to the lab. The high temperature, large amount of solvents, and free flow of cooling water needed may be a deterrent for industrial applications.

2.2.2 Photochemical hydrosilylation

Hydrosilylation can be induced photochemically at room temperature (103), and the removal of the thermal energy input can potentially ameliorate some of the aforementioned issues.

UV light-mediated hydrosilylation is induced by photocleavage and/or photoemission. For photocleavage to occur, the UV light must possess sufficient energy to homolytically cleave silicon hydride bonds on the surface to leave surface dangling bonds

for alkyl attachment (104; 105). The reaction then proceeds via the radical-based mechanism depicted in Figure 2.3. In photoemission, the high-energy photon absorbed ejects an electron from the surface of the NC to a neighboring acceptor molecule. A positive hole is left on the surface and is susceptible to attack by an unsaturated vinyl group (106; 107).

White light ($>$ 400 nm) is a relatively low energy light source, thus it is unlikely to break silicon hydride bonds. White light-mediated hydrosilylation is believed to be driven by excitons (107). The long-lived excitons generated by photon absorption can be localized on the quantum dot (QD) surface. The localized holes are susceptible to nucleophilic attack by alkenes/alkynes to create Si-C bonds. The resulting β-silyl-substituted carbocation is then neutralized by a neighboring surface hydride and the electron from the generated exciton.

Hydrosilylation of SiNCs using common light sources, mercury-vapor (UV/blue light) and halogen (white light) lamps, are investigated in Chapter 4.

2.2.3 Gas-phase functionalization

Effort towards lean manufacturing was previously made by exploring gas-phase reactions in the nonthermal plasma reactor for surface passivation. Mangolini *et al.* devised a two-step system to graft the ligands onto SiNCs in the nonthermal plasma (Figure 2.8). SiNCs were formed in a first synthesis plasma (similar to the reactor described in Figure 1.2 in Chapter 1) and delivered into a second plasma for surface passivation. Vaporized organic molecules were bubbled into the latter plasma using argon gas. Hot electrons in the plasma were able to dissociate the molecules, leaving radicals to react with the SiNC surface.

The design was simplified by Anthony *et al.* (Figure 2.9). The SiNC synthesis and 1-dodecene grafting were combined into a single plasma reactor, eliminating the need for an additional power delivery system. 1-dodecene was bubbled into the expansion (diffused) region of the synthesis plasma, several inches downstream of the electrodes, using hydrogen gas. This technique allowed the development of an entirely gas-phase produced SiNC-based inorganic LED.

While FT-IR spectroscopy of the SiNCs produced in the two aforementioned reactors revealed the presence of CH_x groups, the gas-phase functionalized SiNCs suffer

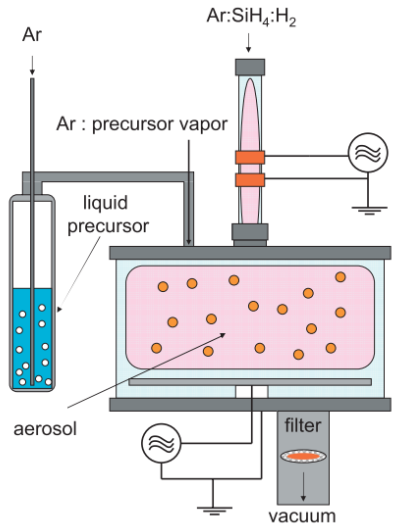

Figure 2.8: Experimental setup of two-staged nonthermal plasma reactor for NC synthesis and in-flight alkyl passivation. Image taken from (5).

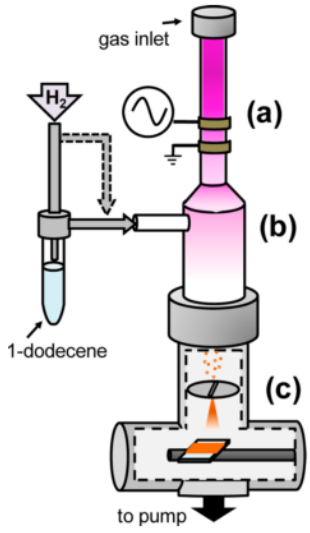

Figure 2.9: Simplified nonthermal plasma reactor for NC synthesis and in-flight alkyl passivation. Image taken from (6).

from weak photoluminescence, with PLQYs under 10 %. The origin of the poor optical properties is investigated in Chapter 5, and techniques to improve the PLQY are

explored.

2.3 Oxide passivation

The growth of an oxide shell on silicon is another approach for passivating nonradiative surface defects. Several groups have observed enhanced PLQY from oxidized SiQDs (43; 108) or SiQDs embedded in silicon oxide or silicon nitride matrices (109; 110).

We synthesized hydrogen-terminated SiNCs of a range of sizes in the nonthermal plasma reactor depicted in Figure 1.2 and left the NCs to oxidize in ambient conditions. Improvements in PLQY was observed with the growth of a native oxide shell; after 20 days of oxidation, PLQYs nearing 20 % was measured for the smallest SiNCs with an emission peak centered at $\sim$ 750 nm (Figure 2.10).

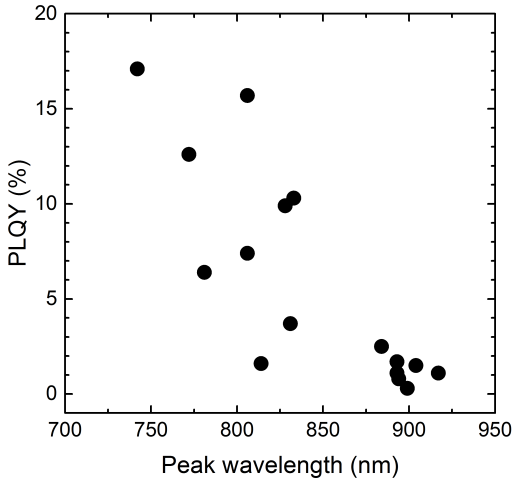

Figure 2.10: PLQY of oxidized hydrogen-terminated SiNCs as a function of peak photoluminescence wavelength. Measurements were acquired after 18 days in ambient conditions.

2.3.1 Fluorine passivation

The oxidation of hydrogen-terminated is a slow process; however, incorporation of fluorine onto the surface significantly enhances oxidation due to the high surface electronegativity induced (84; 108). Oxidized fluorine-terminated SiNCs have also exhibited PLQYs exceeding that of oxidized hydrogen-terminated SiNCs. Upon complete oxidization at $\sim$ 2 weeks, PLQYs nearing 50 % were measured by Liptak *et al.* (89). Furthermore, enhanced environmental stability has been observed (89).

Pi and Liptak *et al.* employed a similar setup to the two-staged nonthermal plasma reactor devised by Mangolini *et al.* to fabricate fluorine-passivated SiNCs. The effects of tetrafluoromethane (CF_4) and sulfur tetrafluoride (SF_6) injection into the second surface treatment plasma were studied in the reactor depicted in Figure 2.11 (3; 84). In addition to surface-passivating atoms, fluorine radicals also act as etchants, allowing the synthesis of sub-3 nm SiNCs in the plasma. The plasma power and CF_4 and SF_6 flow rates play a significant role in the etch rates (108).

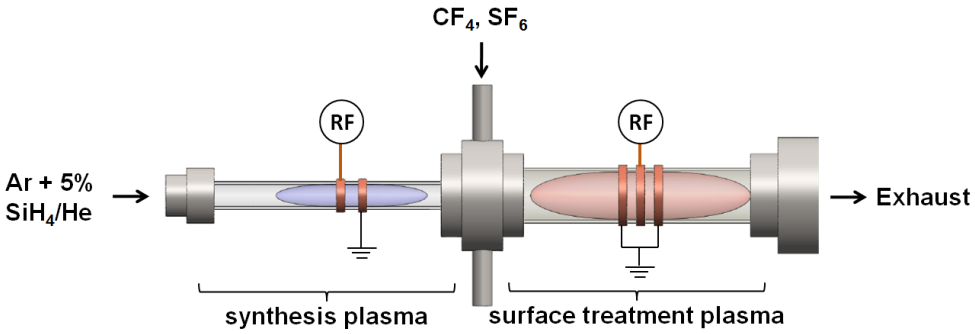

Figure 2.11: Experimental setup of two-staged nonthermal plasma reactor for NC synthesis and fluorine passivation.

We simplified the process following Anthony *et al.*'s gas-phase alkyl functionalization reactor (6). The diffused plasma in the expansion region of the reactor depicted in Figure 1.2 has the ability to dissociate molecules. In place of hydrogen gas, $SF_6$was injected through the sidearm into the plasma. Similar to the two-staged reactor, the size of the SiNCs can be modified by tuning the plasma power and the SF_6 flow rate. PLQYs nearing 50 % were also obtained after 2 weeks of oxidation. It was also observed

that an ideal SiNC size, with peak emission wavelength $\sim$ 750 nm, for maximizing PLQY exists (Figure 2.12).

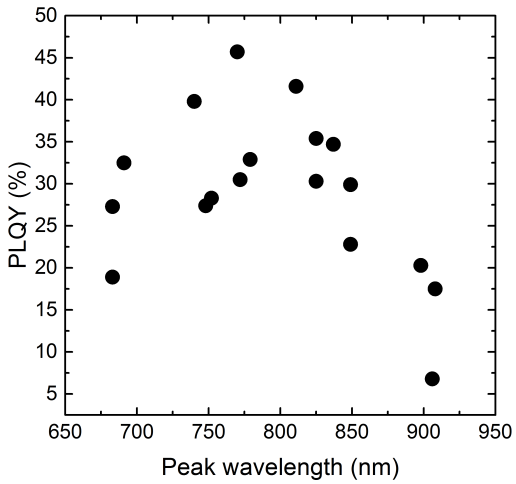

Figure 2.12: PLQY of oxidized SF_6-etched SiNCs as a function of peak photoluminescence wavelength. Measurements were acquired after 18 days in ambient conditions.

The oxidation of the SiNCs can be further accelerated by injecting oxygen into the plasma along with SF_6. At low flow rates, oxygen has a positive impact on the SiNCs' optical properties. PLQYs exceeding 50 % were measured after 3 days of oxidation in ambient conditions (Figure 2.13). However, weak photoluminescence was observed at high oxygen concentrations, likely due to a competition between the oxygen species and fluorine radicals in the plasma for SiNC surface sites.

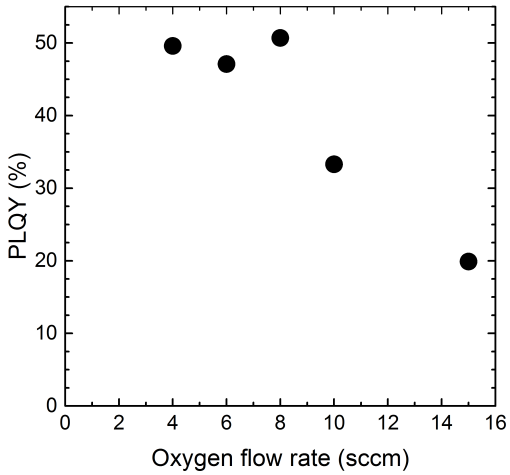

Figure 2.13: Photoluminescence quantum yields of in-flight oxidized, SF_6-etched SiNCs as a function of oxygen flow rate. Measurements were acquired 3 days after synthesis.

2.4 Biocompatible silicon quantum dots

Solubilization of the SiNCs in water is essential for biological applications. Hydrogen-terminated SiNCs produced in the nonthermal plasma shown in Figure 1.2 are highly hydrophobic. The NCs tend to float on water (Figure 2.14), and solubility does not improve with stirring or sonication.

Figure 2.14: Hydrophobic hydrogen-terminated SiNCs on water.

Biocompatible QDs are typically produced through surface engineering. II-VI QDs such as CdSe have been linked to biomolecules using conjugating ligands such as mercaptoacetic acid or mercaptosilane, via electrostatic forces between negatively-charged QDs and positively-charged molecules, or by incorporating the QDs into micro or nano-beads

(Figure 2.15) (7).

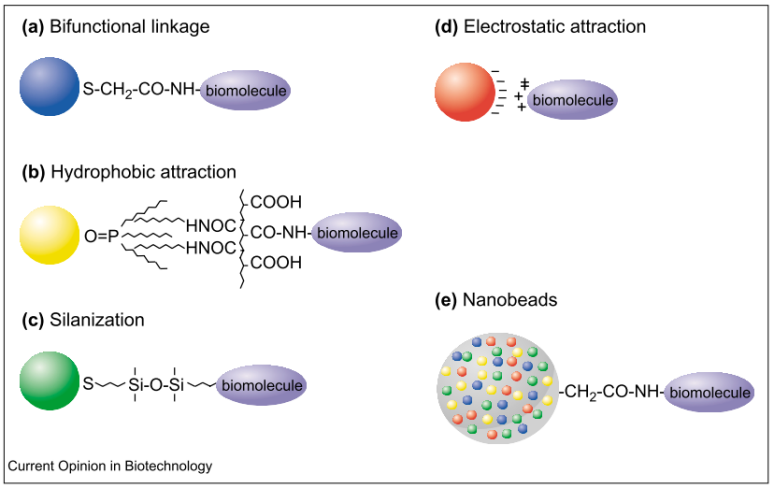

Figure 2.15: Schematic of the different methods for QD bioconjugation. Image taken from (7).

Surface engineering on silicon is more challenging due to the strong covalent bonds formed on the surface. However, hydrophilicity has been observed in SiQDs encapsulated in silica (111) and QDs grafted with allylamine (93) or acrylic acid (92). These allylamine and acrylic acid-terminated SiNCs were successfully incorporated into HeLa cells and hamster ovary cells, respectively, for fluorescence imaging.

2.4.1 Silica shell

Several approaches have been used to grow a hydrophilic silica shell onto SiQDs. The simplest method was the reaction of the QDs with hydrogen peroxide (in ethanol) (94). SiQDs react readily with water; however, the addition of hydrogen peroxide slows the reaction rate and allows control over the growth of the silica shell. A range of emission colors from red to blue was obtained by tuning the reaction time.

Silica-encapsulated SiNCs were also produced through a complex sol-gel method using tetraethylorthosilicate (TEOS) precursor and triethylamine (TEA) catalyst (111). Improved colloidal stability was obtained by grafting amine groups onto the silica shell using aminopropyltriethoxysilane (APTS). The SiQDs showed enhanced stability in water and continued to luminesce after a week in solution.

The third method using a microplasma serves to reduce the amount of impurities in the fabrication process. Freestanding SiNCs were treated in water with DC or RF-powered microplasma (112; 113). Passivation of the surface is believed to be a result of hydroxyl radicals generated by electron dissociation of the water molecules. Condensation of hydroxyl groups at the surface forms a protective silica shell. Photoluminescence intensities of the microplasma-treated SiQDs remained stable after 20 days in water.

Microplasma surface treatment of nonthermal plasma-synthesized SiNCs is studied in Chapter 6.

2.4.2 Allylamine and allyl alcohol passivation

Amine and hydroxyl groups can form hydrogen bonds with water molecules; thus, the functional groups have been shown to impart hydrophilicity to QDs (93).

Allylamine and allyl alcohol, organic compounds with unsaturated amine and hydroxyl groups, respectively, can react with hydrogen-terminated SiNCs via their unsaturated vinyl groups. We attempted thermal and light-induced hydrosilylation, which yielded unfavorable results. FT-IR spectra of the SiNCs (Figure 2.16) lacked the characteristic N-H and O-H vibrational peaks at $\sim$ 3400 cm^{-1}; instead, strong Si-N-Si or Si-O-Si peaks at $\sim$ 1100 cm^{-1} were observed. The results suggest that the allylamine and allyl alcohol reacted with the silicon surface via the amine and hydroxyl groups. The vinyl groups at the tail of the ligand, evident by the C=C peak at $\sim$ 1600 cm^{-1}, created a hydrophobic surface that is insoluble in water.

Radical initiator-assisted hydrosilylation

Silicon has a strong affinity to nitrogen and hydrogen atoms; thus, it is necessary to employ other means to induce radicals in the hydrosilylation reactions. Benzoyl peroxide (BP) and azobisisobutyronitrile (AIBN) are common radical initiators used in free radical reactions. The molecules decompose at low temperatures (60 – 80 ^{o}C) to generate a radical pair. The radicals abstract a hydrogen from the silicon surface, creating silyl radicals that can react with the unsaturated vinyl groups of the allylamine or allyl alcohol. The initiation mechanism is shown in Figure 2.17.

FT-IR spectra of the allylamine-functionalized SiNCs through radical initiator-assisted hydrosilylation are shown in Figure 2.18. The presence of N-H vibrational peaks from

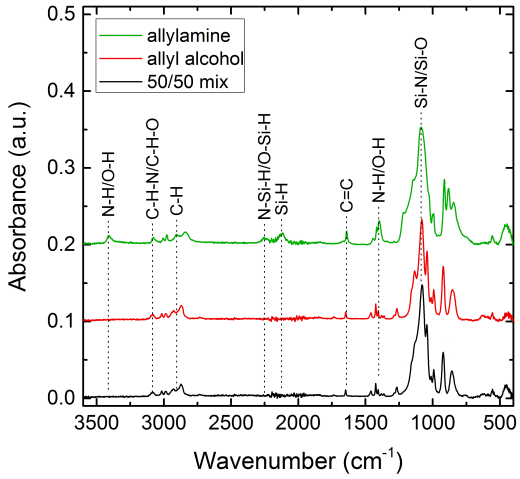

Figure 2.16: FT-IR spectra of allylamine and allyl alcohol functionalized SiNCs produced from thermal hydrosilylation.

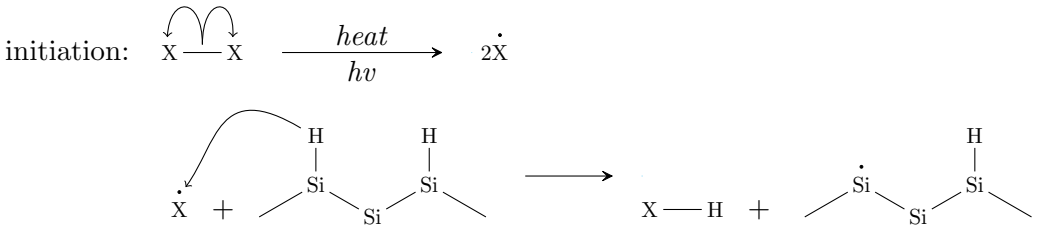

Figure 2.17: Mechanism for radical-initiated hydrosilylation of silicon surfaces using BP or AIBN.

NCs produced in both BP and AIBN reactions indicates that the radical initiators aided in the reaction of the vinyl groups to the silicon surface. However, the strong Si-N-Si absorption observed from the AIBN reaction suggests that significant amount of amine groups had reacted with the SiNCs as well. Consequently, inferior solubility was obtained from the AIBN-reacted SiNCs in comparison to the BP-reacted NCs as shown in the insets of Figure 2.18.

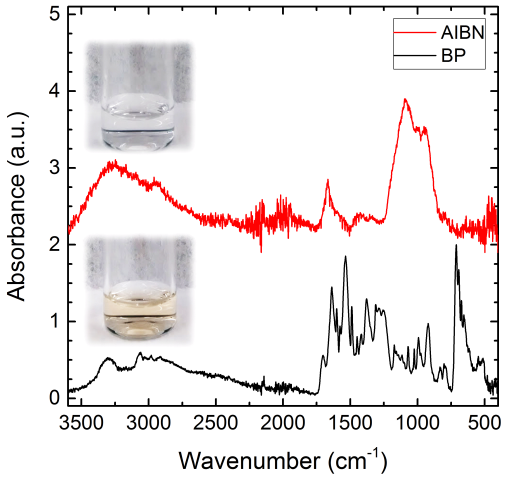

Figure 2.18: FT-IR spectra of allylamine-functionalized SiNCs produced from BP and AIBN-initiated hydrosilylation. Insets are pictures of the filtered SiNCs dispersed in water.

Catalytic hydrosilylation

Hydrosilylation with the aid of chloroplatinic acid (H_2PtCl_6), a platinum catalyst, yielded the most promising results. The mechanism of the catalytic hydrosilylation reaction is shown in Figure 2.19. Strong N-H vibrational peaks were observed in the FT-IR spectra of the allylamine-functionalized SiNCs (Figure 2.20). The persistent Si-N-Si peak suggests that some ligands were attached through the amine group; however, the unfavorably functionalized SiNCs were removed upon filtering with a 0.2 μm PTFE (polytetraethyfluoroethylene) filter.

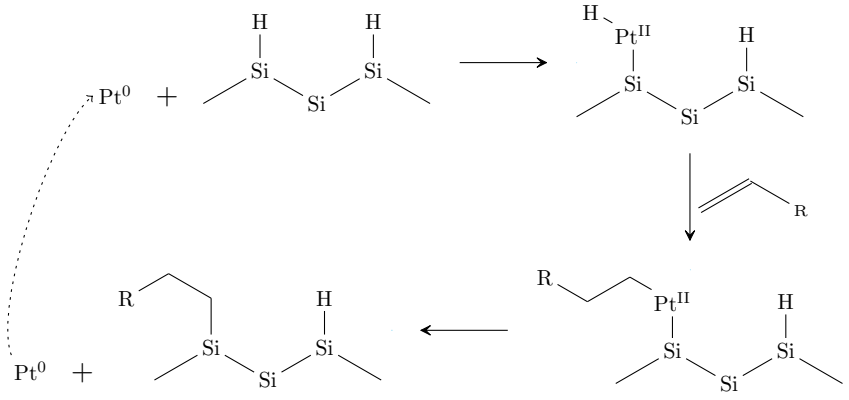

Figure 2.19: Mechanism for catalytic hydrosilylation of silicon surfaces.

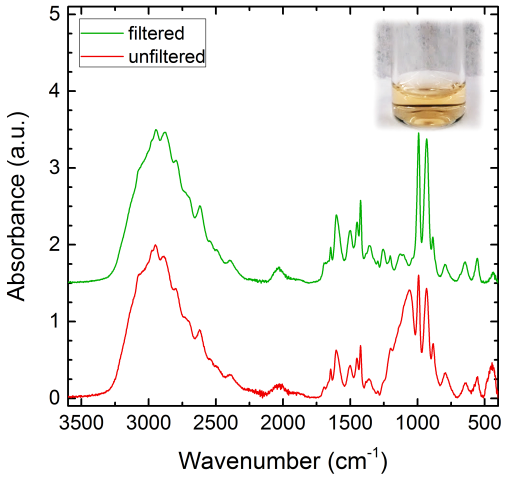

Figure 2.20: FT-IR spectra of allylamine-functionalized SiNCs produced from H_2PtCl_6-catalyzed hydrosilylation before and after filtering. Inset is a picture of the filtered SiNCs dispersed in water.

Comparison

The chloroplatinic acid-aided hydrosilylation reaction demonstrated the highest yield of the three methods, while the lowest yield was obtained from the AIBN reactions. The colloids of SiNCs produced from each reaction are depicted in Figure 2.21. Similar masses of SiNCs were used in the reactions initially; post reaction, the unfunctionalized

SiNCs were removed using 0.2 μm filters.

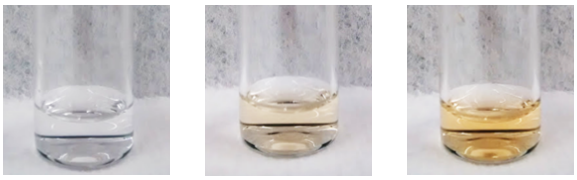

Figure 2.21: Pictures of the filtered water-soluble SiNCs produced using three different methods. Similar amounts of SiNCs were used in each functionalization reaction

Dynamic light scattering (DLS) spectroscopy of the filtered H_2PtCl_6-reacted SiNCs reveal individually-separated 4 nm SiNCs dispersed in water (Figure 2.22). Small agglomerates $\sim$ 7 nm in size were detected from the BP reactions. Supporting the reaction yields obtained, the AIBN reactions had the poorest results; highly polydispersed, large agglomerates $>$ 100 nm were measured. The functionalized SiNCs from all three reactions demonstrated excellent stability in water; no visible etching was observed after 4 months in water.

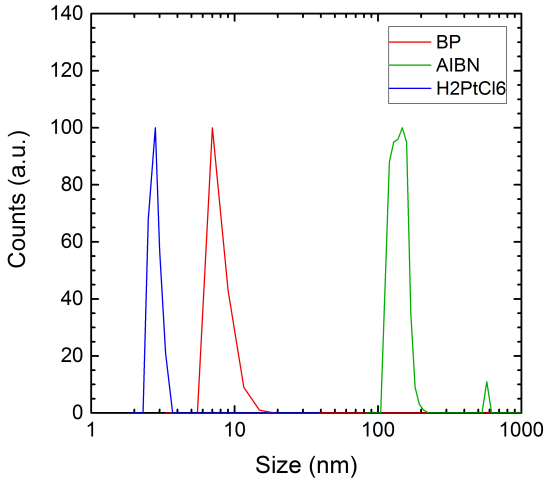

Figure 2.22: DLS of allylamine-functionalized SiNCs produced using BP, AIBN, and H_2PtCl_6 after filtering.

Similar to as-produced, hydrogen-terminated SiNCs, the functionalized SiNCs absorbed strongly in the UV region (Figure 2.23a). Chloroplatinic acid-reacted SiNCs displayed a second absorption peak from platinum impurities in the solution. These impurities can be easily removed using metal scavengers.

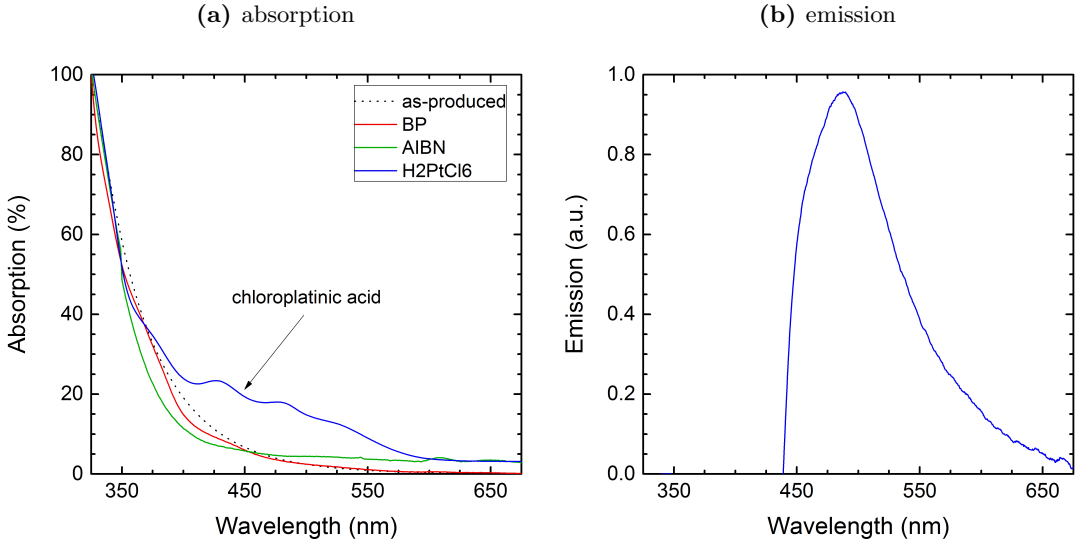

Figure 2.23: (a) Absorption spectrum of allylamine-functionalized SiNCs produced from BP, AIBN, and H_2PtCl_6-induced hydrosilylation in comparison to as-produced, hydrogen-terminated SiNCs. (b) Emission from H_2PtCl_6-reacted SiNCs.

Despite the success of the reactions, only weak blue emission ($<$ 10 % PLQY) centered at $\sim$ 490 nm—likely from defect states—was detected from the SiNCs (Figure 2.23b), similar to results obtained by Warner *et al.*

2.4.3 Acrylic acid passivation

Red luminescence, likely from bandgap emission, was observed in (poly)acrylic acid-functionalized SiNCs (92). (Poly)acrylic acid, with its high density of carboxylic acid functional groups, can be used to immobilize biomolecules with amine groups. Li *et al.* devised a simple radical-based hydrosilylation approach to graft acrylic acid monomers onto SiQDs. Freestanding hydrogen-terminated SiNCs were dispersed in a mixture of

acrylic acid and ethanol and irradiated with UV light at 40 ^{o}C for 24 h. The SiQDs retained 80 % of their initial photoluminescence intensity after 5 days of dispersion in water. Enhanced stability against photobleaching in comparison to conventional organic fluorophores was also observed.

Chapter 3

Photostability of thermally-hydrosilylated silicon quantum dots

3.1 Introduction

Since the observation of photoluminescence from porous silicon in 1990 (9), the appeal of silicon in optoelectronic and biological devices and in third generation photovoltaics has grown. At the nanoscale, silicon exhibits size-dependent optical and electronic properties, which allows the tailoring of their band gap and emission wavelengths. Silicon quantum dots (SiQDs) were applied in hybrid nanocrystal-organic LEDs by Cheng *et al.*. Peak external quantum efficiencies up to 8.6 % were attained for LEDs emitting from red to near-infrared. (14). In photovoltaic applications, silicon nanocrystal (SiNC) layers functioning as luminescent downshifters have led to enhancements in the internal quantum efficiencies of solar cells (114; 23). Recently, carrier multiplication studies have demonstrated the possibility of further increasing solar cell efficiencies past the Shockley Queisser limit (33; 34).

To be a promising candidate for the abovementioned applications, the SiQDs must exhibit enhanced optical properties and stability with environmental exposure. Mangolini *et al.* obtained photoluminescence quantum yields (PLQY) exceeding 60 % from

SiNCs synthesized in a nonthermal plasma reactor and thermally hydrosilylated with organic ligands, specifically, 1-dodecene (83). The hydrosilylated NCs can be colloidally dispersed into organic solvents for solution-phase device fabrication. However, alkyl-functionalized silicon surfaces are prone to oxidation (115), and their photoluminescence has been shown to degrade with prolonged UV exposure (115; 46; 90).

In order to fabricate photostable SiNCs, it is necessary to understand the origin of the photodegradation. Here, we study the stability of hydrosilylated, nonthermal plasma-synthesized SiQDs under 365-nm light. Photoluminescence measurements of colloidal SiQDs indicate degradation of the QDs' PLQY with irradiation time. Electron paramagnetic resonance (EPR) and Fourier transform infrared spectrometry (FT-IR) are used to probe the origin of the photodegradation; the results revealed an increase in dangling bond defects due to the breakage of silicon hydride bonds at the NC surface. The passivation of these dangling bonds in a second hydrosilylation reaction led to the recovery of the QDs' PLQY. Furthermore, the resulting SiQDs were photostable, and no further degradation in PLQY was observed with additional UV exposure.

3.2 Results and Discussion

Silicon nanocrystals were synthesized in a nonthermal plasma reactor and functionalized with 1-dodecene via thermal hydrosilylation reaction that has been described by Mangolini *et al.* (116). A typical X-ray diffraction (XRD) pattern of these SiNCs is shown in Figure 1.3. Debye-Scherrer fits of XRD peaks established an average particle size of $\sim$ 4.2 nm. The PLQY of these as produced QDs dispersed in toluene was measured to be 56 $\pm$ 6 % with peak wavelength at 828 $\pm$ 3 nm, which corresponds to band gap emission of the SiQDs (117).

The photostability of the QDs to UV exposure was studied by irradiating colloidal NCs sealed in nitrogen atmosphere with 365-nm light at a power density that is comparable to that of sunlight in the UV region under AM1.5G conditions. This was calculated to be equivalent to $\sim$ 4 mW/cm^2. Figure 3.1 reveals that the UV irradiation resulted in significant degradation of the SiQDs' optical properties. Within 4 h of irradiation, their PLQY degraded from $\sim$ 56 % to less than 40 %—almost 30 % decrease in the

QDs' PLQY. After 4 h of irradiation, steady-state was reached and no further degradation was observed. In comparison, under room (fluorescent) light, only slight (< 5 %) PLQY degradation was observed. Insignificant change in the photoluminescence peak wavelength was detected, aside from a blueshift at 24 h of UV irradiation that is most likely the result of oxidation. The increased oxidation is indicative of the photo-induced enhanced oxidation rate that has been reported by several groups (118; 119).

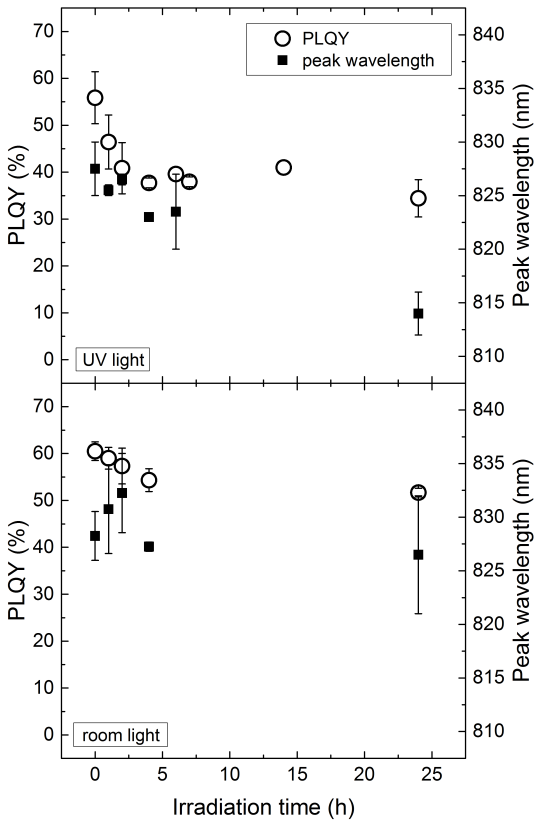

Figure 3.1: Time-study of SiQDs' PLQY (open circles) and peak PL wavelength (solid squares) during UV light exposure (top). The SiQDs' photoluminescence under room light is shown for comparison (bottom).

Photo-induced degradation was also observed in hydrogenated amorphous silicon (a-Si:H) due to a mechanism known as the Staebler-Wronski effect (SWE). It was shown that prolonged light illumination leads to a decrease in photoconductivity of a-Si:H

films (120; 121; 122), which is attributed to the creation of defects from the breakage of Si-H or Si-Si bonds (123). UV light is also known to break surface bonds of flat and porous silicon during photochemical hydrosilylation reactions. In this process, it is believed that high-energy photons are able to homolytically cleave silicon hydride bonds to generate reactive sites for the attachment of organic ligands (101; 103).

Unpaired electrons generated by the abovementioned process can be probed via electron paramagnetic (or spin) resonance (EPR) (124; 125; 126). The EPR of nonthermal plasma-produced SiNCs has been studied extensively by Pereira *et al.* (124; 125). Two defect signals have been detected in freestanding SiNCs: (1) D centers allocated to three-fold coordinated silicon (or dangling bonds) in a disordered environment, and (2) an asymmetrical signal assigned to P_b centers at the interface of the SiNC and its oxide shell. A typical EPR signal of hydrosilylated SiNCs is shown in Figure 3.2. The spectrum resembles that of SiNCs with low initial defect density (LIDD) shown in reference 125 and exhibits an insignificant P_b signal. For these LIDD SiNCs, the dangling bond density has been calculated to be less than 1 per 200 NCs.

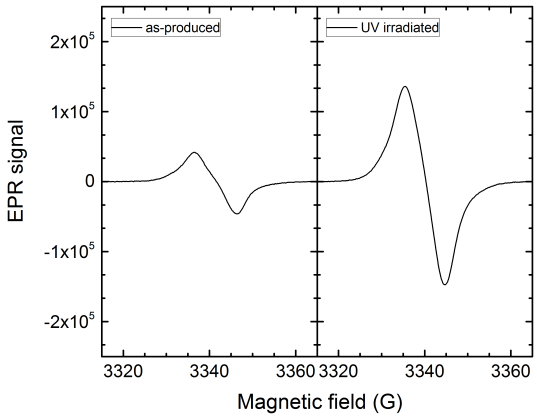

Figure 3.2: EPR spectra of SiNCs before and after UV exposure.

The EPR of UV-irradiated SiNCs revealed a significantly higher density of unpaired electrons (Figure 3.2). These unpaired electrons can act as sites for electron-hole recombination, preventing radiative recombination, thus, resulting in a reduction in the SiQDs' PLQY (78; 79). Due to the lack of asymmetry, the bulk of the EPR signal amplification is attributed to an increase in D centers that is the result of the generation

of dangling bonds due to bond breakage, similar to results reported by Dersch *et al.* (123).

The approximately 3.5 times increase in dangling bond defect density may not explain the 20 % reduction in PLQY. Recently, it has been presented that if the energy of the photon were above that of the work function of the SiNC's surface, an electron can be ejected from the conduction band, leaving a reactive cation species at the surface (106; 107). These positively-charged species can act as exciton traps, preventing electron-hole recombination. However, since cations are not EPR active, another method will need to be employed for the detection of these defects (not in the scope of this work).

Two material properties are proposed to play critical roles in the SWE observed in a-Si:H films: (1) disorder in the silicon network and (2) the presence of hydrogen (127). These are also characteristics of the SiNC surface; thus, the elevated D center signal is postulated to be derived from unpaired electrons at the NC surface.

At 4.2 nm, almost 50 % of the silicon atoms ($\sim$ 900 atoms) in a SiNC lie on its surface (77). FT-IR spectroscopy reveals that the surface of nonthermal plasma-produced SiNCs is highly disordered, comprising of hydrogen in the form of SiH_3, along with SiH and SiH_2, as depicted in Figure 3.3. Steric factors limit the coverage with long alkyl ligands on the silicon surface to $\sim$ 50 % (102). A typical IR spectrum of 1-dodecene functionalized SiNCs is represented by Figure 3.4(b). Peaks between 3000 cm^{-1} and 2800 cm^{-1} are fingerprints of CH_x stretching modes from the dodecyl groups; their deformation modes absorb between 1500 cm^{-1} and 1200 cm^{-1}. No CH_x vibrational modes were observed from the unfunctionalized SiNCs (Figure 3.4(a)). This indicates that the carbon on the functionalized SiNC surface originate from the organic ligands—not contaminates from the synthesis process.

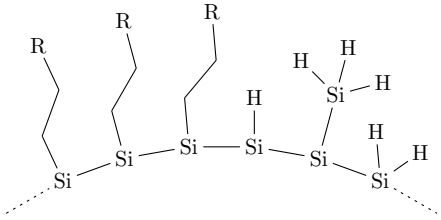

Figure 3.3: Hydrosilylated surface of SiNCs.

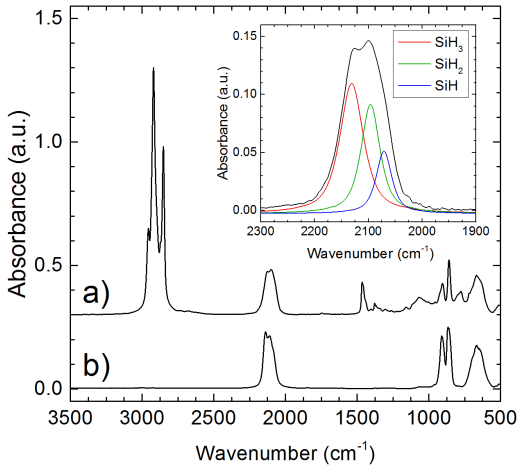

Figure 3.4: Typical FT-IR spectra of H-terminated SiNCs (a) and thermally-hydrosilylated SiNCs (b). Inset shows deconvoluted spectra of the silicon hydride stretching modes of hydrosilylated SiNCs: SiH_3 (red), SiH_2 (green) and SiH (blue).

Significant coverage with hydrogen is present on the SiNC surface before and after hydrosilylation (Figure 3.4). The triplet between 2200 cm^{-1} and 2000 cm^{-1} are characteristic SiH_x stretching modes. A deconvoluted spectrum of the SiH_x mode of the thermally-hydrosilylated SiNCs is shown in the inset of the figure. The peak at $\sim$ 2130 cm^{-1} is assigned to the SiH_3, and the SiH_2 and SiH modes appear at $\sim$ 2097 cm^{-1} and $\sim$ 2070 cm^{-1}, respectively. Due to the proximity and overlap of the symmetrical and asymmetrical modes, their peaks have been grouped in this study. The deformation modes of the SiH_x groups are visible between 1000 cm^{-1} and 800 cm^{-1} (96). The broad Si-O-Si peak between 1100 cm^{-1} and 1000 cm^{-1} indicates slight oxidation. Since insignificant Si-O-Si absorbance was observed in the unfunctionalized SiNCs, it is deduced that the oxidation occurred during the hydrosilylation reaction as a result of impurities in the nitrogen gas and/or solvents that were used.

Through FT-IR spectroscopy, it is possible to study changes in the surface chemistry of the SiNCs due to photobleaching. Hydrosilylated SiNCs were drop cast onto a diamond attenuated total reflectance (ATR) crystal and exposed to 365-nm light for up to 16 h. FT-IR spectra measured at 15-min intervals revealed the stability of alkyl ligands,

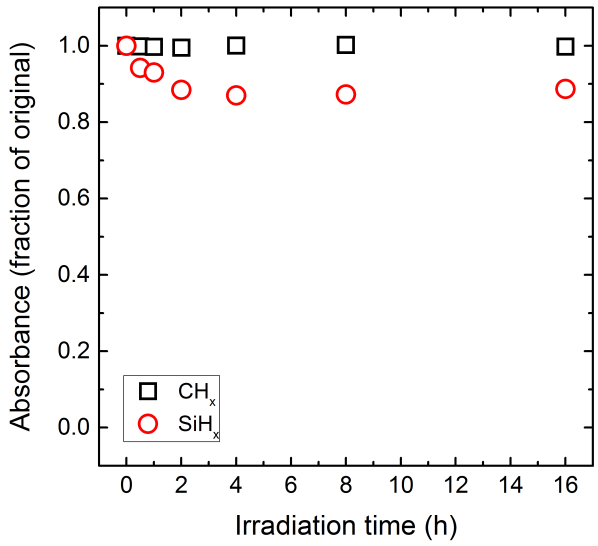

Figure 3.5: Time evolution of IR absorbance of CH_x and SiH_x groups during photobleaching on the ATR crystal.

or Si-C bonds, against UV irradiation (Figure 3.5); on the other hand, the coverage with silicon hydrides on the NC surface decreased with irradiation time. Unfortunately, due to the high absorptivity of silicon in the UV region, only a few monolayers of the SiNC film were exposed to the UV light, and an accurate fraction of hydrides cleaved from the surface could not be obtained from the data. However, knowing the stability of the dodecyl groups on the SiNC surface, FT-IR spectra of SiNCs irradiated *ex-situ* can be normalized to the total absorbance of the CH_x stretching modes.

SiNCs from the photoluminescence stability tests were drop cast onto the ATR crystal for FT-IR measurements. Figure 3.6 shows the IR absorbance of SiH_x stretching modes of the hydrosilylated SiNCs before and after UV irradiation (normalized to the integrated CH_x absorbance). The normalized data indicated $\sim$ 20 % decrease in the total SiH_x absorption intensity. The desorption of silicon hydrides can also be observed in the SiH_x deformation modes in the IR (Figure 3.7). Deconvolution of the SiH_x stretching modes reveals $\sim$ 10 % and 7 % reductions in both SiH_3 and SiH_2 groups, respectively, after UV exposure; little to no changes in the SiH absorption intensity was observed. These results are similar to thermal desorption experiments wherein the

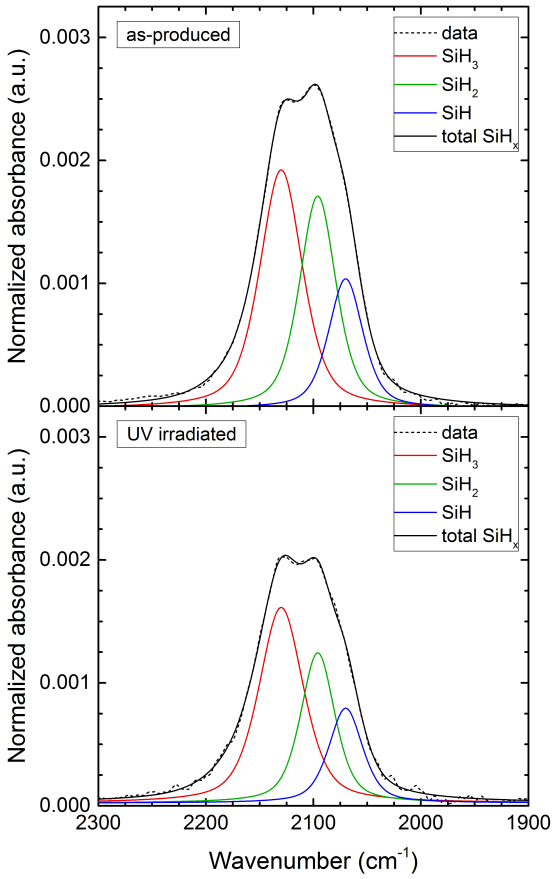

Figure 3.6: Deconvoluted FT-IR spectra of SiH_3, SiH_2, and SiH modes before (top) and after UV irradiation (bottom).

weaker SiH_3 groups were the first to desorb from the surface, followed by SiH_2 groups, and the SiH groups remained the most tightly bound to the NC (128; 104; 129). The PLQY steady-state reached at 4 h (Figure 3.1) represents the point at which all the weaker bonds susceptible to UV cleavage were removed from the surface.

SiH_3 groups are bound to the surface via a single Si-Si bond. The Si-Si bond, with a bond strength of 2.0 – 2.7 eV (129), is one of the weaker bonds on the NC surface; thus, 365-nm (3.4 eV) light has sufficient energy to homolytically cleave the Si-Si bond, yielding a volatile SiH_3 specie that desorbs from the NC (79; 130). The desorption

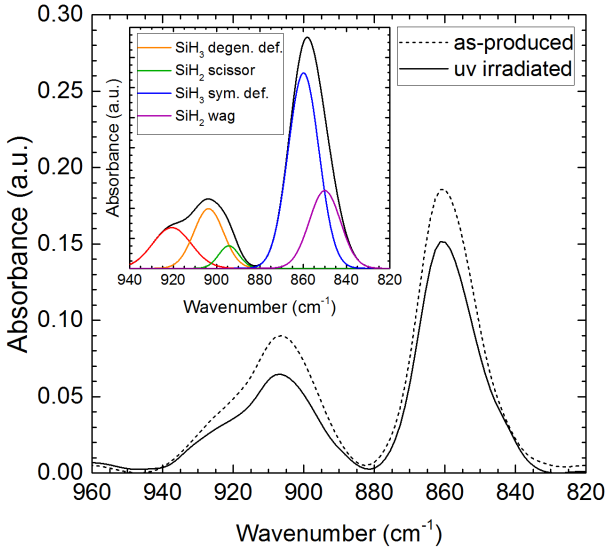

Figure 3.7: FT-IR spectra of the SiH_x deformation modes of as-produced (dotted black) and UV irradiated (solid black) SiNCs. The inset displays the deconvoluted spectrum, showing SiH_3 degenerate deformation (orange), SiH_2 scissoring (green), SiH_3 symmetrical deformation (blue), and SiH_2 wagging (purple) modes.

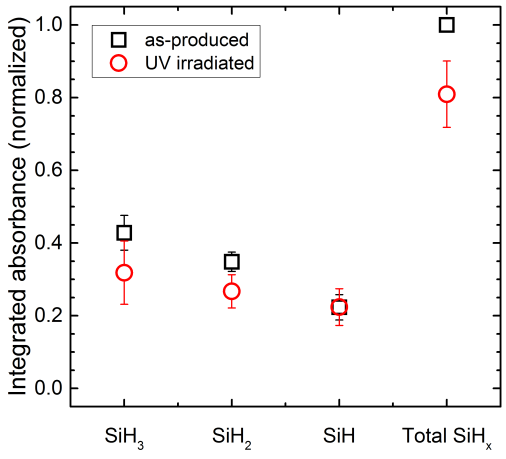

Figure 3.8: Integrated IR absorbance of silicon hydride stretching modes before and after UV irradiation.

reaction can be represented as:

$$SiH_3(s) \xrightarrow{\text{UV light}} Si^*(s) + SiH_3(g) \tag{3.1}$$

where (s) and (g) denote surface species and species in the gas phase, respectively, and superscript * denotes a surface dangling bond.

SiH_2 groups are doubly bonded to the silicon surface, and the strength of the Si-H bond is estimated to be $\sim$ 3.67 eV (104); thus, desorption of the SiH_2 groups seems less likely. However, steric interactions between neighboring SiH_3 and SiH_2 groups generate strain on the NC surface, weakening bonds (105). Gupta *et al.* estimate the Si-H bond in the SiH_2 group on an Si(100)-(2×1) surface to be $\sim$ 3.19 eV (104). These weakened bonds are, therefore, more susceptible to bond cleavage by the 3.4 eV light via the following process:

$$SiH_2(s) \xrightarrow{\text{UV light}} SiH^*(s) + H \tag{3.2}$$

The resulting increase in SiH may be offset by the reaction of the highly mobile monatomic hydrogen (131; 132) with a neighboring silicon hydride group to form hydrogen gas (H_2) that is desorbed from the surface. Hydrogen desorption in the form of H_2 was also observed by Pusel *et al.* in time-of-flight (TOF) analysis of the desorption products of silicon surfaces irradiated with a vacuum ultraviolet laser (VUV) (133).

With the understanding that the instability of SiQDs under UV light is a result of the generation of dangling bonds at the NC surface, we propose new pathway to create photostable SiQDs. Hydrosilylation is a well-established method for the passivation of silicon surfaces (101) and is a technique that can be employed for the passivation of the dangling bonds generated during photobleaching. EPR shows a decrease in unpaired electron density at the SiNCs surface by heating photobleached SiNCs above 150 ^oC in the presence of 1-dodecene (Figure 3.9). With 0.1 ml of 1-dodecene per 5 mg of SiNCs, an $\sim$ 25 % decrease in EPR signal was observed; with 0.5 ml of 1-dodecene, over 60 % reduction in EPR signal was observed. In the latter case, sufficient 1-dodecene was present to passivate the majority of the surface defects, nearly restoring the EPR signal to the initial (as-produced) intensity.

Passivation of the surface defects through the second hydrosilylation reaction also led to complete recovery of the photobleached SiQDs' photoluminescence (Figure 3.10).

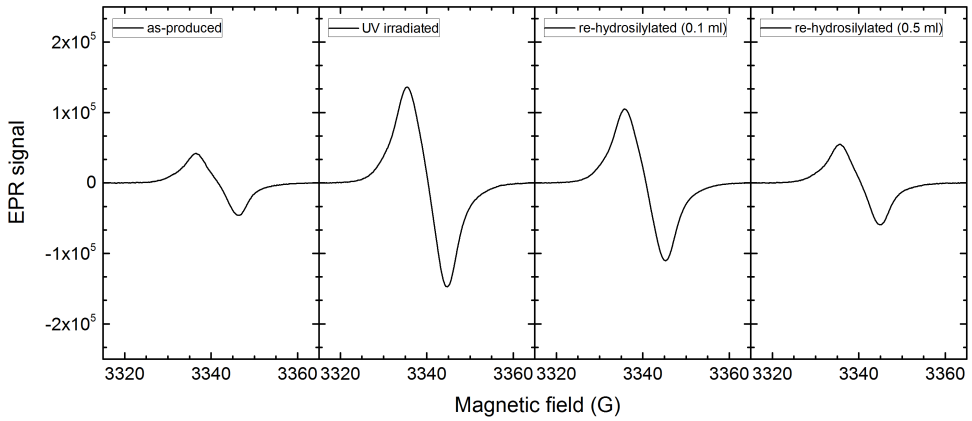

Figure 3.9: EPR spectra of SiNCs after second thermal hydrosilylation with 0.1 ml and 0.5 ml of 1-dodecene.

It should be noted that in the absence of 1-dodecene, heating of the SiNCs showed no recovery. This implies the recovery mechanism is dissimilar to the silicon network restructuring proposed for the healing of SWE defects in a-Si:H via thermal annealing (127).

Interestingly, further UV irradiation of the re-hydrosilylated SiNCs displayed no further degradation (Figure 3.10). This implies that the weaker bonds that are susceptible to the 365-nm light had been removed during the first UV exposure; the remaining surface is thus photostable. However, while the SiNCs are stable under 365-nm light, it is possible that exposure to light with energy greater than 3.4 eV will still result in photodegradation.

3.3 Conclusions

The photostability of thermally-hydrosilylated SiNCs produced in a nonthermal plasma has been studied. 365-nm light with a power density similar to that of the UV spectrum in AM1.5G sun was used as the irradiation source. UV irradiation resulted in $\sim$ 20 % (absolute) decrease in the SiQDs' PLQY, reaching a saturation of $\sim$ 40 % within 4 h. Similar to the SWE in a-Si:H, photodegradation was found to be a result of the creation of dangling bonds due to the breaking of silicon hydride bonds at the SiNC surface.

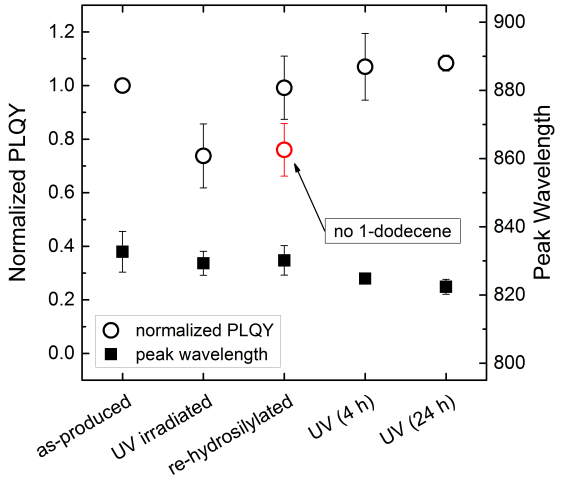

Figure 3.10: PLQY recovery of SiQDs after second thermal hydrosilylation with 1-dodecene (open circes). Further UV irradiation saw no decrease in PLQY. No recovery was observed when heated in the absence of 1-dodecene (red). The peak PL wavelengths are represented by the solid squares.

These dangling bonds act as centers for nonradiative recombination, resulting in the deterioration of the SiNCs' optical properties. The results demonstrate the inability of thermal hydrosilylation to remove the weaker silicon hydride bonds that are susceptible to UV cleavage. However, the PLQY of the photobleached SiNCs can be recovered via thermal hydrosilylation post UV irradiation. The resulting SiNCs are photostable and do not degrade under further irradiation. The photodegradation and recovery process is summarized in Figure 3.11.

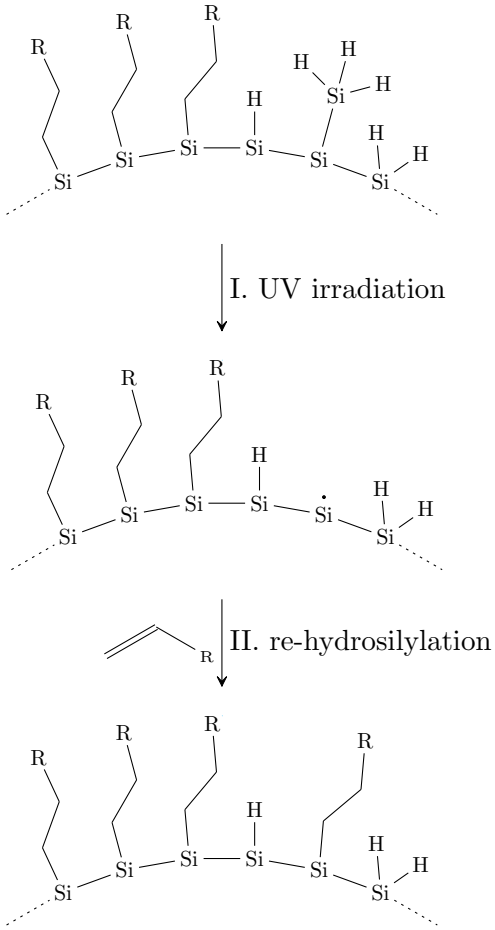

Figure 3.11: Summary of the photodegradation and recovery process. I. Irradiation of the SiNCs with UV light results in the cleavage of weaker silicon hydrides from the surface. II. Hydrosilylation of the photobleached SiNCs with 1-dodecene passivates the surface defects and leads to recovery of the SiNCs' PLQY.

3.4 Experimental

3.4.1 Synthesis

Silicon nanocrystals 4.2 nm in size were prepared using a nonthermal plasma reactor in a process that was previously reported (52). Argon and silane (5 % in helium) were flown into a flow-through reactor at 35 sccm and 13 sccm, respectively. The reactor

pressure pressure was maintained at 1.4 Torr using a butterfly valve. Dissociation of the silane was achieved using a nonthermal plasma that was excited by a 13.56 MHz radio-frequency power source. 100 sccm of hydrogen was injected into the afterglow of the synthesis plasma to passivate the SiNCs' surface, and the resulting hydrogen-terminated SiNCs were collected on a stainless steel mesh downstream of the plasma.

Post synthesis, Si-H bonds on the SiNCs' surface were partially replaced by stable Si-C bonds via a thermal hydrosilylation process using 1-dodecene (96 %) in a background solvent of mesitylene (98+ %). The collected SiQDs ($\sim$ 10 mg), along with the stainless steel mesh, were placed in a degassed mixture of the alkene (4 ml) and mesitylene (20 ml), and the solution was sonicated for 1 min to disperse the NCs. The resulting suspension was transferred into a glass boiling flask for the thermal hydrosilylation reaction and placed in a sand bath that was heated to 215 ^{o}C for over 3 hrs. A cold water condenser was used to prevent solvent evaporation. The resulting SiNC colloid was filtered through a 0.2 µm PTFE filter to remove agglomerates of unreacted NCs. Subsequently, the NCs were dried in a stream of nitrogen under vacuum prior to analysis.

Unwanted organic polymers formed during the thermal hydrosilylation process were removed by washing the SiNCs. Dried SiNCs were re-dispersed in 1 ml of toluene (99 %) and precipitated in 14 ml of acetonitrile (99.8+ %). Subsequently, the precipitated solution was sonicated for 2 mins and centrifuged at 4500 rpm for 10 mins. Finally, the supernatant was removed, and the process was repeated several times. All processes were performed in nitrogen atmosphere, and all solvents were degassed prior to usage.

3.4.2 UV irradiation

To mimic sunlight in the UV spectrum under AM1.5G conditions, a 100 W mercury-vapor lamp coupled with a 365-nm filter was used. SiQDs dispersed in toluene at a concentration of 5 mg/ml were exposed to 365-nm light at a power density of $\sim$ 4 mW/cm^2 for a duration of up to 24 hours for the photostability study. The irradiation was conducted in either vacuum or nitrogen atmosphere.

3.4.3 Characterization

Electron paramagnetic resonance (EPR). 5 mg of hydrosilylated, UV irradiated, and re-hydrosilylated SiQDs dispersed in 0.1 ml of toluene were added to three 5 mm diameter borosilicate glass tubes. The glass tubes were flame-sealed under vacuum to prevent air exposure. The EPR measurements were performed using Bruker Continuous Wave EleXsys E500 EPR spectrometer equipped with a X-band (9 GHz) microwave bridge and a spherical Super High-Q (SHQ) resonator. Measurements were acquired at a microwave attenuation of 30 dB. The field was centered at 3339 G with a sweep width of 100 G. 1024 points were taken in the range. A modulation frequency of 100 kHz and amplitude of 1 G were used. The time constant and conversion time were set at 40.96 ms. 10 scans were taken at room temperature (295 K) for each measurement.

Fourier Transform Infrared (FT-IR) spectroscopy. FT-IR measurements were performed on a Bruker ALPHA FT-IR spectrometer using the ATR single reflection module in a nitrogen-filled glovebox. SiNCs dispersed in toluene were drop cast onto the diamond ATR crystal and allowed to dry. 20 scans were taken for each measurement from 400 cm^{-1} to 4000 cm^{-1} at a resolution of 2 cm^{-1}. Time study of species desorption from the QD surface was performed by irradiating the drop-cast SiNC film with a 365-nm UV light. Measurements were acquired at 15-min intervals for over 16 h. Fitting of the FT-IR spectra was performed using Voight distributions. By fixing the position of the absorption peaks and their FWHM, time evolution of the absorption intensities of the individual peaks was obtained. The coefficients of determination, R^2, were used to determine quality of fits; all fits possessed R^2 values above 0.99.

Photoluminescence. Photoluminescence of SiQDs was measured using an Ocean Optics USB2000 spectrometer and integrating sphere setup whose absolute spectral response was calibrated using an Ocean Optics LS-1-CAL tungsten halogen light source. The validity of the calibration was verified using the fluorescence standard, Rhodamine 101 inner salt dispersed in ethanol. Photoluminescence was measured by irradiating SiQDs dispersed in 0.6 ml of toluene at a concentration of $\sim$ 1 mg/ml with a 395 nm LED. 2048 points were recorded in the range of 340 nm to 1024 nm. 60 scans were taken per measurement, and each measurement was smoothed using the boxcar

averaging technique set at a width of 5 points.

X-ray diffraction (XRD). Hydrosilylated SiQDs dispersed in toluene were drop cast onto a borosilicate glass substrate. The substrate was heated at 100 ^{o}C in nitrogen atmosphere for 1 h to ensure solvent evaporation. XRD was performed using a Bruker-AXS Microdiffractometer with 2.2 kW sealed Cu X-ray source. Three frames of 30 ^{o} width were collected with the first frame centered at 30 ^{o}. Each frame was scanned for 300 s. Debye-Scherrer fits of the integrated XRD patterns were used to determine the SiQD sizes.

Chapter 4

Photochemical hydrosilylation of silicon quantum dots

4.1 Introduction

The passivation of silicon surfaces has been an important topic of research for decades. Improved thermal and chemical stability has been observed with surfaces grafted with a monolayer of organic ligands (86; 87). Porous silicon (p-Si) and silicon nanocrystals (SiNCs) have also demonstrated intensified photoluminescence (82; 83; 85). The enhanced stability and optical properties are appealing for applications in optoelectronic devices (13; 14), bioimaging (134; 111), and photovoltaic spectrum modification systems (135; 136).

Hydrosilylation is a common technique used to attach organic ligands, such as alkenes and alkynes, onto hydrogen-terminated silicon surfaces (101). The reaction can proceed without the use of catalysts at elevated temperatures above 150 ^{o}C (97; 98) or photochemically at room temperature (85; 99; 100). Photochemical hydrosilylation presents several benefits over its thermal counterpart as removal of the potentially harmful thermal input widens the range of devices that can passivated and allows the photopatterning of self-assembled monolayers (82).

UV light with emission wavelengths shorter than 350 nm is believed to possess sufficient energy to cleave silicon hydride bonds (104; 105), leaving surface dangling bonds for alkyl attachment. Recent studies have shown that photoemission may play

a role in photochemical hydrosilylation reactions as well (106; 107). The absorption of a high-energy photon can eject an electron from the surface of the NC to an acceptor molecule, leaving a positive hole on the surface that is susceptible to attack by an alkene.

An alternate photochemical hydrosilylation pathway was discovered in 1998, where white light was used to graft organic ligands onto porous silicon (p-Si) surfaces (82). As white light ($>$ 400 nm) does not possess sufficient energy to cleave silicon hydride bonds, the authors proposed that an exciton-driven mechanism was responsible for the reaction (107). In porous silicon (as in SiNCs), the lifetime of an exciton is on the order of microseconds. The absorption of a photon lowers the activation energy required for the hydrosilylation reaction (137) and generates excitons that become localized in surface states. The reaction then proceeds via the nucleophilic attack of an alkene onto a localized hole, forming a Si-C bond (107; 138).

While extensive studies have been conducted on the mechanisms of light-induced hydrosilylation, little has been reported in the literature on the surface and optical properties of the functionalized silicon. Here, we study the surface chemistries and photoluminescence of thermally and photochemically-hydrosilylated, nonthermal plasma-produced (freestanding) SiNCs. The SiNCs exhibited enhanced emission, with photoluminescence quantum yields (PLQYs) nearing 60 %. Furthermore, SiNCs hydrosilylated photochemically showed improved photostability from those hydrosilylated thermally.

4.2 Results and Discussion

Silicon nanocrystals $\sim$ 4.2 nm in size were produced in the gas phase in a nonthermal plasma using silane as a precursor. Hydrogen was injected into the afterglow of the plasma to improve hydrogen passivation of the NCs' surfaces (83). Post synthesis, dodecyl groups were grafted onto the SiNC surface in the liquid-phase via three hydrosilylation pathways: (1) thermally, and photochemically using (2) halogen lamp or (3) mercury-vapor lamp. As seen in the emission spectrum included in Figure 4.1, the halogen lamp consists predominately of white light, with a weak component between 350 and 400 nm. The mercury-vapor lamp emits high-energy light in the blue-UV spectrum between 365 and 578 nm. The intensities of the light sources $<$ 700 nm were maintained at 10 mW/cm^2 during hydrosilylation.

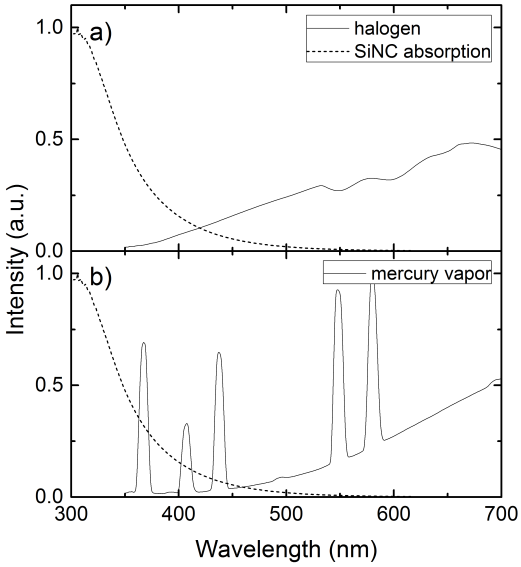

Figure 4.1: Emission spectra of halogen lamp (a) and mercury-vapor lamp (b). Dotted lines represent the absorption spectrum of the SiNCs.

The SiNCs' high surface-to-volume ratio enables the use of FT-IR spectroscopy for analysis of the hydrosilylated surfaces. Figure 4.2 shows a typical IR absorption spectrum of the nonthermal plasma-produced SiNCs before hydrosilylation. The SiNCs possess hydrogen-rich surfaces, exhibiting two distinct signals: (1) SiH_x stretching modes ~ 2100 cm^{-1}, and (2) SiH_x deformation peaks between 960 cm^{-1} and 810 cm^{-1}. The clean IR absorption spectrum implies a surface free of contaminates such as carbon, which has characteristic absorption peaks ~ 2900 cm^{-1}. Furthermore, the lack of Si-O-Si vibrational peaks at ~ 1100 cm^{-1} infers little oxidation occurred during synthesis. The hydrogen-rich, oxide-free surface provides an ideal platform for hydrosilylation reactions.

FT-IR spectra of the thermally and photochemically-hydrosilylated SiNCs (Figure 4.2) display strong CH_x absorption, revealing successful attachment of organic ligands onto the surface. The most prominent peaks ~ 2900 cm^{-1} originate from CH_x stretching modes of the dodecyl groups. The CH_x deformation modes absorb between 1500 cm^{-1} and 1200 cm^{-1}. The spectra lack the characteristic C=C stretching peak

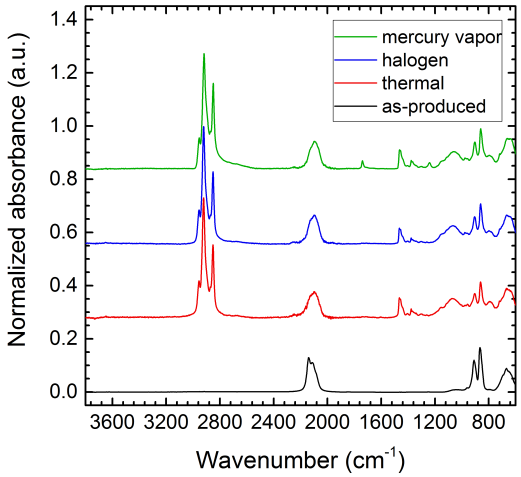

Figure 4.2: FT-IR spectra of as-produced SiNCs (black), SiNCs hydrosilylated thermally (red), SiNCs hydrosilylated using halogen lamp (blue), and SiNCs hydrosilylated using mercury-vapor lamp (green).

$\sim$ 1650 cm^{-1} from 1-dodecene, which validates the attachment of alkenes through the unsaturated vinyl group. Slight oxidation occurred during hydrosilylation as evident from the broad Si-O-Si vibrational peak at $\sim$ 1100 nm. Oxidation is likely a result of impurities in the chemicals or nitrogen gas used during hydrosilylation.

Successful hydrosilylation of p-Si and SiNCs has been shown to lead to the reduction of dangling bonds. The suppression of nonradiative recombination pathways through surface passivation can enhance band gap photoluminescence (115). The emission of as-produced nonthermal plasma-synthesized SiNCs is weak as a result of surface defects and charge transfer between neighboring SiNCs (139). Ensemble PLQY less than 5 % were measured for as-produced SiNCs dispersed in toluene. Thermal hydrosilylation of the SiNCs significantly enhanced photoluminescence. PLQYs of $\sim$ 59 % were measured for thermally-hydrosilylated SiNCs (hereafter referred to as t-SiNCs), comparable to previous reports by Jurbergs *et al.* (83). PLQYs nearing 60 % were also obtained via photochemical hydrosilylation; SiNCs hydrosilylated using halogen and mercury-vapor lamps (h-SiNCs and m-SiNCs, respectively) exhibited PLQYs of 56 % and 57 %, respectively. Relative to the as-produced SiNCs, $\sim$ 40 nm blueshift in peak photoluminescence wavelength was observed for all three hydrosilylated SiNCs (Figure 4.3b)—an effect of

the suppression of mid-gap dangling bond defects (78; 140).

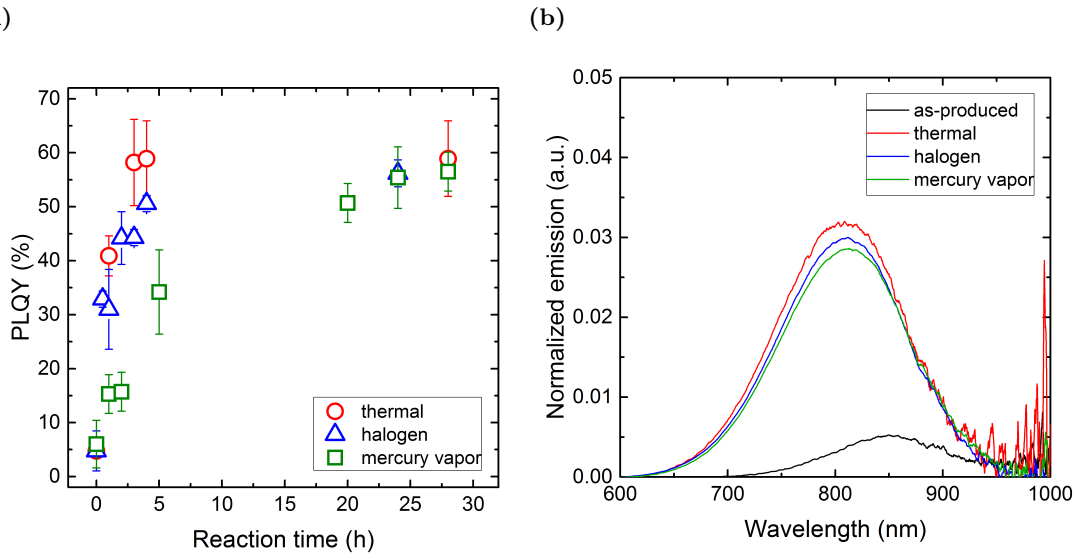

Figure 4.3: (a) Progress of hydrosilylation reactions as a function of PLQY. (b) Emission spectra of as-produced and hydrosilylated SiNCs.

While photochemical hydrosilylation can be as effective a technique as thermal hydrosilylation, the dependence on photon absorption decreases the reaction rate. The progress of thermal hydrosilylation, in terms of PLQY, is shown in Figure 4.3a. As seen in the figure, the reaction completed within 3 h, and the terminus PLQY of 59 % was attained. Halogen light-mediated hydrosilylation completed within 5 – 6 h. However, the reaction rate for mercury-vapor light-mediated hydrosilylation was considerably lower than that of the other two techniques—more than half a day was required for reaction completion. The low reaction rate is likely due to the high absorptivity of silicon in the blue-UV region. The penetration depth of UV light into silicon is limited to several nanometers; conversely, white light has a penetration depth of close to 1 mm (141). Furthermore, both photochemical reactions are hindered by light scattering; as-produced SiNCs form large agglomerates ($>$ 200 nm) in mesitylene, which increases the intensity of light scattered. The extensive reaction time of the photochemical hydrosilylation processes may be a deterrent for industrial applications, but it has been shown that the addition of electron acceptors can significantly increase the hydrosilylation rate (107).

The stability of the SiNCs in ambient conditions is also an important factor for industrial applications. In both optoelectronic and photovoltaic devices, the SiNCs will be subjected to high-energy irradiation from the sun. To test the SiNCs' photostability, NC colloids were subjected to 365-nm UV light at a power density of 10 mW/cm^2—several times that of the global AM1.5G standard. T-SiNCs exhibited significant optical degradation within 15 min of UV irradiation, experiencing close to 40 % reduction in PLQY (Figure 4.4). Photochemically-hydrosilylated SiNCs demonstrated enhanced stability to UV light. Less than 20 % reduction in PLQY was observed in h-SiNCs; m-SiNCs displayed insignificant degradation during the 2 h irradiation time, establishing superior stability against photodegradation. It should be noted that photostability can also be achieved by performing the hydrosilylation at 150 ^{o}C under mercury-vapor light exposure for 4 h.

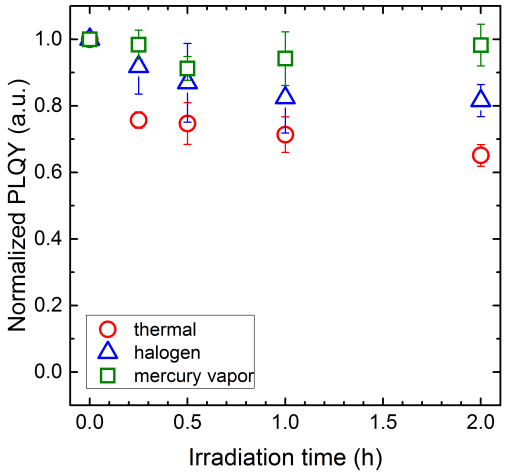

Figure 4.4: Photostability of hydrosilylated SiNCs irradiated with 365-nm light at 10 mW/cm^2 in N_2 environment.

Unfortunately, the enhanced stability of the photochemically-hydrosilylated SiNCs did not sustain in the presence of oxygen. With 20 ppm of oxygen (oxygen content in the glovebox), similar to the t-SiNCs, the photochemically-hydrosilylated SiNCs exhibited over 50 % degradation in PLQY within 2 h of UV irradiation (Figure 4.5). Oxide growth on silicon is proposed to proceed via the bonding of oxygen to surface dangling bonds

(Si-OH) or the bridging of oxygen between silicon atoms (Si-O-Si) (142; 143; 144); thus, a monolayer of dodecyl ligands is unlikely to prevent oxidation. Embedding the SiNCs in protective matrices such as a transparent polymer or via atomic layer deposition is a potential solution (145; 146).

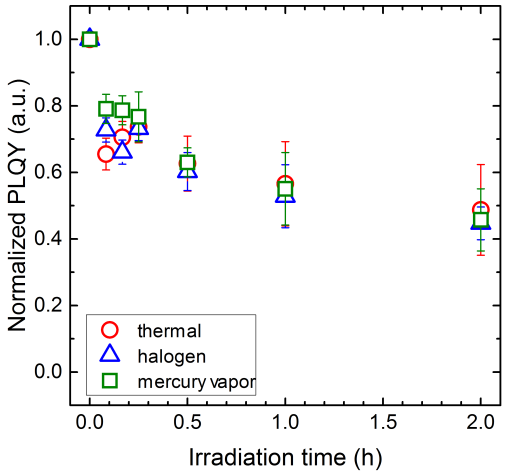

Figure 4.5: Stability of hydrosilylated SiNCs irradiated with 365-nm light at 10 mW/cm^2 in 20 ppm of O_2 in N_2.

The surface chemistries of the SiNCs play a significant role in their stability. The improved thermal and chemical stabilities of hydrosilylated SiNCs is believed to be a result of the replacement of weak Si-H bonds with stronger Si-C bonds (86; 87). However, limited by factors such as steric hindrance and self-termination of the radical chain propagation reaction (147; 148), the maximum alkyl substitution percentage is only 69 % (for Si(111) surfaces) (102). The incomplete surface grafting is evident in the FT-IR spectra (Figure 4.2). Strong IR absorbance by the t-SiNCs, h-SiNCs, and m-SiNCs at 2100 cm^{-1} reveals significant hydrides remaining on the surface post-hydrosilylation.

It has previously been shown that the instability of t-SiNCs under UV light is the result of the photocleavage of weak/strained surface hydrides. The resultant dangling bonds act as exciton trap sites and inhibit photoluminescence. For the m-SiNCs, the bonds susceptible to photocleavage are eliminated by the intense UV light of the

mercury-vapor lamp during hydrosilylation. However, as the halogen lamp emits weakly in the blue/near-UV region, the bonds vulnerable to breakage with the 365-nm light remain on the surface. Photodegradation thus occurs during UV irradiation due to the cleavage of these bonds.

The ability of the high-energy mercury-vapor light to attack the stronger surface bonds also generates additional alkene attachment sites, improving ligand coverage. As the initial surface hydride coverage of the pre-hydrosilylated SiNCs were similar, the alkyl coverages of the NCs hydrosilylated via the three different routes can be compared using the integrated IR absorbance of their CH_x and SiH_x stretching modes. Listed in Table 4.1 are the calculated CH_x:SiH_x ratios. Similar alkyl coverages were obtained for both t-SiNCs and h-SiNCs. In contrast, mercury-vapor light-mediated hydrosilylation demonstrates improved grafting efficiency—over 20 % higher CH_x:SiH_x ratio was measured for m-SiNCs.

Table 4.1: Surface ligand coverage

	CH_x:SiH_x ratio
Thermal	2.5
Halogen	2.6
Mercury vapor	3.2

*Each value is an average of > 3 samples. Measurements are within 11 % error.

The bonding structure of the surface ligands can provide some insights into the hydrosilylation mechanisms. It is widely believed that hydrosilylation results in additions of linear alkyl groups onto the surface. This is likely a result of steric hindrance between the surface moieties. However, β-bonding has been observed in SiNCs hydrosilylated photochemically (100; 149). This phenomenon may be an effect of the hydrosilylation mechanisms.

The fraction of α and β-bonded ligands can be estimated using the relative ratios of the CH_2 and CH_3 integrated areas, R, from ^{1}H-NMR spectroscopy (149). Figure 4.6 depicts typical NMR spectra of SiNCs produced through each hydrosilylation route. The CH_3, CH_2, and CH resonance peaks appear at 0.88 ppm, 1.25 ppm, and 1.43 ppm, respectively. The fraction of α-bonded ligands, x, can be calculated via Equation 4.1,

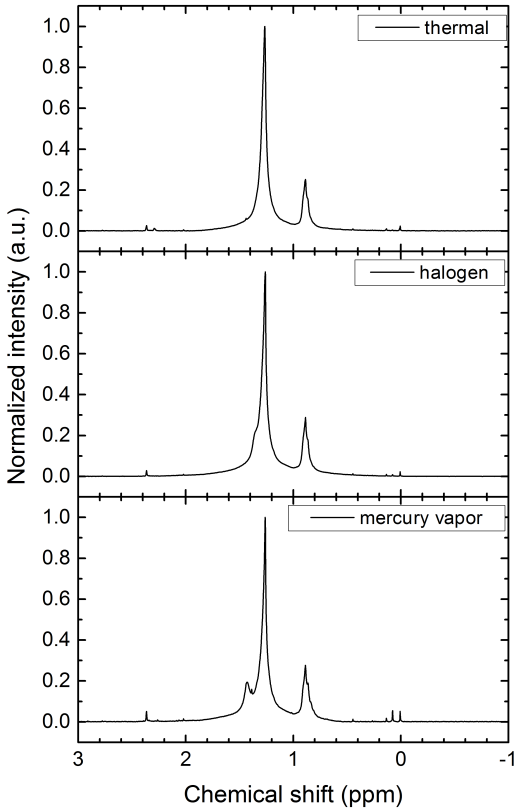

Figure 4.6: ^{1}H NMR spectra of hydrosilylated SiNCs showing CH (1.43 ppm), CH_2 (1.25 ppm) and CH_3 signals (0.88 ppm).

with the assumption that the alkyl groups remain whole, i.e. 12 carbons per surface-bonded ligand (L), during hydrosilylation.

$$R = \frac{A_{CH_2}}{A_{CH_3}} = \frac{2(L-1) + 2(1+x)(L-3)}{3x + 6(1-x)} \tag{4.1}$$

Table 4.2 lists the percentage of α-bonding in t-SiNCs, h-SiNCs, and m-SiNCs. The majority of the ligands on the t-SiNC's surface was α-bonded; < 5 % was branched. Similarly, only ~ 7 % of the ligands on the h-SiNCs exhibited β-bonding. However, a significantly higher percentage of β-bonding was observed in m-SiNCs; only 67 % of the m-SiNCs was α-bonded. Evidence of increased branching was also apparent from the distinct CH resonance peak in the m-SiNC spectrum that is absent in the t-SiNC and

h-SiNC NMR spectra.

Table 4.2: Surface ligand bonding structure

	% α-bonding
Thermal	96
Halogen	93
Mercury vapor	67

*Each value is an average of > 3 samples. Measurements are within 5 % error.

Variations in bonding structures have been attributed to the sizes and initial surface chemistries of the SiNCs, and structure of the alkenes/alkynes (100; 149). However, in this study, the properties of the pre-hydrosilylated SiNCs were similar; thus, any variations in the structures of the surface ligands is attributed to the hydrosilylation mechanisms.

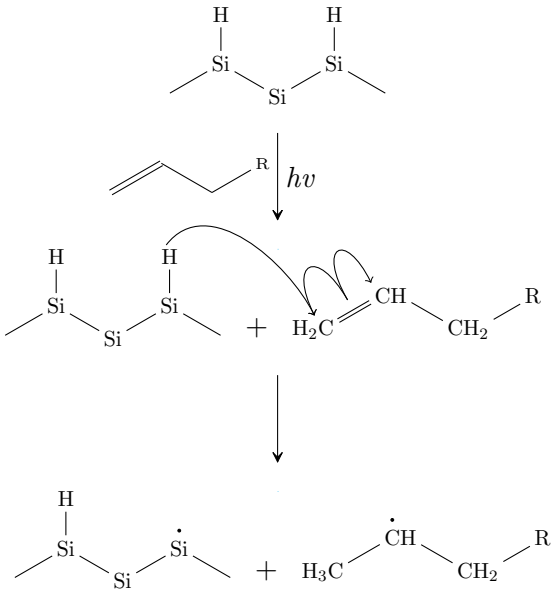

Figure 4.7: Figure depicting abstraction of hydrogen from SiNC surface by alkene molecule.

Two hydrosilylation mechanisms are found to be involved with UV light: (1) homolytic cleavage and (2) photoemission (85; 107). The increased β-bonding points to

homolytic cleavage as the predominant mechanism in the UV light-mediated hydrosilylation with the mercury-vapor lamp. Photocleavage of a surface Si-H bond leaves a silyl radical and a highly reactive hydrogen atom. The hydrogen atom can react with the vinyl group of an alkene molecule nearby, forming a new σ bond with a carbon atom. This reaction can lead to the (preferential) formation of the more stable secondary radical as depicted in Figure 4.7. The positively-charged β-carbon will react with a surface silyl radical to form the branched ligand detected via NMR spectroscopy. Furthermore, photoemission of an electron to a 1-dodecene molecule is difficult due to its low reduction potential (107; 150). Thus, it can be reasoned that the prevalent mechanism of the UV light-initiated hydrosilylation reaction in this study is based on the homolytic cleavage of silicon hydride bonds.

4.3 Conclusion

Silicon nanocrystals were successfully functionalized with dodecyl ligands via photochemical hydrosilylation. While as-produced SiNCs exhibit weak photoluminescence $<$ 5 %, the photochemically-hydrosilylated SiNCs displayed PLQYs nearing 60 %, comparable to t-SiNCs. The enhanced photoluminescence was a result of the suppression of dangling bond defects as observed in the blueshift of peak photoluminescence wavelength. Moreover, photochemically-hydrosilylated SiNCs demonstrate enhanced stability against UV irradiation, with SiNCs hydrosilylated via mercury-vapor lamp showing no degradation during exposure. FT-IR spectroscopy indicates that the improved stability of the m-SiNCs is likely a result of the homolytic cleavage of weak Si-H bonds during hydrosilylation. Passivation of the resultant radicals with alkyl ligands not only results in photostable surfaces, but also improved alkyl coverages in comparison to reactions mediated by heat or white light. Whilst the enhanced stability is an attractive property, the extended reaction time for mercury-vapor light-mediated hydrosilylation is an obstacle for industrial applications. Unfortunately, the reaction relies on photon absorption, and light scattering and low penetration depth reduces the amount of light incident on the NCs. The addition of electron acceptors to enhance photoemission may be a solution to the problem.

4.4 Experimental

4.4.1 Synthesis

Silicon nanocrystals were synthesized in the gas-phase using a nonthermal plasma. 13 sccm of 0.5 % SiH_4/He mixture and 35 sccm of Ar were fed into the flow-through reactor that was maintained at 1.4 Torr using a butterfly valve. A 13.56 MHz radio-frequency power source was used to ignite the plasma. The resulting SiNCs ($\sim$ 10 mg) were collected on stainless steel meshes sandwiched between two gate valves to prevent oxidation and transferred into N_2-filled gloveboxes.

Hydrosilylation. The SiNCs were dispersed in 4 ml of 1-dodecene and 20 ml of mesitylene. The cloudy dispersion was sonicated for 1 min and transferred into a 100 ml Pyrex round bottom boiling flask (a fused quartz flat bottom flask was used for mercury-vapor light-mediated hydrosilylation) with an attached water condenser on the Schlenk line. *Thermal hydrosilylation.* The flask was buried in a sand bath and heated to 215 ^{o}C for 3 h under constant N_2 flow. *Halogen light-mediated hydrosilylation.* A 300 W halogen lamp was used to irradiate the solution for up to 24 h. The solution was stirred at 500 rpm during irradiation. *Mercury vapor light-mediated hydrosilylation.* Two 100 W mercury-vapor lamps were used to irradiate the solution for up to 24 h. The solution was stirred at 500 rpm during irradiation, and the temperature of the flask was maintained at 60 ^{o}C. Power densities of $\sim$ 10 mW/cm^2 (of light $<$ 700 nm) were used for both photochemical reactions. All solvents were dried and degassed prior to usage.

Purification. The resulting colloid from the hydrosilylation reaction was filtered using a 0.2 μl PTFE filter, and the solvents were evaporated under vacuum and constant N_2 flow. The dried SiNCs were redispersed into 1 ml of toluene. Acetonitrile was added to the colloid to precipitate the NCs. The solution was centrifuged at 4500 rpm for 15 mins. The process was repeated 3 times.

4.4.2 Characterization

Fourier Transform Infrared (FT-IR) spectroscopy. FT-IR spectroscopy was performed using a Bruker ALPHA FT-IR spectrometer with the platinum ATR single reflection module in a N_2-filled glovebox. SiNCs dispersed in toluene were drop casted onto the ATR crystal. Each measurement was averaged over 20 scans.

Nuclear Magnetic Resonance (NMR) spectroscopy. Proton NMR spectroscopy was performed using a Varian Inova VAC-300 spectrometer. SiNCs were dispersed in deuterated chloroform at a concentration of 5 mg/ml, and flame-sealed in a NMR precision tube. 128 scans were taken per measurement.

Photoluminescence. Photoluminescence of the SiNCs was measured using an Ocean Optics USB2000 spectrometer and integrating sphere setup. The absolute irradiance of the setup was calibrated using an Ocean Optics LS-1-CAL tungsten halogen light source. Quantum yield measurements were verified using the fluorescence standard Rhodamine 101 inner salt dispersed in ethanol. SiNCs were dispersed in toluene at a concentration of 1 mg/ml and irradiated with a 395-nm LED. 60 scans were taken per measurement.

X-ray Diffraction (XRD). XRD was performed on SiNCs drop casted onto borosilicate glass substrates. A Bruker-AXS Microdiffractometer with 2.2 kW sealed Cu X-ray source was used. SiNC sizes were determined using Debye-Scherrer fits of the integrated XRD patterns. Corundum standard was used to calculate equipment broadening.

Chapter 5

Gas-phase functionalization of silicon quantum dots

5.1 Introduction

The grafting of organic ligands onto silicon surfaces is a common method to improve the material's stability (86; 87). For porous silicon (p-Si) and silicon quantum dots (SiQDs), surface passivation with 1-alkenes have also led to enhanced optical properties (82; 83; 85). Specifically, thermally-hydrosilylated, nonthermal plasma-synthesized SiQDs have exhibited photoluminescence quantum yields (PLQYs) exceeding 60 % (83).

Surface passivation of freestanding silicon nanocrystals (SiNCs) often occurs after the synthesis reaction. For example, to obtain 60 % QY, SiQDs synthesized in a nonthermal plasma are dispersed in a mixture of 1-alkene and mesitylene and heated in a sand bath maintained at 215 ^{o}C for $>$ 3 h. Unfortunately, the hydrosilylation reaction is time consuming and is a wasteful process. They often require excess solvents that must be evaporated after reaction completion, and a free flow of cooling water is needed to prevent solvent loss during the reaction.

Mangolini *et al.* devised an all gas-phase approach for the in-flight passivation of SiNCs in a two-stage nonthermal plasma reactor (5) (Figure 2.8). SiNCs synthesized in a first nonthermal plasma are delivered into a second surface passivation plasma. Vaporized organic molecules are injected into the second plasma by bubbling argon gas into the liquid. Hot electrons in the second plasma are able to dissociate the molecules

and create radicals that react with the SiNCs.

Anthony *et al.* further simplified the design by combining the two plasmas into one (6) (Figure 2.9). The nonthermal plasma reactor was redesigned to include an expansion region after the synthesis plasma. In the expansion region, the diminished plasma intensity allows the selective dissociation of the weaker C=C bonds in the alkene. This plasma synthesis/functionalization technique permitted the fabrication of simple inorganic LEDs entirely in the gas-phase (6). Peak quantum efficiencies of ~ 0.02 % were attained. The low efficiency was attributed to the absence of charge transport layers and weak SiNC optical properties. PLQYs less than 10 % were measured from the gas-phase functionalized SiNCs produced in both the aforementioned reactors.

In order to improve the quantum efficiencies of the LEDs, the optical properties of the SiQDs must be enhanced. Here, we investigate the origin of the weak photoluminescence from the gas-phase functionalized SiNCs. The plasma process resulted in inadequate surface passivation; reactive alkyl radicals were physisorbed onto the NCs; unfortunately, a large fraction of the radicals were unable to chemically bond to the surface. Post-synthesis photochemical reactions using mercury-vapor and halogen light were examined to improve the SiNCs' emission. PLQYs approaching 60 % were obtained by irradiating films of gas-phase functionalized SiNCs using halogen light. It is anticipated that the ease and success of the gas-phase functionalization process in producing brightly-emitting SiNCs will drive the replacement of conventional liquid-phase reactions.

5.2 Results and discussion

Silicon nanocrystals were synthesized in the low-pressure, nonthermal plasma depicted in Figure 5.1 using silane (SiH_4) as a precursor. Imitating the work by Anthony *et al.*, 1-dodecene was injected into the expansion region of the plasma by bubbling hydrogen gas into the liquid to passivate the SiNC surface with hydrocarbon chains (6). The resulting SiNCs were collected onto silicon or glass substrates via inertial impaction (8) for characterization.

Two major surface groups, (1) hydrocarbons and (2) silicon hydrides, were discerned

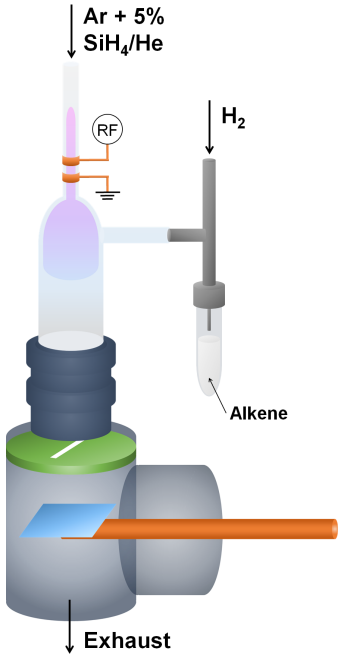

Figure 5.1: Nonthermal plasma reactor for NC synthesis and in-flight alkyl passivation. Image adapted from (6).

from the FT-IR spectrum of gas-phase functionalized SiNCs (Figure 5.2), which indicates the successful addition of dodecyl groups onto the surface. Similar peaks were detected from liquid-phase, 1-dodecene hydrosilylated SiNCs. In comparison, SiNCs produced without alkene injection is terminated with only hydrogen from the silane precursor and hydrogen gas. The characteristic SiH_x stretching modes appear at $\sim$ 2100 cm^{-1}; the triplet consists of the absorption from SiH_3, SiH, and SiH groups at 2141 cm^{-1}, 2109 cm^{-1}, and 2080 cm^{-1}, respectively. The SiH_x stretching modes of the functionalized SiNCs are red-shifted by $\sim$ 10 cm^{-1} from the as-produced SiNCs. The shift is a result of the relaxation of the SiH_x bonds induced by the spatial separation of the neighboring SiNCs created by the long organic ligands. The strong CH_x vibrational peaks between 3100 cm^{-1} and 2700 cm^{-1} arise from the dodecyl moieties on the SiNC surface.

Similar to previous reports, PLQYs less than 5 % were measured on average for the gas-phase functionalized SiNCs (5; 6). In comparison, PLQYs over 60 % can be obtained

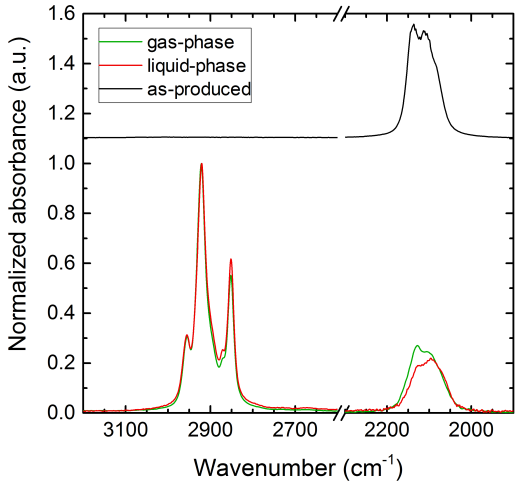

Figure 5.2: FT-IR spectra of gas-phase functionalized SiNCs (green) in comparison with unfunctionalized, hydrogen-terminated SiNCs (black) and liquid-phase hydrosilylated SiNCs (red).

via liquid-phase hydrosilylation of similarly-sized, nonthermal plasma-synthesized SiNCs (83). The weak photoluminescence may be a result of the inferior alkyl surface passivation of the gas-phase functionalized SiNCs; 20 to 40 % lower hydrocarbon density (calculated from the integrated IR absorbance) than liquid-phase hydrosilylated SiNCs was measured.

The sample-to-sample discrepancies in hydrocarbon densities, or grafting efficiencies, of the gas-phase functionalized SiNCs were the result of inconsistencies in the 1-dodecene injection process. The vapor pressure of 1-dodecene ($\sim$ 0.02 Torr at room temperature) is considerably lower than the pressure in the reactor ($\sim$ 1.5 Torr). It was, thus, necessary to bubble hydrogen gas into the liquid (similar to an atomization process) to introduce the molecules into the plasma. Evident from a coating of liquid on the inner surface of the reactor tube, the dodecyl molecules were not vaporized, but were in liquid form, when injected into the reactor. In addition to the large degree of inconsistency, the liquid in the reactor also resulted in significant energy losses in the plasma—a portion of the energy input was needed to vaporize the liquid.

The use of 1-alkenes with vapor pressures higher than the reactor pressure improved

the reliability of the process and prevented contamination of the reactor. 1-decene, 1-octene, and 1-hexene were investigated. The vapors were carried into the plasma using hydrogen gas—without bubbling the gas into the liquid. FT-IR spectra of these SiNCs reveal the presence of hydrocarbons on the surface (Figure 5.3). All SiNCs also dispersed readily into non-polar solvents to form clear colloids. Flattening of the CH_x IR absorption peaks between 3100 cm^{-1} and 2700 cm^{-1} and reduction in CH_x to SiH_x integrated ratios were observed from the IR spectra of 1-dodecene to 1-hexene functionalized SiNCs. They are attributed to the shortened hydrocarbon chains (from 12 to 6 carbons), not the grafting efficiencies of the functionalization process.

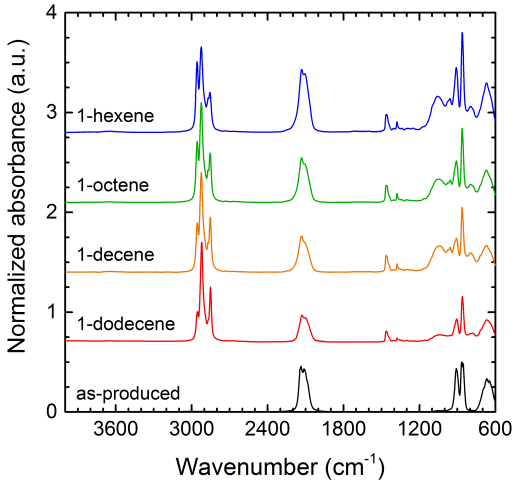

Figure 5.3: FT-IR spectra of as-produced SiNCs and NCs functionalized with 1-dodecene, 1-decene, 1-octene, and 1-hexene.

Optical measurements of the gas-phase functionalized SiNCs suggested increase in grafting efficiencies with high vapor pressure alkenes. Table 5.1 lists the PLQYs and peak luminescence wavelengths of SiNCs produced from alkenes of different vapor pressures. The use of 1-decene, whose vapor pressure is slightly higher than the reactor pressure, led to four to five-fold increase in PLQY from 1-dodecene. Similarly, 1-octene and 1-hexene functionalized SiNCs exhibited PLQYs nearing 25 %. Due to their higher vapor pressures, higher volumes of 1-octene and 1-hexene were used per unit of SiNCs than 1-decene. However, no improvements in PLQY from hexene-functionalized SiNCs

were found. This implies the grafting efficiency is limited by the plasma process.

Table 5.1: Vapor pressures of 1-alkenes and photoluminescence of the respective gas-phase functionalized SiNCs

Alkene	Vapor pressure (Torr)	PLQY (%)	Peak PL wavelength (nm)
1-dodecene	0.019	5	775
1-decene	1.67	23	768
1-octene	17.4	24	769
1-hexene	183.8	22	787

As previously mentioned, the plasma process generates reactive radicals. The growth of C:H layers at low temperatures is believed to be initiated by the adsorption of reactive species (151; 152; 153). If unreacted, these adsorbed radicals act as exciton trap sites on the surface, inhibiting radiative recombination and suppressing photoluminescence. The first evidence of physisorption was from the synthesis paper by Mangolini *et al.* The group obtained $\sim$ 50 % PLQY from gas-phase functionalized SiNCs that were heated in solution (in the absence of additional 1-dodecene) ((5)), which indicates that the dodecyl molecules were only weakly bound to the NC surface—not covalently bonded. When dispersed in solution, these radicals can desorb from the surface, which should lead to an improvement the SiNCs' photoluminescence. Four-fold increase in PLQY was observed from gas-phase (1-dodecene) functionalized SiNCs dispersed in chloroform for an extended time (Figure 5.4).

Further evidence of molecular adsorption is found in the peak broadening in the ^{1}H NMR spectrum of the gas-phase functionalized SiNCs (Figure 5.5). Three resonance peaks arising from the organic ligands are observed. Peaks at 0.9 ppm, 1.3 ppm, and 1.5 ppm (relative to the tetramethylsilane (TMS) reference peak at 0 ppm) represent the resonant frequencies of CH_3, CH_2, and CH, respectively.

The CH peak in the NMR spectrum indicates the presence of branched ligands from the reaction of the β-carbon atom of the alkene molecule to the surface silicon atom, contrary to the common believe that hydrosilylation results in linear alkyl chains. β-bonding was also recently observed in SiNCs produced in UV light-mediated

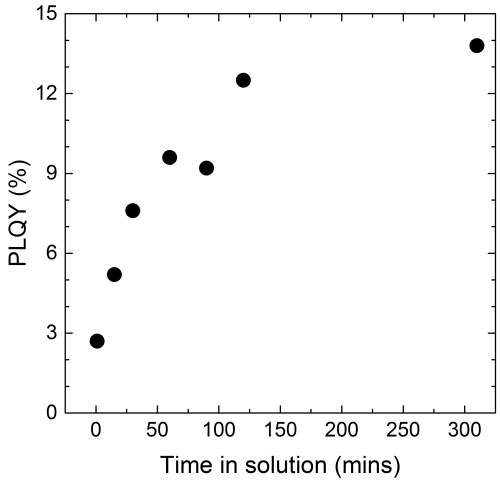

Figure 5.4: PLQY of gas-phase functionalized SiNCs as a function of time dispersed in chloroform.

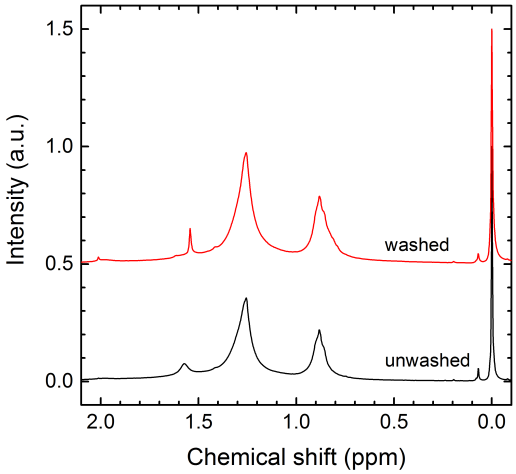

Figure 5.5: ^{1}H NMR resonance spectra of washed and unwashed gas-phase functionalized SiNCs.

hydrosilylation processes (100; 149). The presence of β-bonded moieties on the plasma-functionalized SiNCs suggests that both primary and secondary alkyl radicals (indicated by blue and red color in Figure 5.6, respectively) were produced in the plasma. The

respective surface structure resulting from these radicals are indicated by cyan and magenta in the figure. From the ratio of the integrated CH_2 and CH_3 NMR peaks, it was inferred that almost 50 % of the surface ligands are branched. It was noted that the injection of hydrogen gas was necessary; the replacement of hydrogen with helium or argon gas reduced the grafting efficiency, and PLQYs < 4 % were measured.

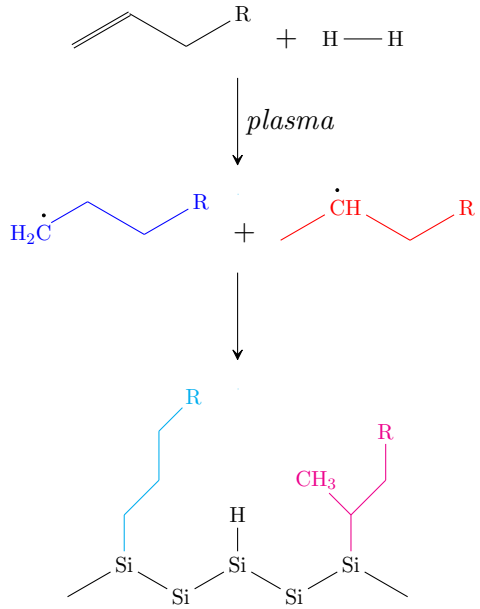

Figure 5.6: Schematic of the functionalization mechanism of SiNCs in a nonthermal plasma. Both primary (blue) and secondary (red) radicals are produced in the plasma, resulting in both linear (cyan) and branched (magenta) moieties, respectively, on the SiNC surface.

Broadening of the CH_2 and CH_3 peaks is a result of the free molecular motion of the tail of the organic ligands. However, the broad CH peak is unexpected. Covalent bonding of the branched ligands to the NC surface should inhibit C-H motion and produce a sharp NMR peak. Thus, the broad CH peak is indicative of the existence of weakly bound molecules. Removal of the physisorbed molecules by washing the gas-phase functionalized SiNCs with acetonitrile leaves covalently-bonded alkyl groups on the surface and reveals a sharp peak in the ^{1}H NMR spectrum.

The physisorbed alkyl molecules can be attached to the SiNC surface via hydrosilylation—a common technique for passivating silicon surfaces with unsaturated molecules (103).

In these reactions, reactive sites are created on the NC surface thermally, at temperatures above 150 ^{o}C, or photochemically, using UV light or white light. All three methods have resulted in SiNCs with PLQYs nearing 60 % previously (83) (see Chapter 4). Heating of the gas-phase functionalized SiNCs evaporated the adsorbed molecules, and no significant improvements in PLQY were observed. However, photochemical reactions can take place at room temperature, which reduces the risk of vaporizing the adsorbed molecules.

To perform the photochemical hydrosilylation reactions, thin films (< 1 μm) of gas-phase functionalized SiNCs were impacted onto borosilicate glass substrates. In a nitrogen-filled glovebox, the films were irradiated with a mercury-vapor lamp (UV light) or a halogen light source (white light) (see Figure 4.1 for the emission spectra). The evolution of the SiNCs' PLQY is shown in Figure 5.7. 10–15 % increase in PLQY was observed when the SiNC films were irradiated with UV light. On the other hand, significant enhancement in PLQY was achieved in less than 2 h when the SiNC films were irradiated with white light—PLQYs nearing 60 % were measured. In both processes, little to no changes in peak photoluminescence wavelength ($\sim$ 780 nm) were observed, which indicates preservation of the SiNC's core during irradiation. A photograph of the gas-phase functionalized SiNCs before and after white light treatment can be seen in Figure 5.8.

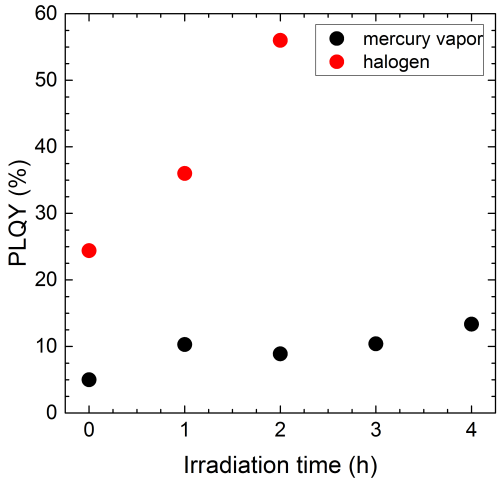

Figure 5.7: PLQY of light-irradiated, gas-phase functionalized SiNCs.

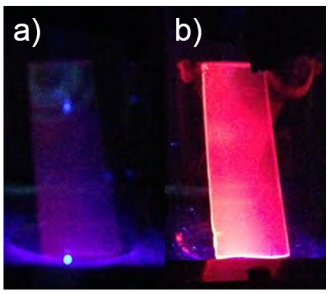

Figure 5.8: Gas-phase functionalized SiNCs under UV light (a) before and (b) after white light irradiation.

The weak PLQY enhancement with the UV light-irradiated thin films is likely a result of the small penetration depth of high-energy light into silicon. PLQYs nearing 60 % can also be obtained when the gas-phase functionalized SiNCs are irradiated with UV light in solution. 400 nm light is only able to penetrate several monolayers, while 600–700 nm light has a penetration depth of $\sim$ 0.5 mm (141).

5.3 Conclusions

Photoluminescence quantum yields approaching 60 % have been achieved from gas-phase alkyl-functionalized SiNCs. In the nonthermal plasma, alkyl radicals in the form of primary and secondary radicals are created by electron impact dissociation of the injected alkenes. A portion of these alkyl radicals are simply physisorbed onto the surface of the NCs, and they act as exciton trap sites that inhibit radiative recombination. Irradiation of the NCs (with the physisorbed radicals) initiates hydrosilylation reactions. SiNC produced from UV light-irradiated films exhibit weak photoluminescence due to the small penetration depth of the light source. However, white light has a penetration depth close to 1 mm and produced SiNCs with PLQYs nearing 60 %. The elimination of uneconomical solvent use may promote the use of the nonthermal plasma technique in industrial applications.

5.4 Experimental

5.4.1 Synthesis and deposition

Silicon nanocrystals were synthesized in the gas-phase using a nonthermal plasma. 6 sccm of 5 % SiH_4/He mixture and 35 sccm of Ar were fed into the flow-through reactor that was maintained at 1.4 Torr using an adjustable slit orifice. 1-alkene vapors were introduced into the reactor through a continuous flow of hydrogen gas (100 sccm). A needle valve was used to control the 1-alkene feed rate. A 13.56 MHz radio-frequency power source with a power input of 60 W (nominal) was used to ignite the plasma. The resulting SiNCs were deposited onto borosilicate or silicon substrates and transferred in a gate valve into N_2-filled gloveboxes to prevent oxidation.

5.4.2 Characterization

Fourier Transform Infrared (FT-IR) spectroscopy. Gas-phase functionalized SiNCs were deposited on gold-coated silicon wafers. FT-IR spectroscopy was performed using a Bruker ALPHA FT-IR spectrometer with the DRIFT (diffuse reflection) module in a N_2-filled glovebox. Washed SiNCs were measured using a platinum ATR single reflection module by drop casting SiNCs dispered in chloroform onto the ATR crystal. Each measurement was averaged over 20 scans.

Nuclear Magnetic Resonance (NMR) spectroscopy. Proton NMR spectroscopy was performed using a Varian Inova VAC-300 spectrometer. SiNCs were dispersed in deuterated chloroform and flame-sealed in a NMR precision tube. 512 scans were taken per measurement.

Photoluminescence. Photoluminescence of the SiNCs was measured using an Ocean Optics USB2000 spectrometer and integrating sphere setup. The absolute irradiance of the setup was calibrated using an Ocean Optics LS-1-CAL tungsten halogen light source. Quantum yield measurements were verified using the fluorescence standard Rhodamine 101 inner salt dispersed in ethanol. SiNCs were dispersed in toluene at a concentration of 1 mg/ml and irradiated with a 395-nm LED. 60 scans were taken per measurement.

Chapter 6

Luminescent, water-soluble silicon quantum dots via microplasma surface treatment

6.1 Introduction

Quantum dots are emerging as new materials for biological fluorescent imaging. Silicon quantum dots (SiQDs), with their broad absorption, narrow and size-tunable emission, and potential nontoxicity, are well-suited for this application. Most significantly, QDs have demonstrated enhanced stability compared to conventional organic fluorophores (39).

An obstacle to the implementation of SiQDs in biological systems is the synthesis of hydrophilic QDs that exhibit band-gap emission. Several approaches have been used to modify silicon surfaces. Allylamine-functionalized silicon nanocrystals (SiNCs), despite being water-soluble, exhibit blue emission from defect states (93). Size-tunable emission was observed from silica-coated SiNCs produced by oxidizing red-emitting SiNCs in hydrogen peroxide (94); blue-emitting SiNCs were produced within 24 h of reaction. Silica-coated SiNCs were also produced via microplasma-treatment of free-standing SiNCs in water or ethanol (112). The plasma-treated SiNCs demonstrated stability for up to 20 days in water. Unfortunately, the photoluminescence quantum

yields (PLQYs) of the aforementioned SiNCs were either weak (< 5 %) or unreported.

In this work, we engineered highly-luminescent, water-soluble SiQDs with size-tunable emission. Hydrogen-terminated SiNCs were synthesized in a low-pressure, nonthermal plasma. Using an atmospheric-pressure, nonthermal microplasma, the hydrophobic SiNCs were treated in water. The resulting hydrophilic SiQDs exhibited water-stable PLQYs nearing 50 %. Plasma chemistry was changed in the microplasma for preliminary assessment of the chemical mechanism(s) involved in the creation of water-stable SiNCs.

6.2 Results and discussion

Silicon nanocrystals 5.9 nm in size were synthesized in a low pressure, nonthermal plasma reactor (Figure 1.2) using silane SiH_4 as a precursor (52) and treated in water using a RF-powered, atmospheric pressure, argon microplasma (154). The experimental setup for the microplasma surface treatment is shown in Figure 6.1. Hydrogen-terminated SiNCs were wetted in ethanol to aid initial dispersion into water. The NCs were then treated in water under ambient conditions. Plasma parameters, such as input power, gas flow rate, and plume distance from liquid, were adjusted to produce water-soluble, luminescent SiNCs.

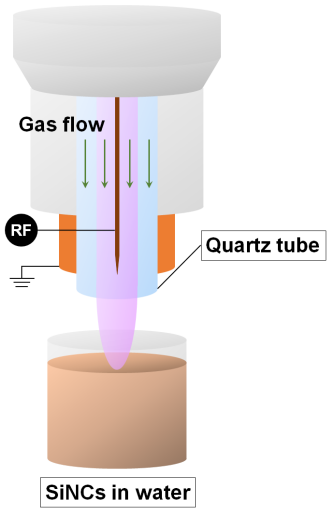

Figure 6.1: Schematic of microplasma gun for surface treatment of SiNCs.

Silicon nanocrystals produced using silane possess hydrogen-rich surfaces as evident in the Fourier transform infrared (FT-IR) spectrum in Figure 6.2. The weak Si-O-Si vibration at $\sim$ 1100 cm^{-1} suggests little oxidation occurred during synthesis. The as-produced SiNCs suffer from several limitations that render them incompatible for biological applications. Firstly, the hydrogen-terminated surface (Figure 6.2) is highly hydrophobic. As seen in Figure 6.3a, the SiNCs tend to float on water. Moreover, unlike the self-limiting oxidation reaction that occurs in ambient conditions, water is able to diffuse deep into the SiNC's core; within hours, the SiNC solution would turn from brown to transparent. Lastly, nonradiative defects at the surface of the as-produced SiNCs suppress luminescence—PLQYs less than 5 % were measured on average.

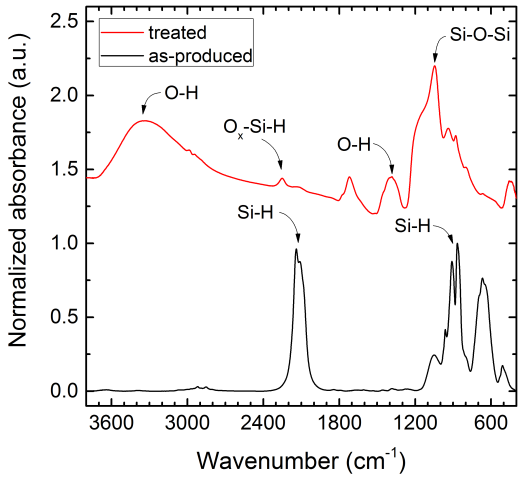

Figure 6.2: FT-IR spectra of SiNCs before (black) and after (red) microplasma treatment.

The microplasma-treated SiNCs were highly oxidized. FT-IR spectroscopy, energy-dispersive X-ray spectroscopy (EDS) in the transmission electron microscope (TEM), and Auger spectroscopy detected silicon and oxygen atoms in the treated SiNCs. According to EDS and Auger measurements, almost 50 % of the SiNCs comprised of oxygen atoms. Hydrogen and carbon were the only other elements identified from the three different spectroscopy techniques. The high purity of the SiNCs highlights one of the main benefits of microplasma processing.

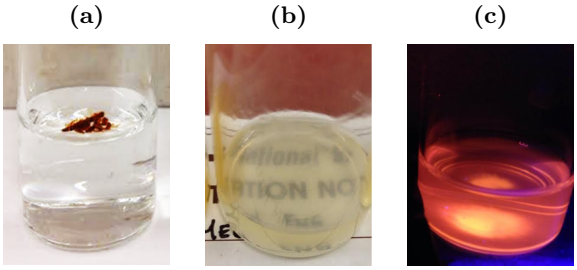

Figure 6.3: SiNCs in water: (a) hydrogen-terminated SiNCs, (b) microplasma-treated SiNCs at 5 mg/ml, and (c) microplasma-treated SiNCs under UV light.

The large fraction of oxygen atoms detected in the microplasma-treated SiNCs indicates a thick oxide shell is grown on the surface. For a 5.9 nm SiNC, an estimated 35 % of the atoms lie on the surface (77), which is less than the fraction of oxygen atoms measured in the treated SiNCs. Further evidence of shell growth is provided in the FT-IR spectrum (Figure 6.2). Strong O-H and Si-O-Si vibration, and a weak SiH_x absorption was observed; this suggests the microplasma treatment had replaced all surface hydrides with oxide species.

The silica shell imparted water solubility onto the SiNCs. Figure 6.3b shows a picture of a translucent colloid of treated SiNCs in water. Dynamic light scattering (DLS) spectroscopy revealed $\sim$ 200 nm particles in the colloid of ethanol-wetted, hydrogen-terminated SiNCs (non-wetted SiNCs do not disperse into water). During the microplasma treatment, the particle sizes decreased with time; after 1.3 h, the particles were reduced to 60 – 80 nm. Transmission electron microscopy (TEM) revealed these particles were agglomerates of 5 – 6 nm SiNCs (inset of Figure 6.4).

Water solubility can be obtained via hydrogen bonding of the surface moieties to the water molecules or electrostatic repulsions between neighboring SiNCs that possess significant surface charge. Zeta potential measurements indicate that the water solubility of the silica-encapsulated SiNCs is attributed to the latter mechanism (155). The Si-O bonds formed on the NC surface during microplasma treatment are highly electronegative, which results in an increase in (negative) surface charge. Figure 6.5 shows an increase in the zeta potential amplitude with microplasma treatment time. The large zeta potential allows the colloid to remain stable and dispersed in water.

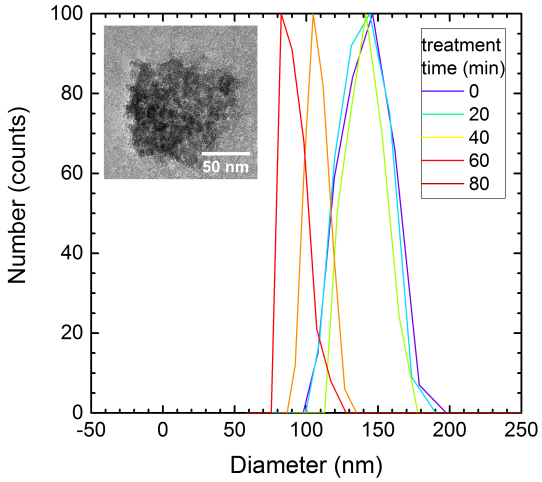

Figure 6.4: Agglomerate sizes of microplasma-treated SiNCs in water as a function of microplasma treatment time. Inset shows a TEM image of a single agglomerate (image courtesy of Shreyashi Ganguly). Measurements were acquired within a day of dispersion in water.

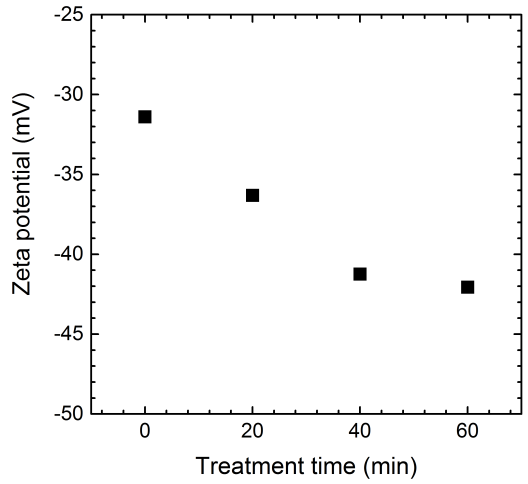

Figure 6.5: Zeta potential of microplasma-treated SiNCs in water as a function of treatment time. Measurements were acquired within a day of dispersion in water.

In addition to water solubility, the microplasma-treated SiNCs also exhibited enhanced photoluminescence (Figure 6.6a). As previously mentioned, the photon emission of as-produced, nonthermal plasma-synthesized SiNCs is suppressed by nonradiative surface defects. Oxygen can act as a passivating source for silicon surfaces; oxidized hydrogen-terminated SiNCs have shown over five-folds improvement in PLQY(43; 108). However, in the ambient environment, oxidation is a slow process; despite the reactive SiNC surface, it may take over 2 – 3 months for the growth of a complete native oxide shell (43; 108).

Microplasma treatment (in water) significantly enhanced the oxidation rate of silicon surfaces. PLQYs nearing 50 % were measured from the SiNCs within 40 min of treatment (Figure 6.6). In comparison, SiNCs oxidized in ambient conditions only attained PLQYs nearing 30 % after 2 months (43). Figure 6.3c shows a picture of the intense red emission from the microplasma-treated SiNCs irradiated with UV light. As shown in Figure 6.6b, the emission color is tunable by changing the size of the as-produced SiNCs.

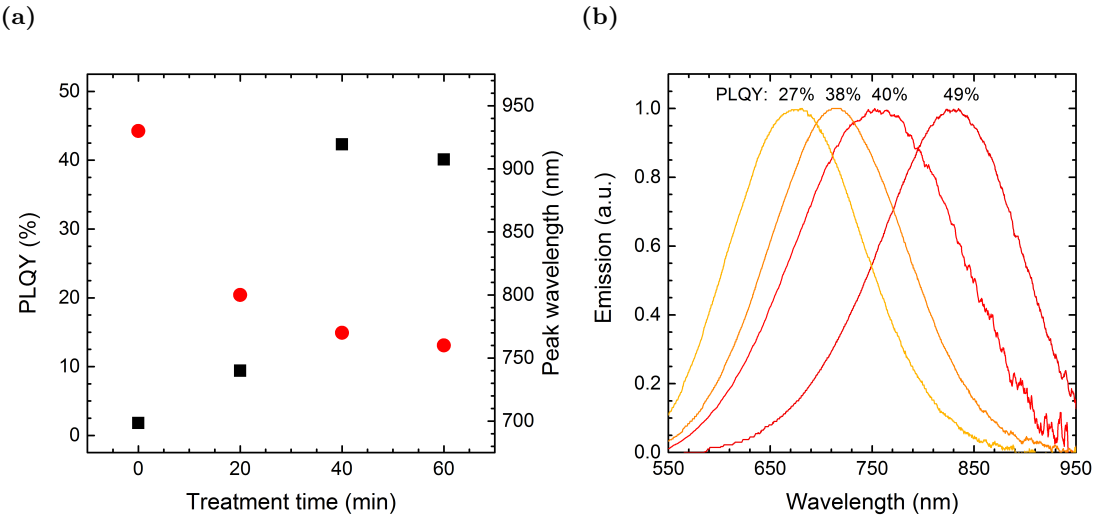

Figure 6.6: (a) PLQY (black squares) and peak emission wavelength (red circles) of SiNCs with microplasma treatment. (b) Size-tunable emission from microplasma-treated, nonthermal plasma-synthesized SiNCs.

The SiNCs displayed a significant shift in photoluminescence wavelength with the microplasma treatment (Figure 6.6a). The blueshift in emission, likely the result of a decreasing NC core size, suggests the plasma-induced reaction oxidized into the core of the SiNCs. This trend is dissimilar to reports by Mariotti *et al.* with SiNCs treated in ethanol and water using a DC plasma (112). From their FT-IR spectrum, it is deduced that the SiNCs were oxidized in air prior to microplasma treatment. This suggests the initial surface chemistry of the SiNCs may play a role in the plasma-induced reactions.

The SiNCs remained stable in water several months proceeding the microplasma treatment. Figure 6.7 shows the PLQY and peak photoluminescence wavelength of the treated SiNCs during the first 15 days. No degradation or changes in emission properties were detected. The long-term stability of the SiNCs is beneficial for prolonged monitoring of the activities of and interactions between biomolecules—a study that is difficult to accomplish with conventional organic dyes (40).

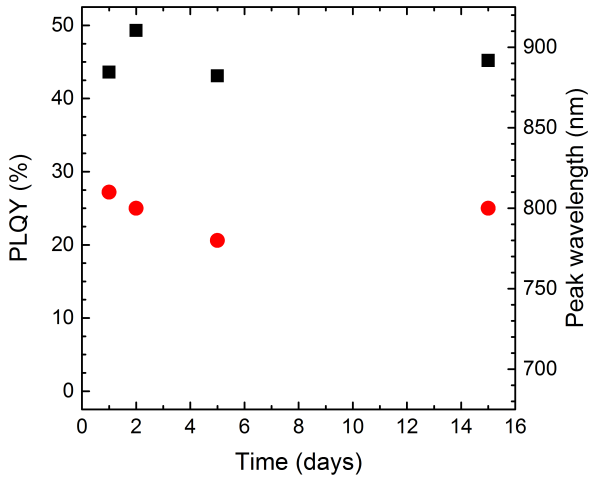

Figure 6.7: Stability of SiNCs in water after microplasma treatment as represented by their PLQY (black squares) and peak emission wavelength (red circles).

6.2.1 Microplasma surface passivation mechanism(s)

The microplasma-induced reactions between the SiNCs and water have not been extensively studied. Mariotti *et al.* postulated the microplasma reactions were driven by

hydroxyl (OH) radicals generated by electron-induced dissociation of water molecules at the plasma-liquid interface or in the liquid (112). They proposed a protective oxide shell was formed on the NC surface from the the condensation of the chemically-reacted OH species; they thus believe the microplasma treatment is purely a surface oxidation reaction.

The blueshift in emission wavelength observed with microplasma treatment time (Figure 6.6a) indicates reduction of the NC's core, which suggests that the microplasma reaction here was not simply a surface reaction as proposed by Mariotti *et al.* According to X-ray diffraction (XRD) measurements, the 5.9-nm nonthermal plasma-produced SiNCs reduced to $\sim$ 3 nm after treatment, which indicates $\sim$ 1.45 nm shell was grown around the SiNCs. No further changes in emission wavelength was observed after microplasma treatment, which suggests the oxide shell was able to act as a protective layer to inhibit the diffusion of water molecules into the NC core.

The effectiveness of an oxide shell as a diffusion barrier depends on the thickness and the quality of the oxide (156). In air, a 2 nm native oxide shell acts as an effective diffusion barrier for oxygen and water vapor (108). In water, the diffusion coefficient and solubility concentration of silicon oxide is higher than that of oxygen (157; 158). Thus, it is unlikely that the monolayer of oxide proposed by Mariotti *et al.* can provide an effective barrier against water diffusion (112).

Long-lived gaseous ions and/or radicals generated by the plasma played a small role in the microplasma reactions. Dissimilar from the direct microplasma treatment of SiNCs in water, dispersion of NCs into microplasma-treated water resulted in no noticeable difference in water-solubility. Furthermore, no significant improvement in photoluminescence or stability was observed when the plasma plume was not in contact with the solution (Figure 6.8). However, increasing the density of reactive hydroxyl (OH) and hydrogen peroxide (H_2O_2) or the density of oxygen species (O, O_2, O_3) with the addition of water vapor in argon or oxygen, respectively (159; 160; 161), enhanced the photoluminescence of the SiNCs (Figure 6.8). Interestingly, similar PLQY improvements were obtained despite the different mixture of oxidizing species produced with the addition of O_2 and H_2O (162).

In the liquid-phase, the interaction of electrons (from the plasma) and water creates

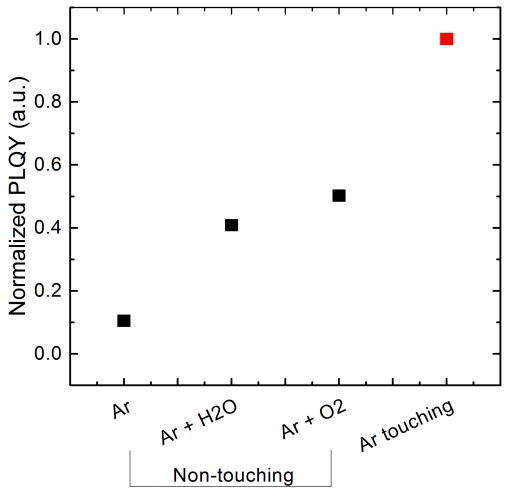

Figure 6.8: PLQY of SiNCs treated with argon, argon + water, and argon + oxygen plasma with plume away from the solution, and with argon plasma with plume in contact with the liquid.

reactive oxygen and hydroxyl species that may all play a role in the SiNC's surface passivation (163; 164; 165). The majority of the reactions likely occur at the liquid/plasma interface as microplasma treatment of non-wetted SiNCs floating on the water surface delivered similar results to the dispersed SiNCs. Some reactions may occur in the liquid as mixing induced by the gas flow would also force reactive species into the liquid (166). In addition, the mixing also recirculates the NCs at the plasma liquid interface.

Studies using Fenton's reaction showed the importance of liquid-phase radicals and/or ions in the surface reactions. The oxidation of iron(II) with hydrogen peroxide (H_2O_2) can generate highly reactive OH radicals (OH·) in the bulk of the solution:

$$Fe^{2+} + H_2O_2 \longrightarrow Fe^{3+} + OH\cdot + OH^- \tag{6.1}$$

Figure 6.9 shows the optical properties of as-produced, hydrogen-terminated SiNCs reacted with 4 different molar concentrations of $Fe^{2+}$and H_2O_2: 1. 100 μM, 2. 1,000 μM, 3. 10,000 μM, and 4. 100,000 μM. Enhanced photoluminescence, approaching the QYs measured for microplasma-treated SiNCs, was observed with higher concentrations

(1,000 and 10,000 μM) of Fenton's reagents. Further increasing the concentration increases the pH of the solution, which results in the precipitation of Fe as $Fe(OH)_3$ and the decomposition of H_2O_2 to oxygen (167). The resulting SiNCs exhibited inferior photoluminescence to the microplasma-treated NCs.

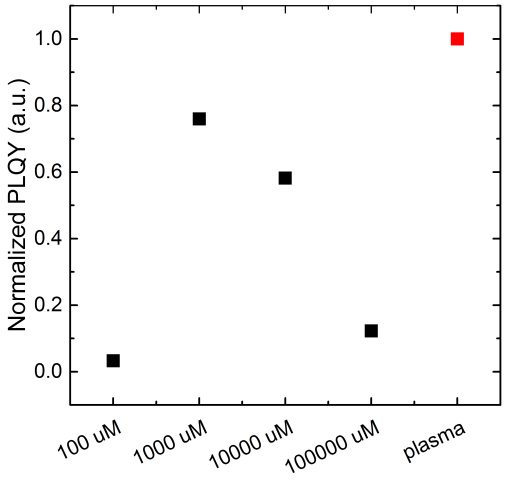

Figure 6.9: PLQY of SiNCs after Fenton's reaction as a function of molar concentration of hydrogen peroxide and iron(II) sulfate. PL measurements were performed 1 day after dispersion.

The gas and liquid-phase studies conducted indicate the importance of oxidizing species in the formation of a stable, oxide shell. It should be noted that the microplasma reaction is a complex process and probably includes reactions with O, O_3, OH, H_2O_2, and HO_2 species amongst others. Two different reactions can occur with the silanol groups on the surface:

1. dissolution of silica to form silicic acid (H_4SiO_4)
2. condensation of silanol groups to form siloxane links (Si-O-Si)

The reaction of amorphous silica with water can lead to the dissolution of silica into silicic acid (H_4SiO_4) via the pathway shown in Reaction 6.2 (168). At moderate pH levels (pH 3 – 7.5), the formation of silicic acid progresses via the reaction of water with

silanol groups (≡Si−OH) (169).

$$\mathrm{Si{-}O_2(s) + 2\,H_2O \longrightarrow H_4SiO_4(aq)} \tag{6.2}$$

A high density of silanol groups can lead to condensation reactions, producing siloxane links (Si-O-Si) on the surface (170):

$$\mathrm{Si{-}OH + Si{-}OH \longrightarrow Si{-}O{-}Si + H_2O} \tag{6.3}$$

While the condensation reaction (Reaction 6.3) leads to the formation of a stable oxide shell, the dissolution of the silica shell (Reaction 6.2) exposes the core to further oxidation and allows the diffusion of water molecules into the NC's core. It is likely that both reactions play a role in the microplasma reactions.

6.3 Conclusions

Water-soluble silicon nanocrystals were fabricated by treating nonthermal plasma-synthesized NCs in water using a microplasma processing technique. The microplasma-treated SiNCs demonstrated several characteristics that are highly attractive in the imaging of biomolecules. For the first time, efficient size-tunable luminescence, with PLQYs exceeding 50 %, was observed from water-soluble SiNCs. Furthermore, the microplasma-treated SiNCs were high in purity—only silicon, oxygen, carbon, and hydrogen species were detected; thus, no post-synthesis purification is needed prior to biological application. Finally, the NCs possess enhanced stability in water, which is beneficial in long-term studies of biomolecules; no degradation in PLQY was observed within the first 20 days of water dispersion.

The stability of the microplasma-treated SiNCs is likely the result of the formation of a stable oxide shell ($>$ 1.4 nm thick according to XRD). The oxide shell acts as an effective barrier against water diffusion and prevents further oxidation of the NC core. Fenton's reaction indicates that the OH species generated in the liquid-phase could play a significant role in the surface passivation reaction. However, gas-phase reactions with argon + oxygen plasma indicate that other reactive oxygen species may also play an important role in the microplasma reactions.

6.4 Experimental

6.4.1 Synthesis

Silicon nanocrystals were synthesized using a nonthermal plasma. 14 sccm of 5 % SiH_4/He mixture and 10 sccm of Ar were flown into a 13.56 MHz RF-powered plasma maintained at 1.6 Torr. 60 W nominal power was used to crystallize the silicon. Hydrogen gas was injected into the expansion region of the reactor to hydrogen passivate the surface. The SiNCs were collected via inertial impaction onto glass slides for further processing.

Surface treatment. The hydrogen-terminated SiNCs were wetted in ethanol and dispersed in distilled water at a concentration of 0.5 mg/ml. An atmospheric pressure, nonthermal microplasma driven by 13.41 MHz RF source (154) was used to treat the SiNCs in water. 0.75 slm of Ar gas was fed into the reactor. The tip of the microplasma gun was placed 3 mm above the surface of the water, such that the 2.5 W microplasma plume touched the liquid surface. The SiNCs were treated for 45 min to 1 h, and the volume of water was adjusted every 15 mins to counter evaporation.

6.4.2 Mechanism characterization

Fenton's reaction. Silicon nanocrystals were wetted with ethanol and dispersed into 3 ml mixtures of hydrogen peroxide (H_2O_2) and iron(II) sulfate ($FeSO_4$) in water. The molar concentrations of H_2O_2 and $FeSO_4$ were varied from 100 μM to 100,000 μM.

Plasma species. Silicon nanocrystals were wetted in ethanol and dispersed into 3 ml of distilled water. For the microplasma treatment, the tip of the plasma plume was positioned 3 mm above the surface of the liquid, and the SiNCs were treated for 1 h. The total flowrate of gas mixtures were kept at 0.75 slpm for the following conditions:

Ar + O_2: 1 % oxygen gas was added to the argon plasma at flowrates of 0.74 slm of argon and 8 sccm of oxygen.

Ar + H_2O: Water vapor was bubbled into the plasma using 0.75 sccm of argon gas at a partial pressure of 2.5 %.

6.4.3 Characterization

Photoluminescence. Photoluminescence of the SiNCs was measured using an Ocean Optics USB2000 spectrometer and integrating sphere setup that was calibrated using an Ocean Optics LS-1-CAL tungsten halogen light source. SiNCs in colloidal form, dispersed in water at a concentration of 1.5 mg/ml, were irradiated with a 395-nm LED, and 60 scans were taken per sample. The fluorescence standard Rhodamine 101 inner salt was dispersed in ethanol and used as a reference for quantum yield measurements.

Transmission electron microscopy (TEM). The SiNCs were imaged using a FEI Technai T12 microscope equipped with an energy-dispersive X-ray spectroscopy system. SiNCs dispersed in water were drop cast onto a lacey carbon TEM grid and placed under vacuum for 1 h to ensure solvent evaporation prior to imaging.

X-ray diffraction (XRD) spectroscopy. XRD was performed using a Bruker D8 Discover 2D with a Co Kα radiation source. The as-produced SiNCs were dispersed in toluene and the microplasma-treated SiNCs were dispersed in water and drop cast onto borosilicate glass substrates. The substrate was heated at 100 ^{o}C in nitrogen atmosphere for 30 min to evaporate the solvents. Two frames of 30 ^{o} width were collected with the first frame centered at 30 ^{o}. Each frame was scanned for 300 s. Debye-Scherrer fits of the integrated XRD patterns were used to determine the NC sizes.

Chapter 7

Silicon nanocrystal films as antireflective coatings

Antireflective coatings (ARCs) can drastically improve the efficiency of photovoltaic devices by increasing the coupling efficiency of sunlight into the cell . Reflection losses can be reduced by texturing the cell surface or using transparent oxides. Zhao *et al.* reported over 6 % increase in cell efficiency with the application of a "honeycomb" surface texture (171; 172).

In 1990s, Strehlke *et al.* showed that ARCs can be fabricated using electrochemically-etched porous silicon (p-Si) (173; 174). By varying the thickness and porosity of the p-Si, its refractive index can be tuned such that destructive interferences are created between waves reflected at the air/ARC and ARC/substrate interfaces. In this study, we demonstrate that the same principle can be applied to silicon nanocrystal (SiNC) films.

7.1 Results and discussion

Antireflective coatings make use of impedance mismatch between materials of differing refractive indices. Phase changes that arise at the material interfaces create destructive interferences between light waves, minimizing reflection. A single reflection minimum can be created using a simple quarter-wave ARC (Figure 7.1a), where the thickness, d_{arc},

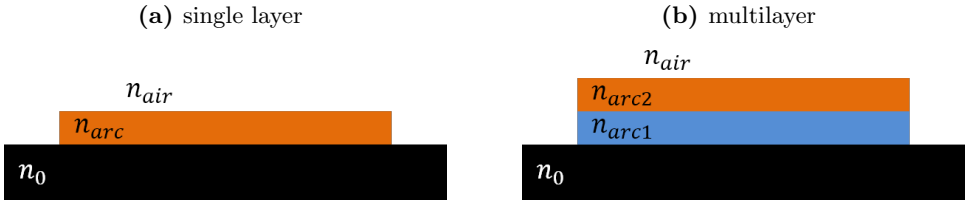

Figure 7.1: Schematic of antireflective coatings.

is chosen to be a quarter wavelength of the optical thickness of the ARC (173; 174):

$$n_{arc}d_{arc} = \frac{\lambda_{min}}{4} \tag{7.1}$$

where λ_{min} is the wavelength of minimum reflection and n_{arc} is the refractive index of the ARC.

The refractive index of the ARC is determined by Fresnel equations. The reflection, R, of a substrate of refractive index, n_0, with a single layer ARC is defined by the following equation (175):

$$R = \left(\frac{n_{arc}^2 - n_0 n_{air}}{n_{arc}^2 + n_0 n_{air}}\right)^2 \tag{7.2}$$

where $n_{air} = 1$.

Thus, to obtain zero minimum reflection, the equation simplifies to:

$$n_{arc}^2 = n_0 \tag{7.3}$$

The refractive index of a SiNC film can be tailored by tuning the density of the film (176). For a film with a mixture of SiNC and void (air), the Lorentz-Lorenz equation states that the effective refractive index, n_{eff}, is a function of the film density, f_{si}, and refractive index of silicon, n_{si}.

$$\frac{n_{eff}^2 - 1}{n_{eff}^2 + 2} = f_{si}\left(\frac{n_{si}^2 - 1}{n_{si}^2 + 2}\right) \tag{7.4}$$

A single-layer SiNC film is an ineffective ARC as it only maintains a single reflection minimum. However, multiple layers of ARCs with differing refractive indices can be

stacked to improve the anti-reflection properties (Figure 7.1b). The reflection of a double layer ARC is as follows (175):

$$R = \left(\frac{n_{arc2}^2 n_0 - n_{arc1}^2 n_{air}}{n_{arc2}^2 n_0 + n_{arc1}^2 n_{air}} \right)^2 \tag{7.5}$$

Zero reflection is obtained when:

$$n_{arc2}^2 = \frac{n_{arc1}}{n_0} \tag{7.6}$$

From these equations, it is determined that ~ 60 % density is needed for a single layer of SiNC ARC on a bare silicon substrate. However, as most solar cells are fabricated with a thin layer of transparent conductive oxide, a SiNC film acting as a second layer of ARC on an indium-tin oxide (ITO) coated silicon wafer requires a lower density of 31 %.

Solution-processed silicon quantum dot antireflective coatings

Nonthermal plasma-synthesized SiNCs were functionalized with dodecyl ligands via thermal hydrosilylation reaction to allow dispersion of the SiNCs into non-polar solvents. The resulting NC inks are suitable for liquid-phase deposition processes such as drop casting, spin coating, and spray coating (Figure 7.2).

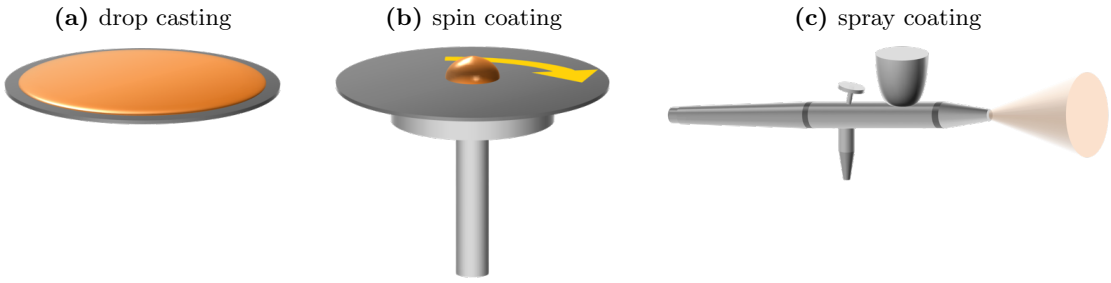

Figure 7.2: Liquid-phase deposition techniques.

Drop casting (Figure 7.2a) allows a drop of NC ink to dry under controlled conditions (pressure and temperature) over a period of time. Unfortunately, differences in evaporation rates across the substrates results in uneven film thicknesses.

Spin coating is able to create more uniform films using centrifugal forces to spread the ink evenly across the substrate (Figure 7.2b). A scanning electron microscope (SEM) image of a spin-coated NC film on a polished silicon wafer is seen in Figure 7.3. Dense, uniform SiNC films can be deposited through spin-coating.

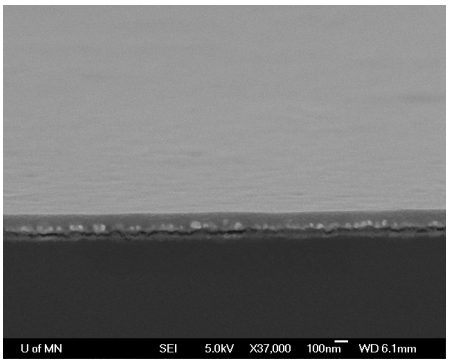

Figure 7.3: SEM image of spin-coated SiNC film on a polished silicon substrate.

The properties of spin-coated SiNC films can be tuned by adjusting the concentration of the colloid or the rotational speed of the substrate. As seen in Figure 7.4, the thickness of the NC films is dependent on the concentration of the colloid. Thin films 40 nm – 140 nm in thickness were created by simply varying the colloid concentration from 0.5 mg/ml to 50 mg/ml, while maintaining a spin speed of 1500 rpm. However, saturation of the film thickness was observed between 20 mg/ml and 50 mg/ml.

Unfortunately, spin coating is limited to smaller substrates with polished surfaces. Any defects on the substrate will have a negative impact on the uniformity of the spin-coated film. As a partially aerosol technique, spray coating (Figure 7.2c) allows deposition on a wide range of substrates. It makes use of atomizers to aerosolize an ink, generating droplets of NCs that deposit on a movable platform. Atomizer pressure, liquid flow rate, colloid concentration, and substrate distance are parameters that can be tuned to adjust film properties. Figure 7.5b shows an SEM image of SiNCs spray coated onto a textured silicon substrate using an airbrush gun. Dense NC films (~ 50 %) can be deposited uniformly on pyramidal structures—a feat which cannot be achieved via spin coating.

Silicon nanocrystal ARCs were successfully fabricated by spin coating NCs dispersed in chloroform onto polished silicon wafers. The film thicknesses were tuned by changing

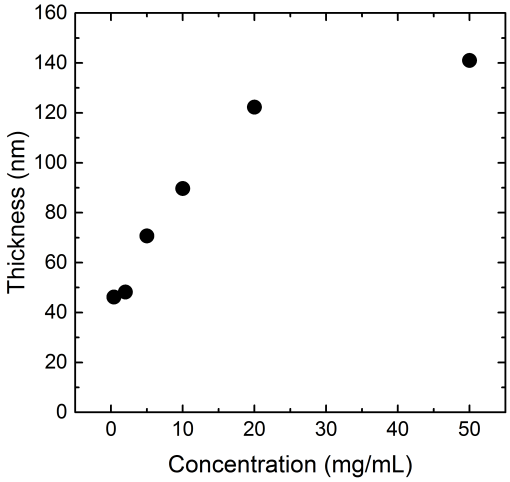

Figure 7.4: Effects of SiNC colloid concentration on spin-cast film thicknesses.

(a) blank **(b)** spray-coated layer

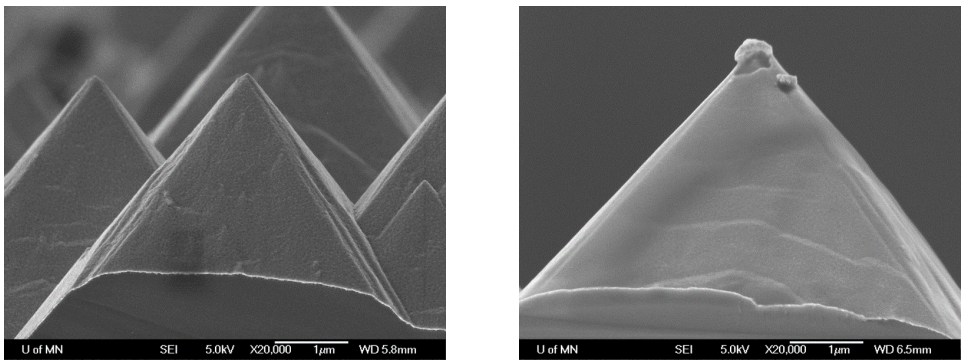

Figure 7.5: SEM images of (a) blank textured substrate and (b) spray-coated SiNC film on a textured substrate.

the colloid concentrations. As seen in Figure 7.6, the silicon wafer is highly reflective, reflecting close to 40 % of incident light. The addition of thin films of SiNCs significantly reduces the reflection of the wafers. As predicted by the model, the wavelengths of minimum reflection is dependent on the thicknesses of the ARCs.

Figure 7.7 compares the minimum reflection wavelengths measured to the wavelengths determined via Fresnel's equations. The diagonal line represents an exact match

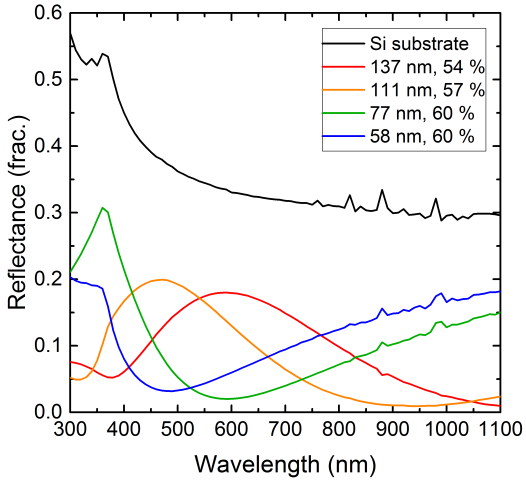

Figure 7.6: Antireflective SiNC films of different thicknesses (and similar densities) on silicon substrate.

of the measured to theoretical values. A close correlation between the two data sets was found, with R-squared values above 0.99 calculated.

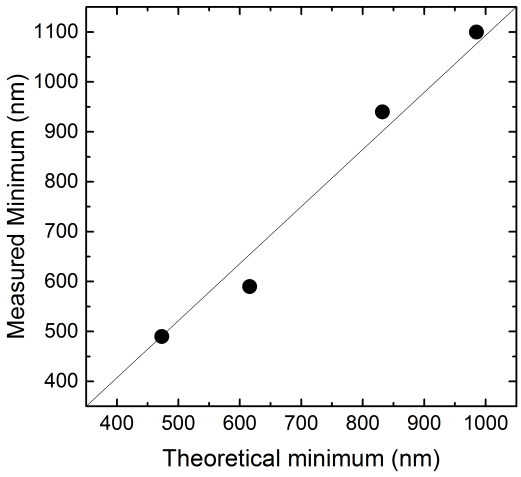

Figure 7.7: Comparison of the minimum reflection wavelengths measured and the wavelengths determined via Fresnel's equations.

7.2 Conclusion

Effective antireflective coatings for silicon substrates were fabricated using silicon nanocrystals. Fresnel equation dictates that a refractive index of ~ 2 is needed for an ARC on a silicon substrate. For bulk silicon, the refractive index at a specific wavelength is fixed; however, the refractive index of a SiNC film can be tuned by simply varying the density of the silicon constituents. The relationship between the film density and refractive index can be effectively modeled using effective medium approximations (EMA) (see Appendix A).

According to the Lorentz-Lorenz EMA, ~ 60 % dense SiNC films—close to the limit for randomly-packed spheres—are needed for the films to act as effective ARCs. Spin casting is a highly advantageous technique to deposit thin and dense films from SiNC inks. We demonstrated that these dense SiNC films can act as effective ARCs, and by varying the thicknesses of the films, the wavelengths of minimum reflectance can be tuned.

7.3 Experimental

7.3.1 Synthesis and deposition

Liquid-phase deposited hydrosilylated silicon nanocrystals. Hydrogen-terminated SiNCs were synthesized in a nonthermal plasma sustained by a 45 W (nominal) 13.56 MHz radio-frequency power supply. 35 sccm of argon carrier gas and 14 sccm of silane precursor gas were injected reactor maintained at 1.4 Torr using an actuated butterfly valve. 100 sccm of hydrogen gas was introduced into the diffused region of the plasma to passivate the SiNC surface. SiNCs were collected via diffusion on a stainless steel mesh downstream of the plasma.

The collected SiNCs were sonicated into a 18 ml mixture of 1 part 1-dodecene to 5 parts mesitylene for hydrosilylation. The solution was transferred into a round bottom boiling flask in a sand bath maintained at 215 ^{o}C. A cooling water condenser prevents solvent evaporation. After 3 h reaction, the SiNCs were dried at room temperature and re-dispersed in chloroform for liquid-phase processing. All processes were performed in nitrogen atmosphere.

7.3.2 Characterization

Film thicknesss and density. The thickness and density of the SiNC films were determined via ellipsometry (see Appendix A). Measurements were taken at 65^o and 75^o from 800 nm to 1100 nm. The collected polarization change is fitted using Bruggeman effective medium approximation to obtain the thickness and density.

Reflection. Substrate reflection was measured using ellipsometry from 300 nm to 1100 nm at 15 ^{o} incidence angle.

Chapter 8

Dual-purpose, luminescent downshifting and antireflective silicon quantum dot film

8.1 Introduction

In order for PV technologies to be competitive in the power generation market, they must overcome the Shockley-Queisser theoretical limit of 30 % that was estimated for conventional, single bandgap cells under AM1.5G sun (177; 178). Several methods have been devised so that solar cells can exceed their theoretical limiting efficiency. One of which is through spectrum modification, which seeks to minimize PV losses due to the poor spectral response of solar cells (179). Surface recombination losses can be reduced with the addition of a luminescent downshifting (LDS) layer to the front surface of a solar cell. The LDS layer absorbs the incident high-energy photons and emits them at longer wavelengths.

A material must possess several properties to be an effective luminescent downshifter (179; 180):

1. The excitation energy of the LDS layer must be between 300 to 500 nm.
2. The material must have low absorption in the regions of the spectrum not downshifted.

3. Low excitation energy is required as solar power is on the order of W/cm^2.
4. The LDS layer must emit within the solar cell's absorbance range, which is typically between 350 and 1100 nm.
5. High photoluminescence quantum yield (PLQY), defined as the fraction of photons emitted to photons absorbed, is necessary.

Silicon quantum dots (SiQDs) are attractive materials for LDS. The material possesses a large intrinsic Stokes shift due to its indirect band gap; high-energy photons below 600 nm are effectively absorbed by the silicon nanocrystals (SiNCs) and re-emitted at a lower energy (Figure 8.1). Conversion efficiencies, or PLQYs, exceeding 60 % were discovered from dodecyl-passivated, nonthermal plasma-synthesized SiNCs (83).

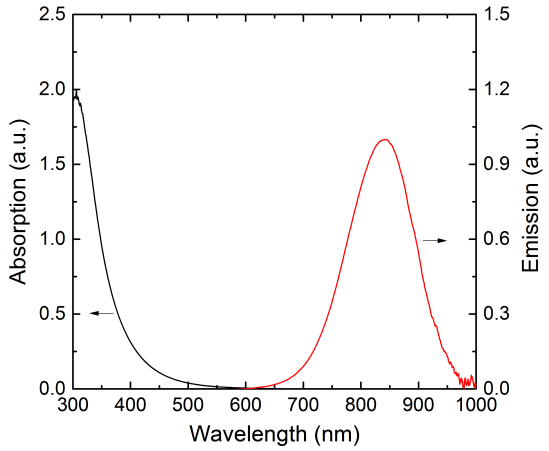

Figure 8.1: Absorption and emission spectra of 4.2 nm SiNCs.

Svrcek *et al.* successfully embedded SiNCs prepared *ex-situ* via the pulverizing of electrochemically-etched porous silicon (p-Si) into spin-on glass (SOG), a silicon dioxide (SiO_2) that is commonly used as a surface encapsulation layer for solar cells. The group saw a successful increase in internal quantum efficiency (IQE) of the solar cell at wavelengths between 350 and 450 nm, resulting in an increase in absolute efficiency by approximately 0.4 % (181; 114).

In this study, we applied highly-luminscent SiNCs as LDS layers onto heterojunction solar cells. Cells with liquid-phase deposited, dodecyl-passivated SiNCs demonstrated enhanced EQE in the blue/UV spectrum; however, reduced EQE was also observed

in the regions not downshifted as a result of increased reflection. As a solution, we fabricated a dual-purpose SiNC film that acted as an antireflective coating (ARC) in addition to a luminescent downshifter. The cells with the dual-purpose films exhibited enhanced EQE in the blue/UV spectrum without efficiency losses above 400 nm. On cells with deficient antireflective coatings, the effects of the SiNC ARC was significant; almost 20 % improvement in EQE was observed in the visible/NIR range.

8.2 Results and discussion

8.2.1 Silicon quantum dots as luminescent downshifters: preliminary results

Silicon nanocrystals $\sim$ 4.2 nm in size were synthesized in a low-pressure, nonthermal plasma and functionalized with 1-dodecene molecules in a thermal hydrosilylation reaction. The hydrosilylated SiNCs exhibited enhanced PLQYs nearing 60 %, and the NCs were soluble in non-polar solvents to form NC inks beneficial for solution processing. SiNCs dispersed in chloroform at a concentration of 20 mg/ml were drop cast onto a heterojunction solar cell from l'Ecole polytechnique federale de Lausanne (EPFL) as depicted in Figure 8.2.

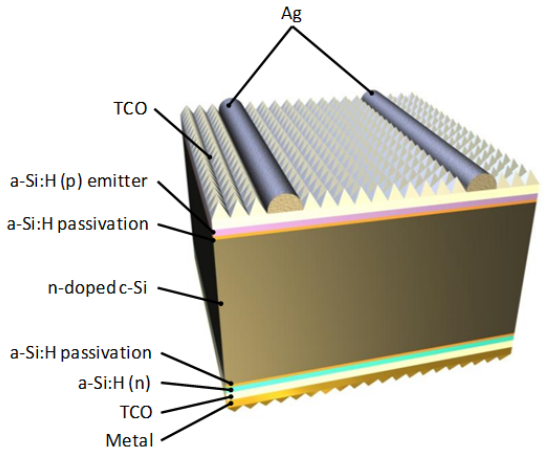

Figure 8.2: Depiction of heterojunction solar cell used. Image courtesy of Zachary Holman.

As seen in Figure 8.3, the SiNC LDS layer resulted in an increase in solar cell performance at wavelengths < 400 nm. However, the cell saw a decrease in external quantum efficiency (EQE) at all other wavelengths due to increased reflectivity of the cell. This can potentially negate the desired LDS effects.

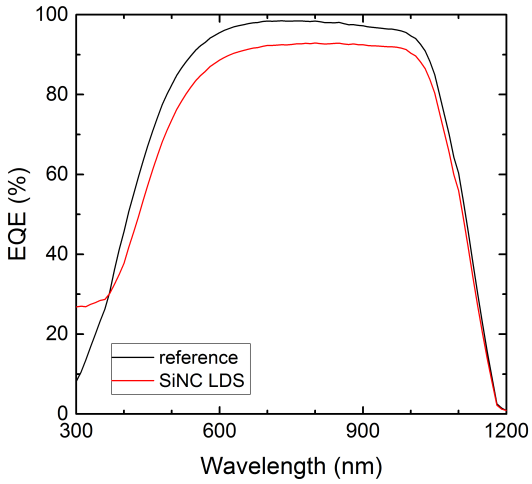

Figure 8.3: External quantum efficiency of solar cell with drop-cast SiNC luminescent downshifting layer.

The increased reflection from the SiNC LDS film can be remedied by employing a dual-purpose SiNC layer that acts as both a LDS and an ARC. A dual-purpose SiNC film is expected to increase solar cell performance by up to 15 % (relative to the reference cell) for NCs with 60 % photon conversion efficiency (182)—an efficiency achieved by Kortshagen *et al.* (83).

Antireflective SiNC films were fabricated in Chapter 7 via liquid-phase deposition of NC inks. However, the liquid-phase deposition of SiNCs proves to be impractical for the fabrication of multilayered ARCs. As the Lorentz-Lorenz equations demonstrate, the refractive indices of the SiNC films—a property that determines the performance of the ARC—is dependent on the film densities. As a second ARC layer on an ITO-coated silicon wafer, the SiNCs films need to be ~ 30 % dense, and the most porous film achieved via spin coating had a density of ~ 40 %.

While the thicknesses of liquid-phase deposited films are easily adjustable, tuning

the densities of the films is more challenging. As seen in Figure 8.4, less than 20 % variation in film density was measured with spin-coated films fabricated with colloid concentrations between 0.5 mg/ml and 20 mg/ml. It was believed that the use of longer ligands could increase the inter-particle spacing. However, extending the ligand length from twelve to eighteen carbons had little influence on the film density (Figure 8.4). This implies that the ligands do not extend away from, but wrap around the NC instead.

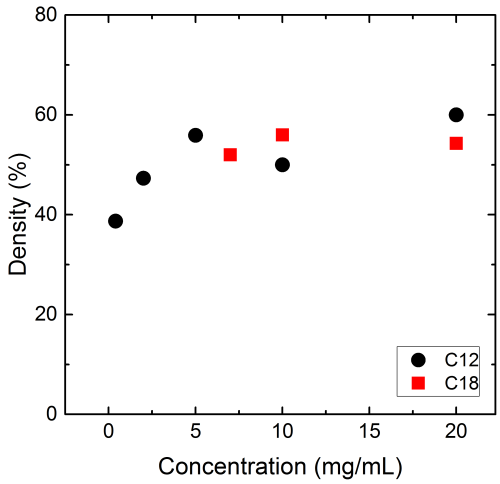

Figure 8.4: Effects of SiNC colloid concentration and ligand length on spin-cast film density.

Aerosol deposition of silicon quantum dot films

Aerosol deposition may be a more flexible method to deposit the more porous SiNC films. Holman *et al.* demonstrated the deposition of germanium nanocrystal (GeNC) thin films in a nonthermal plasma reactor via inertial impaction (8). Driven by a large pressure differential across a slit orifice, the gas flow is accelerated to supersonic speeds at the nozzle exit. The GeNCs entrained in the flow can attain velocities up to 450 m/s (theoretically) (8). The velocities (or momentum) of the NCs at substrate impaction determines the densities of the GeNC films. Densities between $\sim$ 10 % and 55 % were obtained by simply varying the pressure ratio across the orifice.

Holman *et al.*'s model in Reference 8 calculates the velocity of the GeNCs downstream of the orifice. Due to the low operating pressures and temperatures, it is possible to assume the gases are ideal. Initial SiNC velocities at the orifice are assigned the Mach (or sonic) speed of the gases, assuming the NCs have sufficient time in the orifice to reach equilibrium with the flow. The model then calculates the NCs' acceleration at a given time, taking into account the drag forces on the NCs. Following, the velocities and positions of the NCs are evaluated using simple kinematic equations.

Using MATLAB, the flow downstream of the orifice was modeled for SiNCs. Figure 8.5b shows the NC velocity as a function of its position from the orifice for a typical SiNC synthesis recipe (Table 8.5a). The NC velocity increases in the gas expansion region and reaches its maximum velocity of over 400 m/s at the position of the Mach disk, which is represented by the kink in the profile. Since the densities of the impacted films are dependent on the NC velocities, the film densities can simply be varied by adjusting the substrate position, i.e. the standoff distance, from the orifice.

(a) Typical SiNC synthesis recipe

Parameter	Value
SiNC size	4 nm
SiH_4 flowrate	14 sccm
Ar flowrate	50 sccm
Orifice size	0.635 × 25 mm
Upstream pressure	1.5 Torr
Downstream pressure	100 mTorr

(b) Modeled SiNC velocity

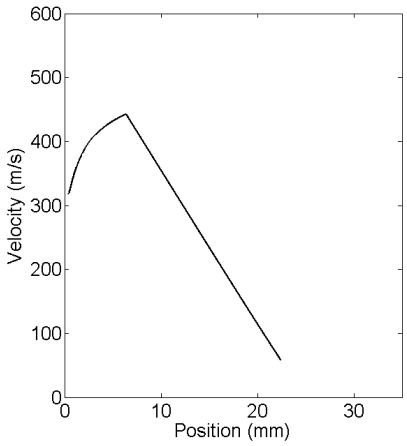

Figure 8.5: SiNC velocity as a function of position from the orifice for typical synthesis recipe with argon as carrier gas. Modeled using equations from (8).

Using the conditions listed in Table 8.5a, SiNCs were impacted onto 2 × 2 cm polished silicon wafers placed at various standoff distances from the orifice. The densities of the impacted films (Figure 8.6), measured via ellipsometry (see Appendix A), follows

a similar trend to the modeled data in Figure 8.5b. However, the maximum density obtained was only $\sim$ 10 %, implying inadequate SiNC momentum at impaction.

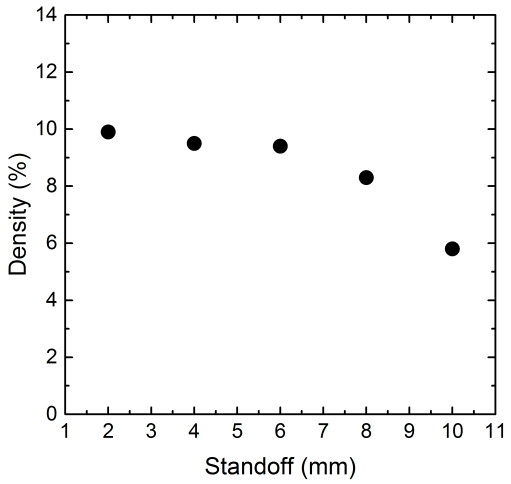

Figure 8.6: Measured SiNC film densities as a function of standoff distance.

The inertial impaction of SiNCs is challenging. While it is possible to obtain 55 % dense GeNC films, the low density of silicon necessitates $\sim$ 2.3 times the velocity to attain the same momentum. The velocity of the SiNCs can be increased by changing the composition of gases injected into the reactor. The gas speed in the throat of the nozzle is limited by their speed of sound. The speed of sound in argon is 319 m/s; however, in gases such as helium and hydrogen, the speed of sound is over 1000 m/s. According to the model, adding 100 sccm of hydrogen gas can increase the NC velocity by over 100 m/s. As seen in Figure 8.7, the addition of hydrogen gas increased the film density by three-folds—over 30 % dense SiNC films were obtained. Films with densities between 10 % and 35 % were produced by simply varying the standoff distance. Unfortunately, the increase in NC velocity with the addition of 100 sccm of hydrogen is insufficient for the SiNCs to attain the same momentum as GeNCs. To obtain densities close to the packing limit, it is necessary to replace the carrier gas used, which may change the optical properties of the SiNCs.

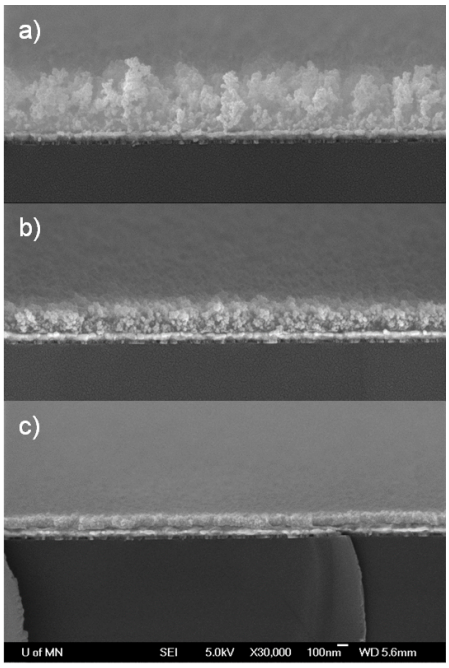

Figure 8.7: SEM image of impacted SiNC films (a) 10 %, (b) 25 %, and (c) 35 % dense.

8.2.2 Dual-purpose, luminescent downshifting and antireflective silicon quantum dot film

Oxidized fluorine-passivated SiNCs, with their high PLQY (Figure 2.12) and enhanced stability in ambient conditions and under UV irradiation (84; 89), are ideal materials for photovoltaic applications.

Fluorine-passivated SiNCs were synthesized in the two-stage NC synthesis and gas-phase functionalization nonthermal plasma reactor depicted in Figure 2.11. Sulfur hexafluoride (SF_6) was injected into the second surface treatment plasma to passivate the NC surface. The SiNCs were impacted directly onto heterojunction solar cells with poor EQE in the blue/UV region (Figure 8.2).

The density and thickness of the films were tuned for antireflective properties. As previously calculated, as a second ARC on ITO-coated silicon substrates, ~ 30 % dense SiNC films are needed. Unfortunately, due to limitations in the impaction process, a maximum film density of 20 % was obtained. The thicknesses of the films were varied between 100 nm and 250 nm to change the wavelengths of minimum reflectance. SEM

images of one of the impacted films are shown in Figure 8.8. The SiNCs were deposited uniformly across the cell, despite the textured surface.

(a) top down **(b)** cross section

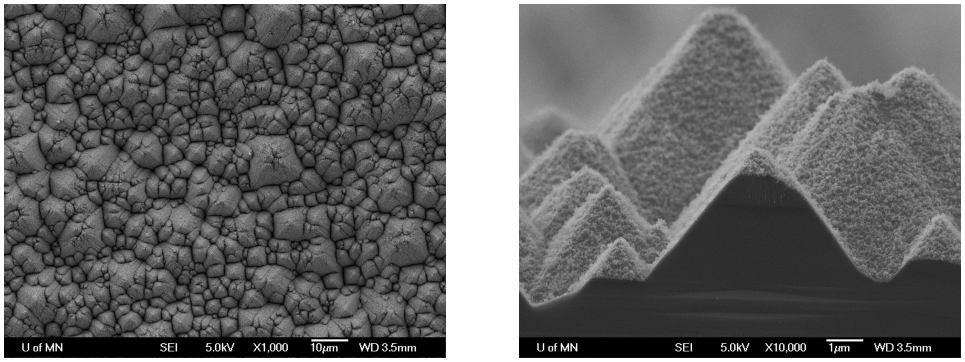

Figure 8.8: SEM images of SiNC film on a solar cell.

The impacted SiNC films acted as successful ARCs. The solar cells demonstrated little to no reduction in EQE in the visible range (Figure 8.9a). Slight decrease in efficiencies at the higher wavelengths was observed with the thickest SiNC film; at $\sim$ 250 nm the film's wavelength of minimum reflectance is located in the IR region. The antireflective SiNC films demonstrated significant improvements over the LDS films that were not tuned for antireflective properties; in comparison, the drop-cast films from the preliminary tests led to $\sim$ 10 % decrease in EQE in the regions not downshifted (Figure 8.3).

On solar cells with deficient ARCs, the antireflective properties of the SiNC films were more apparent. Figure 8.9b shows almost 20 % enhancement in EQE when SiNCs were deposited on silicon solar cells with poor ARCs. Thus, even with a lack of LDS, the application of SiNCs on photovoltaic devices can be highly beneficial.

As luminescent downshifters, the fluorine-passivated SiNCs also led to improvements in EQE in the blue/UV region of the solar spectrum (Figure 8.9a). The SiNCs obtained $\sim$ 40 % PLQY after 2 weeks of oxidation; at this point, 15 % increase in EQE was observed at 300 nm.

The results showed a low coupling efficiency between the NCs' photoluminescence and the LDS effect. As the photoluminescence of a NC is multidirectional, some of the

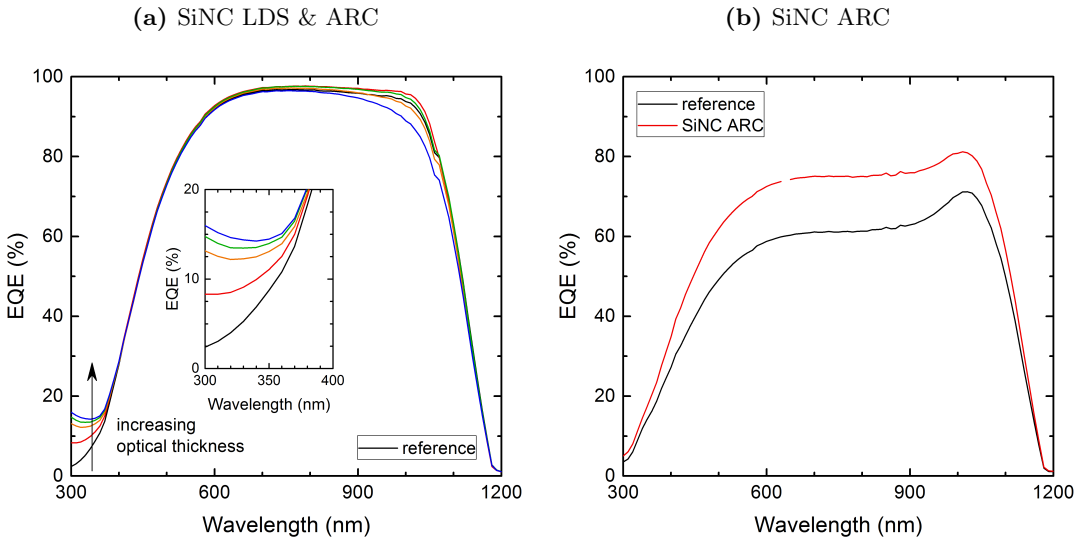

Figure 8.9: (a) EQE of solar cells with dual-purpose, luminescent downshifting and antireflective SiNC films of different thicknesses. Cells were measured 2 weeks after SiNC deposition. (b) EQE of a solar cell with poor ARC (black) and with a layer of SiNC ARC (red).

photons emitted may escape the system through the LDS/air interface. Embedding the SiNCs in a transparent matrix, such as SOG or poly(methyl methacrylate) (PMMA), can promote total internal reflection of photons traveling at low angles towards the LDS/air interface and increase the probability of the photons penetrating into the solar cell (183).

The improving EQE with increasing film thickness (Figure 8.9a) also implies inadequate absorption of the high-energy light by the LDS films. This is likely a result of the film surface roughness. The SEM images in Figure 8.8b suggest agglomerated SiNCs were impacted onto the cell instead of single SiNCs; thus, the high-energy UV light may be inadequately absorbed in the thinner portions of the film and be transmitted to the solar cell. Thus, in order to increase the LDS effects, the plasma process must be improved. The use of a single plasma for NC synthesis and surface passivation (Figure 1.2) can reduce agglomeration and improve the film properties.

8.3 Conclusions

We demonstrated the potential of luminescent silicon nanocrystal films in improving photovoltaic efficiencies. Heterojunction solar cells with liquid-phase deposited, dodecyl-passivated SiNCs displayed enhanced EQE in the blue/UV spectrum; however, an increase in surface reflectivity resulted in significant reduction in EQE at wavelengths above 400 nm. As a solution, we fabricated a dual-purpose SiNC film that acted as an ARC in addition to a luminescent downshifter. The dual-purpose films enhanced the EQE of the solar cells in the blue/UV spectrum without efficiency losses in the regions not downshifted. The effects of the SiNC ARC was most significant on cells that possessed a deficient ARC; almost 20 % improvement in EQE was observed.

8.4 Experimental

8.4.1 Synthesis and deposition

Fluorine-terminated SiNCs were synthesized in a two-stage NC synthesis and surface treatment nonthermal plasma reactor. The synthesis plasma was excited by a 70 W (nominal) 13.56 MHz radio-frequency (RF) power supply. 50 sccm of argon carrier gas and 6 sccm of silane precursor gas were injected into the synthesis plasma maintained at 3 Torr using a 4 mm circular orifice. 6 sccm of sulfur hexafluoride gas was introduced into the second, surface treatment plasma maintained at 1.5 Torr to passivate the SiNC surface. A 40 W (nominal) 13.56 MHz RF power source was used to excite the surface treatment plasma. SiNCs were collected via inertial impaction downstream of a 0.508 $\times$ 25 mm slit orifice where the pressure was maintained at 50 mTorr using a turbomolecular pump to achieve the required pressure differential across the orifice.

8.4.2 Characterization

Photoluminescence. Photoluminescence of the SiNCs was measured using an Ocean Optics USB2000 spectrometer coupled to an integrating sphere. The absolute irradiance of the setup was calibrated using an Ocean Optics LS-1-CAL tungsten halogen light source. Quantum yield measurements were verified using the fluorescence standard Rhodamine 101 inner salt dispersed in ethanol. Hydrosilylated SiNCs were dispersed in

toluene at a concentration of 1 mg/ml, and fluorine-passivated SiNCs were dispersed in dicholorobenzene at a concentration of 2 mg/ml. The SiNC solutions were irradiated with a 395-nm LED, and their absolute irradiance was measured.

Film thicknesss and density. The thickness and density of the SiNC films were determined via ellipsometry (see Appendix A). Measurements were taken at 65^o and 75^o from 800 nm to 1100 nm. The collected polarization change is fitted using Bruggeman effective medium approximation to obtain the thickness and density.

Chapter 9

Summary

Luminescent silicon quantum dots (SiQDs) are attractive in a variety of applications from light emitting devices (LEDs) and third generation photovoltaics (PV) to the imaging of biomolecules.

The fabrication of SiQDs with efficient photoluminescence quantum yields (PLQYs) is challenging. At the nanoscale, the surface chemistry plays an important role in the optical properties. Defects such as unpaired electrons, or dangling bonds, can significantly degrade their luminescence. Passivation of the surface dangling bonds with organic ligands or via oxidation have led to improved PLQY, with hydrosilylated, nonthermal plasma-synthesized SiQDs exhibiting PLQYs exceeding 60 %.

Enhanced thermal stability was also observed with SiQDs hydrosilylated with alkyl groups. While surface hydrides begin to desorb under 100 ^{o}C for unfunctionalized, hydrogen-terminated SiNCs, thermally-hydrosilylated SiNCs were more robust—hydrogen and alkyl desorption only began between 200 ^{o}C and 250 ^{o}C. Thus, at temperatures below 100 ^{o}C (the maximum temperature a commercial solar cell would sustain), the hydrosilylated SiQDs exhibited no permanent degradation in their optical properties.

Unfortunately, the photoluminescence of the hydrosilylated SiQDs degrade with UV exposure. UV irradiation resulted in $\sim$ 20 % (absolute) decrease in the SiQDs' PLQY, reaching a saturation of $\sim$ 40 % within 4 h. Similar to the SWE in a-Si:H, photodegradation was found to be a result of the creation of dangling bonds due to the breaking of silicon hydride bonds at the SiNC surface. These dangling bonds act as centers for

nonradiative recombination, resulting in the deterioration of the SiNCs' optical properties.

Photochemical hydrosilylation proved to be a powerful technique in creating highly luminescent, photostable SiQDs. Similar to thermal hydrosilylation, PLQYs nearing 60 % were obtained via the photochemical reactions. The photochemically-hydrosilylated SiQDs also demonstrated enhanced stability against UV irradiation, with SiQDs hydrosilylated using mercury-vapor lamp showing no degradation during exposure.

The photochemical reactions further allowed the fabrication of highly luminescent SiQDs in an all gas-phase alkylation technique to eliminate solvent waste. Alkenes were injected into the expansion region of the nonthermal plasma, where the diminished plasma intensity allows the selective dissociation of the weaker C=C bonds in the alkene. Unfortunately, a portion of the resulting alkyl radicals were simply physisorbed onto the QDs, acting as exciton trap sites. Irradiation of the QDs (with the physisorbed radicals) initiated hydrosilylation reactions, and PLQYs approaching 60 % were obtained.

The stable, highly luminescent SiQDs can be applied as luminescent downshifters (LDS) to improve photovoltaic efficiencies. A layer of dense SiQDs deposited on a heterojunction solar cell resulted in $\sim$ 25 % enhancement in EQE at 300 nm; however, an increase in surface reflection resulted in significant reduction in EQE at wavelengths above 400 nm. The application of a dual-purpose SiQD film that acted as an antireflective coating (ARC) in addition to LDS enhanced the EQE of the solar cells in the blue/UV spectrum without efficiency losses in the regions not downshifted. The effects of the SiQD ARC was most significant on cells that possessed a deficient ARC; almost 20 % improvement in EQE was observed.

For biological applications, water-soluble SiQDs are necessary. Hydrophilic SiQDs were produced by terminating the surface with amine or hydroxyl groups via radical-assisted or catalytic hydrosilylation reactions. Unfortunately, the amine and hydroxyl-terminated SiQDs only exhibited blue emission, likely from surface defects. On the other hand, microplasma-treated SiNCs demonstrated several characteristics that are highly attractive in the imaging of biomolecules: (1) efficient size-tunable luminescence, with PLQYs exceeding 50 %, was observed from water-soluble SiNCs, (2) the microplasma-treated SiNCs were high in purity—only silicon, oxygen, carbon, and hydrogen species

were detected; thus, no post-synthesis purification is needed prior to biological application, and (3) the NCs possess enhanced stability in water, which is beneficial in long-term studies of biomolecules; no degradation in PLQY was observed within the first 20 days of water dispersion.

Silicon quantum dots are highly versatile materials. Both hydrophobic and hydrophilic SiQDs that are highly luminescent and environmentally stable were fabricated in this work. Hopefully, the results shown here will bring us a step closer towards applying SiQDs in the real world.

References

[1] L. Wang and A. Zunger. Solving Schrödinger's equation around a desired energy: Application to silicon quantum dots. *J. Chem. Phys.*, 1994.

[2] A. Zunger and L. Wang. Theory of silicon nanostructures. *Appl. Surf. Sci.*, 1996.

[3] X. D. Pi, R. W. Liptak, J. Deneen Nowak, N. P. Wells, C. B. Carter, S. a. Campbell, and U. Kortshagen. Air-stable full-visible-spectrum emission from silicon nanocrystals synthesized by an all-gas-phase plasma approach. *Nanotechnology*, 2008.

[4] J.-P. Boeuf, A. Bouchoule, L. Boufendi, C. Hollenstein, J. Perrin, C. Punset, E. Stoffels, and W. Stoffels. *Dusty Plasmas: physics, chemistry and technological impacts in plasma processing.* John Wiley & Sons, 1999.

[5] L. Mangolini and U. Kortshagen. Plasma-Assisted Synthesis of Silicon Nanocrystal Inks. *Adv. Mater.*, 2007.

[6] R. J. Anthony, K.-Y. Cheng, Z. C. Holman, R. J. Holmes, and U. R. Kortshagen. An all-gas-phase approach for the fabrication of silicon nanocrystal light-emitting devices. *Nano Lett.*, 2012.

[7] W. C. W. Chan, D. J. Maxwell, X. Gao, R. E. Bailey, M. Han, and S. Nie. Luminescent quantum dots for multiplexed biological detection and imaging. *Curr. Opin. Biotechnol.*, 2002.

[8] Z. C. Holman and U. R. Kortshagen. A flexible method for depositing dense nanocrystal thin films: impaction of germanium nanocrystals. *Nanotechnology*, 2010.

[9] L. T. Canham. Silicon quantum wire array fabrication by electrochemical and chemical dissolution of wafers. *Appl. Phys. Lett.*, 1990.

[10] A. Alivisatos. Semiconductor clusters, nanocrystals, and quantum dots. *Science.*, 1996.

[11] U.S. Energy Information Administration. Annual Energy Outlook 2015. 2015.

[12] Y. Shirasaki, G. J. Supran, M. G. Bawendi, and V. Bulovic. Emergence of colloidal quantum-dot light-emitting technologies. *Nat. Photonics*, 2013.

[13] K.-Y. Cheng, R. Anthony, U. R. Kortshagen, and R. J. Holmes. Hybrid silicon nanocrystal-organic light-emitting devices for infrared electroluminescence. *Nano Lett.*, 2010.

[14] K.-Y. Cheng, R. Anthony, U. R. Kortshagen, and R. J. Holmes. High-efficiency silicon nanocrystal light-emitting devices. *Nano Lett.*, 2011.

[15] B. Mashford, M. Stevenson, Z. Popovic, C. Hamilton, Z. Zhou, C. Breen, J. Steckel, V. Bulovic, M. Bawendi, S. Coe-Sullivan, and P. T. Kazlas. High-efficiency quantum-dot light-emitting devices with enhanced charge injection. *Nat. Photonics*, 2013.

[16] United Nations Framework Convention on Climate Change. The need for strong global action on climate change. 2011.

[17] Renewable Energy Policy Network for the 21st Century. Renewables 2014: Global Status Report. 2014.

[18] International Renewable Energy Agency. Renewable Power Generation Costs in 2014. 2014.

[19] M. C. Hanna and A. J. Nozik. Solar conversion efficiency of photovoltaic and photoelectrolysis cells with carrier multiplication absorbers. *J. Appl. Phys.*, 2006.

[20] M. C. Beard, K. P. Knutsen, P. Yu, J. M. Luther, Q. Song, W. K. Metzger, R. J. Ellingson, and A. J. Nozik. Multiple exciton generation in colloidal silicon nanocrystals. *Nano Lett.*, 2007.

[21] L. Danos, T. Parel, T. Markvart, V. Barrioz, W. Brooks, and S. Irvine. Increased efficiencies on CdTe solar cells via luminescence down-shifting with excitation energy transfer between dyes. *Sol. Energy Mater. Sol. Cells*, 2012.

[22] V. Svrcek. Ex situ prepared Si nanocrystals embedded in silica glass: Formation and characterization. *J. Appl. Phys.*, 2004.

[23] Z. Yuan, G. Pucker, A. Marconi, F. Sgrignuoli, A. Anopchenko, Y. Jestin, L. Ferrario, P. Bellutti, and L. Pavesi. Silicon nanocrystals as a photoluminescence down shifter for solar cells. *Sol. Energy Mater. Sol. Cells*, 2011.

[24] J. M. Luther, M. C. Beard, Q. Song, M. Law, R. J. Ellingson, and A. J. Nozik. Multiple exciton generation in films of electronically coupled PbSe quantum dots. *Nano Lett.*, 2007.

[25] M. Trinh, A. Houtepen, and J. Schins. In spite of recent doubts carrier multiplication does occur in PbSe nanocrystals. *Nano Lett.*, 2008.

[26] M. C. Beard, A. G. Midgett, M. Law, O. E. Semonin, R. J. Ellingson, and A. J. Nozik. Variations in the quantum efficiency of multiple exciton generation for a series of chemically treated PbSe nanocrystal films. *Nano Lett.*, 2009.

[27] M. Ji, S. Park, S. T. Connor, T. Mokari, Y. Cui, and K. J. Gaffney. Efficient multiple exciton generation observed in colloidal PbSe quantum dots with temporally and spectrally resolved intraband excitation. *Nano Lett.*, 2009.

[28] M. T. Trinh, L. Polak, J. M. Schins, A. J. Houtepen, R. Vaxenburg, G. I. Maikov, G. Grinbom, A. G. Midgett, J. M. Luther, M. C. Beard, A. J. Nozik, M. Bonn, E. Lifshitz, and L. D. A. Siebbeles. Anomalous independence of multiple exciton generation on different group IV-VI quantum dot architectures. *Nano Lett.*, 2011.

[29] R. D. Schaller, M. Sykora, J. M. Pietryga, and V. I. Klimov. Seven excitons at a cost of one: redefining the limits for conversion efficiency of photons into charge carriers. *Nano Lett.*, 2006.

[30] R. Ellingson. Slicing and dicing photons. *Nat. Photonics*, 2008.

[31] J. A. McGuire, M. Sykora, J. Joo, J. M. Pietryga, and V. I. Klimov. Apparent versus true carrier multiplication yields in semiconductor nanocrystals. *Nano Lett.*, 2010.

[32] G. Nair, L.-Y. Chang, S. M. Geyer, and M. G. Bawendi. Perspective on the prospects of a carrier multiplication nanocrystal solar cell. *Nano Lett.*, 2011.

[33] D. Timmerman, J. Valenta, K. Dohnalová, W. D. A. M. de Boer, and T. Gregorkiewicz. Step-like enhancement of luminescence quantum yield of silicon nanocrystals. *Nat. Nanotechnol.*, 2011.

[34] M. T. Trinh, R. Limpens, W. D. A. M. de Boer, J. M. Schins, L. D. A. Siebbeles, and T. Gregorkiewicz. Direct generation of multiple excitons in adjacent silicon nanocrystals revealed by induced absorption. *Nat. Photonics*, 2012.

[35] M. C. Beard, A. G. Midgett, M. C. Hanna, J. M. Luther, B. K. Hughes, and A. J. Nozik. Comparing multiple exciton generation in quantum dots to impact ionization in bulk semiconductors: implications for enhancement of solar energy conversion. *Nano Lett.*, 2010.

[36] C. M. Niemeyer. Nanoparticles, proteins, and nucleic acids: biotechnology meets materials science. *Angew. Chemie Int. Ed.*, 2001.

[37] V. Ntziachristos. Fluorescence molecular imaging. *Annu. Rev. Biomed. Eng.*, 2006.

[38] D. M. Chudakov, M. V. Matz, S. Lukyanov, and K. A. Lukyanov. Fluorescent Proteins and Their Applications in Imaging Living Cells and Tissues. *Physiol. Rev.*, 2010.

[39] T. Jamieson, R. Bakhshi, D. Petrova, R. Pocock, M. Imani, and A. M. Seifalian. Biological applications of quantum dots. *Biomaterials*, 2007.

[40] U. Resch-Genger, M. Grabolle, S. Cavaliere-Jaricot, R. Nitschke, and T. Nann. Quantum dots versus organic dyes as fluorescent labels. *Nat. Methods*, 2008.

[41] W. C. Chan and S. Nie. Quantum dot bioconjugates for ultrasensitive nonisotopic detection. *Science.*, 1998.

[42] X. Michalet, F. F. Pinaud, L. A. Bentolila, J. M. Tsay, S. Doose, J. J. Li, G. Sundaresan, A. M. Wu, S. S. Gambhir, and S. Weiss. Quantum Dots for Live Cells, in Vivo Imaging, and Diagnostics. *Science.*, 2005.

[43] R. Anthony and U. Kortshagen. Photoluminescence quantum yields of amorphous and crystalline silicon nanoparticles. *Phys. Rev. B*, 2009.

[44] R. K. Baldwin, K. A. Pettigrew, J. C. Garno, P. P. Power, G.-y. Liu, and S. M. Kauzlarich. Room temperature solution synthesis of alkyl-capped tetrahedral shaped silicon nanocrystals. *J. Am. Chem. Soc.*, 2002.

[45] Z. Ding, B. M. Quinn, S. K. Haram, L. E. Pell, B. A. Korgel, and A. J. Bard. Electrochemistry and electrogenerated chemiluminescence from silicon nanocrystal quantum dots. *Science.*, 2002.

[46] K. Pettigrew, Q. Liu, P. Philip, and S. Kauzlarich. Solution synthesis of alkyl-and alkyl/alkoxy-capped silicon nanoparticles via oxidation of Mg2Si. *Chem. Mater.*, 2003.

[47] J. P. Wilcoxon and G. A. Samara. Tailorable, visible light emission from silicon nanocrystals. *Appl. Phys. Lett.*, 1999.

[48] A. Onischuk, A. Levykin, and V. Strunin. Aerosol formation under heterogeneous/homogeneous thermal decomposition of silane: experiment and numerical modeling. *J. Aerosol Sci.*, 2000.

[49] K. Littau, P. Szajowski, A. Muller, A. Kortan, and L. Brus. A luminescent silicon nanocrystal colloid via a high-temperature aerosol reaction. *J. Phys. Chem.*, 1993.

[50] F. Huisken, D. Amans, G. Ledoux, H. Hofmeister, F. Cichos, and J. Martin. Nanostructuration with visible-light-emitting silicon nanocrystals. *New J. Phys.*, 2003.

[51] P. Batson and J. Heath. Electron energy loss spectroscopy of single silicon nanocrystals: The conduction band. *Phys. Rev. Lett.*, 1993.

[52] L. Mangolini, E. Thimsen, and U. Kortshagen. High-yield plasma synthesis of luminescent silicon nanocrystals. *Nano Lett.*, 2005.

[53] M. A. Lieberman and A. J. Lichtenberg. *Principles of Plasma Discharges and Materials Processing.* John Wiley & Sons, New Jersey, 2005.

[54] A. J. Wagner, C. Anderson, J. N. Trask, L. Cui, A. Chov, K. A. Mkhoyan, and U. R. Kortshagen. Propagating nanocavity-enhanced rapid crystallization of silicon thin films. *Nano Lett.*, 2013.

[55] U. Kortshagen. Nonthermal plasma synthesis of semiconductor nanocrystals. *J. Phys. D. Appl. Phys.*, 2009.

[56] D. Mukherjee, C. G. Sonwane, and M. R. Zachariah. Kinetic Monte Carlo simulation of the effect of coalescence energy release on the size and shape evolution of nanoparticles grown as an aerosol. *J. Chem. Phys.*, 2003.

[57] J. E. Allen, B. M. Annaratone, and U. de Angelis. On the orbital motion limited theory for a small body at floating potential in a Maxwellian plasma. *J. Plasma Phys.*, 2000.

[58] S. Ratynskaia, S. Khrapak, A. Zobnin, M. Thoma, M. Kretschmer, A. Usachev, V. Yaroshenko, R. Quinn, G. Morfill, O. Petrov, and V. Fortov. Experimental Determination of Dust-Particle Charge in a Discharge Plasma at Elevated Pressures. *Phys. Rev. Lett.*, 2004.

[59] M. Lampe, V. Gavrishchaka, G. Ganguli, and G. Joyce. Effect of Trapped Ions on Shielding of a Charged Spherical Object in a Plasma. *Phys. Rev. Lett.*, 2001.

[60] S. Khrapak, S. Ratynskaia, A. Zobnin, A. Usachev, V. Yaroshenko, M. Thoma, M. Kretschmer, H. Höfner, G. Morfill, O. Petrov, and V. Fortov. Particle charge in the bulk of gas discharges. *Phys. Rev. E*, 2005.

[61] J. Goree. Ion trapping by a charged dust grain in a plasma. *Phys. Rev. Lett.*, 1992.

[62] J. Goree. Charging of particles in a plasma. *Plasma Sources Sci. Technol.*, 1994.

[63] M. Gatti and U. Kortshagen. Analytical model of particle charging in plasmas over a wide range of collisionality. *Phys. Rev. E*, 2008.

[64] P. Belenguer, J. Blondeau, L. Boufendi, M. Toogood, A. Plain, A. Bouchoule, C. Laure, and J. Boeuf. Numerical and experimental diagnostics of rf discharges in pure and dusty argon. *Phys. Rev. A*, 1992.

[65] A. Bouchoule, A. Plain, L. Boufendi, J. P. Blondeau, and C. Laure. Particle generation and behavior in a silane-argon low-pressure discharge under continuous or pulsed radio-frequency excitation. *J. Appl. Phys.*, 1991.

[66] A. Bouchoule and L. Boufendi. Particulate formation and dusty plasma behaviour in argon-silane RF discharge. *Plasma Sources Sci. Technol.*, 1993.

[67] L. Boufendi, A. Plain, J. P. Blondeau, A. Bouchoule, C. Laure, and M. Toogood. Measurements of particle size kinetics from nanometer to micrometer scale in a low-pressure argon-silane radio-frequency discharge. *Appl. Phys. Lett.*, 1992.

[68] S. K. Friedlander. *Smoke, Dust, and Haze*. Oxford University Press, New York, 2000.

[69] A. A. Howling, L. Sansonnens, J. Dorier, and C. Hollenstein. Time-resolved measurements of highly polymerized negative ions in radio frequency silane plasma deposition experiments. *J. Appl. Phys.*, 1994.

[70] C. Courteille, J.-L. Dorier, and C. Hollenstein. Partial-depth modulation study of anions and neutrals in low-pressure silane plasmas. *Plasma Sources Sci. Technol.*, 1996.

[71] L. Boufendi and A. Bouchoule. Particle nucleation and growth in a low-pressure argon-silane discharge. *Plasma Sources Sci. Technol.*, 1994.

[72] U. Kortshagen and U. Bhandarkar. Modeling of particulate coagulation in low pressure plasmas. *Phys. Rev. E*, 1999.

[73] U. R. Kortshagen, U. V. Bhandarkar, M. T. Swihart, and S. L. Girshick. Generation and growth of nanoparticles in low-pressure plasmas. *Pure Appl. Chem.*, 1999.

[74] M. Hirasawa, T. Orii, and T. Seto. Size-dependent crystallization of Si nanoparticles. *Appl. Phys. Lett.*, 2006.

[75] A. Bapat, M. Gatti, Y.-P. Ding, S. A. Campbell, and U. Kortshagen. A plasma process for the synthesis of cubic-shaped silicon nanocrystals for nanoelectronic devices. *J. Phys. D. Appl. Phys.*, 2007.

[76] L. Mangolini and U. Kortshagen. Selective nanoparticle heating: Another form of nonequilibrium in dusty plasmas. *Phys. Rev. E*, 2009.

[77] E. Roduner. Size matters: why nanomaterials are different. *Chem. Soc. Rev.*, 2006.

[78] C. Delerue, G. Allan, and M. Lannoo. Theoretical aspects of the luminescence of porous silicon. *Phys. Rev. B*, 1993.

[79] G. Allan, C. Delerue, and M. Lannoo. Nature of Luminescent Surface States of Semiconductor Nanocrystallites. *Phys. Rev. Lett.*, 1996.

[80] H. Fu and A. Zunger. InP quantum dots: Electronic structure, surface effects, and the redshifted emission. *Phys. Rev. B*, 1997.

[81] V. Klimov, D. McBranch, C. Leatherdale, and M. Bawendi. Electron and hole relaxation pathways in semiconductor quantum dots. *Phys. Rev. B*, 1999.

[82] M. P. Stewart and J. M. Buriak. Photopatterned Hydrosilylation on Porous Silicon. *Angew. Chemie Int. Ed.*, 1998.

[83] D. Jurbergs, E. Rogojina, L. Mangolini, and U. Kortshagen. Silicon nanocrystals with ensemble quantum yields exceeding 60%. *Appl. Phys. Lett.*, 2006.

[84] R. W. Liptak, B. Devetter, J. H. Thomas, U. Kortshagen, and S. A. Campbell. SF6 plasma etching of silicon nanocrystals. *Nanotechnology*, 2009.

[85] J. A. Kelly and J. G. C. Veinot. An investigation into near-UV hydrosilylation of freestanding silicon nanocrystals. *ACS Nano*, 2010.

[86] J. M. Buriak, M. P. Stewart, T. W. Geders, M. J. Allen, H. C. Choi, J. Smith, D. Raftery, and L. T. Canham. Lewis Acid Mediated Hydrosilylation on Porous Silicon Surfaces. *J. Am. Chem. Soc.*, 1999.

[87] A. B. Sieval, A. L. Demirel, J. W. M. Nissink, M. R. Linford, J. H. van der Maas, W. H. de Jeu, H. Zuilhof, and E. J. R. Sudhölter. Highly Stable Si-C Linked Functionalized Monolayers on the Silicon (100) Surface. *Langmuir*, 1998.

[88] M. Sung, G. Kluth, and O. Yauw. Thermal Behavior of Alkyl Monolayers on Silicon Surfaces. *Langmuir*, 1997.

[89] R. W. Liptak, J. Yang, N. J. Kramer, U. Kortshagen, and S. A. Campbell. Environmental photostability of SF6-etched silicon nanocrystals. *Nanotechnology*, 2012.

[90] J. Yang, R. Liptak, D. Rowe, J. Wu, J. Casey, D. Witker, S. A. Campbell, and U. Kortshagen. UV and air stability of high-efficiency photoluminescent silicon nanocrystals. *Appl. Surf. Sci.*, 2014.

[91] D. A. Hines and P. V. Kamat. Recent advances in quantum dot surface chemistry. *ACS Appl. Mater. Interfaces*, 2014.

[92] Z. F. Li and E. Ruckenstein. Water-soluble poly(acrylic acid) grafted luminescent silicon nanoparticles and their use as fluorescent biological staining labels. *Nano Lett.*, 2004.

[93] J. H. Warner, A. Hoshino, K. Yamamoto, and R. D. Tilley. Water-Soluble Photoluminescent Silicon Quantum Dots. *Angew. Chemie*, 2005.

[94] Z. Kang, Y. Liu, C. H. A. Tsang, D. D. D. Ma, X. Fan, N. B. Wong, and S.-T. Lee. Water-soluble silicon quantum dots with wavelength-tunable photoluminescence. *Adv. Mater.*, 2009.

[95] J. Wang, Y. Liu, F. Peng, C. Chen, Y. He, H. Ma, L. Cao, and S. Sun. A General Route to Efficient Functionalization of Silicon Quantum Dots for High-Performance Fluorescent Probes. *Small*, 2012.

[96] J. Holm and J. T. Roberts. Thermal oxidation of 6 nm aerosolized silicon nanoparticles: size and surface chemistry changes. *Langmuir*, 2007.

[97] M. R. Linford, P. Fenter, P. M. Eisenberger, and C. E. D. Chidsey. Alkyl Monolayers on Silicon Prepared from 1-Alkenes and Hydrogen-Terminated Silicon. *J. Am. Chem. Soc.*, 1995.

[98] R. Boukherroub, S. Morin, D. D. M. Wayner, F. Bensebaa, G. I. Sproule, J.-M. Baribeau, and D. J. Lockwood. Ideal Passivation of Luminescent Porous Silicon by Thermal, Noncatalytic Reaction with Alkenes and Aldehydes. *Chem. Mater.*, 2001.

[99] R. Boukherroub, S. Morin, F. Bensebaa, and D. D. M. Wayner. New Synthetic Routes to Alkyl Monolayers on the Si(111) Surface. *Langmuir*, 1999.

[100] F. Hua, M. T. Swihart, and E. Ruckenstein. Efficient surface grafting of luminescent silicon quantum dots by photoinitiated hydrosilylation. *Langmuir*, 2005.

[101] J. M. Buriak. Organometallic chemistry on silicon and germanium surfaces. *Chem. Rev.*, 2002.

[102] A. B. Sieval, B. van den Hout, H. Zuilhof, and E. J. Sudhölter. Molecular modeling of covalently attached alkyl monolayers on the hydrogen-terminated Si(111) surface. *Langmuir*, 2001.

[103] J. M. Buriak. Illuminating Silicon Surface Hydrosilylation: An Unexpected Plurality of Mechanisms. *Chem. Mater.*, 2014.

[104] P. Gupta, V. Colvin, and S. George. Hydrogen desorption kinetics from monohydride and dihydride species on silicon surfaces. *Phys. Rev. B*, 1988.

[105] J. J. Boland. Role of bond-strain in the chemistry of hydrogen on the Si(100) surface. *Surf. Sci.*, 1992.

[106] X. Wang, R. E. Ruther, J. A. Streifer, and R. J. Hamers. UV-Induced Grafting of Alkenes to Silicon Surfaces: Photoemission versus Excitons. *J. Am. Chem. Soc.*, 2010.

[107] L. A. Huck and J. M. Buriak. Toward a mechanistic understanding of exciton-mediated hydrosilylation on nanocrystalline silicon. *J. Am. Chem. Soc.*, 2012.

[108] R. W. Liptak, S. A. Campbell, and U. Kortshagen. Surface chemistry dependence of native oxidation formation on silicon nanocrystals. *J. Appl. Phys.*, 2009.

[109] P. Mutti, G. Ghislotti, S. Bertoni, L. Bonoldi, G. Cerofolini, L. Meda, E. Grilli, and M. Guzzi. Room-temperature visible luminescence from silicon nanocrystals in silicon implanted SiO2 layers. *Appl. Phys. Lett.*, 1995.

[110] M. L. Brongersma, A. Polman, K. S. Min, E. Boer, T. Tambo, and H. A. Atwater. Tuning the emission wavelength of Si nanocrystals in SiO2 by oxidation. *Appl. Phys. Lett.*, 1998.

[111] V. Maurice, I. Rivolta, J. Vincent, and O. Raccurt. Silica encapsulation of luminescent silicon nanoparticles: stable and biocompatible nanohybrids. *J. Nanoparticle*, 2012.

[112] D. Mariotti, V. Švrček, J. W. J. Hamilton, M. Schmidt, and M. Kondo. Silicon Nanocrystals in Liquid Media: Optical Properties and Surface Stabilization by Microplasma-Induced Non-Equilibrium Liquid Chemistry. *Adv. Funct. Mater.*, 2012.

[113] S. Mitra, V. Švrček, D. Mariotti, T. Velusamy, K. Matsubara, and M. Kondo. Microplasma-Induce Liquid Chemistry for Stabilizing of Silicon Nanocrystals Optical Properties in Water. *Plasma Process. Polym.*, 2014.

[114] V. Svrcek, A. Slaoui, and J.-C. Muller. Silicon nanocrystals as light converter for solar cells. *Thin Solid Films*, 2004.

[115] S. Godefroo, M. Hayne, M. Jivanescu, A. Stesmans, M. Zacharias, O. I. Lebedev, G. Van Tendeloo, and V. V. Moshchalkov. Classification and control of the origin of photoluminescence from Si nanocrystals. *Nat. Nanotechnol.*, 2008.

[116] L. Mangolini, D. Jurbergs, E. Rogojina, and U. Kortshagen. High efficiency photoluminescence from silicon nanocrystals prepared by plasma synthesis and organic surface passivation. *Phys. Status Solidi*, 2006.

[117] M. Wolkin, J. Jorne, P. Fauchet, G. Allan, and C. Delerue. Electronic States and

Luminescence in Porous Silicon Quantum Dots: The Role of Oxygen. *Phys. Rev. Lett.*, 1999.

[118] M. A. Tischler, R. T. Collins, J. H. Stathis, and J. C. Tsang. Luminescence degradation in porous silicon. *Appl. Phys. Lett.*, 1992.

[119] J. Harper. Photoluminescence quenching and the photochemical oxidation of porous silicon by molecular oxygen. *Langmuir*, 1997.

[120] M. Stutzmann, W. Jackson, and C. Tsai. Light-induced metastable defects in hydrogenated amorphous silicon: A systematic study. *Phys. Rev. B*, 1985.

[121] H. Fritzsche. Photo-induced structural changes associated with the Staebler-Wronski effect in hydrogenation amorphous silicon. *Solid State Commun.*, 1995.

[122] H. Fritzsche. Development in the understanding and controlling the Staebler-Wronski effect in a-Si:H. *Annu. Rev. Mater. Res.*, 2001.

[123] H. Dersch. Light-induced dangling bonds in hydrogenated amorphous silicon. *Appl. Phys. Lett.*, 1981.

[124] R. Pereira, D. Rowe, R. Anthony, and U. Kortshagen. Oxidation of freestanding silicon nanocrystals probed with electron spin resonance of interfacial dangling bonds. *Phys. Rev. B*, 2011.

[125] R. N. Pereira, D. J. Rowe, R. J. Anthony, and U. Kortshagen. Freestanding silicon nanocrystals with extremely low defect content. *Phys. Rev. B*, 2012.

[126] D. Pierreux and A. Stesmans. Frequency-dependent electron spin resonance study of Pb-type interface defects in thermal Si/SiO2. *Phys. Rev. B*, 2002.

[127] A. Kołodziej. Staebler-Wronski effect in amorphous silicon and its alloys. *Opto-electronics Rev.*, 2004.

[128] M. Niwano, M. Terashi, and J. Kuge. Hydrogen adsorption and desorption on Si(100) and Si(111) surfaces investigated by in situ surface infrared spectroscopy. *Surf. Sci.*, 1999.

[129] S. King, R. Davis, and R. Nemanich. Hydrogen desorption kinetics and band bending for 6H–SiC(0001) surfaces. *Surf. Sci.*, 2009.

[130] D. Marra, E. Edelberg, R. Naone, and E. Aydil. Silicon hydride composition of plasma-deposited hydrogenated amorphous and nanocrystalline silicon films and surfaces. *J. Vac. Sci. Technol. A Vacuum, Surfaces, Film.*, 1998.

[131] W. Beyer. Determination of the hydrogen diffusion coefficient in hydrogenated amorphous silicon from hydrogen effusion experiments. *J. Appl. Phys.*, 1982.

[132] M. Wise, B. Koehler, P. Gupta, P. Coon, and S. George. Comparison of hydrogen desorption kinetics from Si(111) 7×7 and Si(100) 2×1. *Surf. Sci.*, 1991.

[133] A. Pusel, U. Wetterauer, and P. Hess. Photochemical Hydrogen Desorption from H-Terminated Silicon(111) by VUV Photons. *Phys. Rev. Lett.*, 1998.

[134] L. Ruizendaal, S. Bhattacharjee, K. Pournazari, M. Rosso-Vasic, L. H. J. de Haan, G. M. Alink, A. T. M. Marcelis, and H. Zuilhof. Synthesis and cytotoxicity of silicon nanoparticles with covalently attached organic monolayers. *Nanotoxicology*, 2009.

[135] A. J. Nozik. Multiple exciton generation in semiconductor quantum dots. *Chem. Phys. Lett.*, 2008.

[136] M. C. Beard, J. M. Luther, O. E. Semonin, and A. J. Nozik. Third generation photovoltaics based on multiple exciton generation in quantum confined semiconductors. *Acc. Chem. Res.*, 2013.

[137] F. A. Reboredo, E. Schwegler, and G. Galli. Optically Activated Functionalization Reactions in Si Quantum Dots. *J. Am. Chem. Soc.*, 2003.

[138] X. Wang, P. E. Colavita, J. a. Streifer, J. E. Butler, and R. J. Hamers. Photochemical grafting of alkenes onto carbon surfaces: Identifying the roles of electrons and holes. *J. Phys. Chem. C*, 2010.

[139] A. M. P. Botas, R. A. Ferreira, R. N. Pereira, R. J. Anthony, T. Moura, D. J. Rowe, and U. R. Kortshagen. High Quantum Yield Dual-emission from Gas Phase Grown Crystalline Si Nanoparticles. *J. Phys. Chem. C*, 2014.

[140] S. Prokes, O. Glembocki, V. Bermudez, R. Kaplan, L. Friedersdorf, and P. Searson. SiHx excitation: An alternate mechanism for porous Si photoluminescence. *Phys. Rev. B*, 1992.

[141] M. A. Green and M. J. Keevers. Optical properties of intrinsic silicon at 300 K. *Prog. Photovoltaics Res. Appl.*, 1995.

[142] H. Ibach, H. D. Bruchmann, and H. Wagner. Vibrational study of the initial stages of the oxidation of Si(111) and Si(100) surfaces. *Appl. Phys. A*, 1982.

[143] M. Morita, T. Ohmi, E. Hasegawa, M. Kawakami, and M. Ohwada. Growth of native oxide on a silicon surface. *J. Appl. Phys.*, 1990.

[144] G. Cerofolini and L. Meda. Mechanisms and kinetics of room-temperature silicon oxidation. *J. Non. Cryst. Solids*, 1997.

[145] B. O. Dabbousi, M. Bawendi, O. Onitsuka, and M. F. Rubner. Electroluminescence from CdSe quantum-dot / polymer composites. *Appl. Phys. Lett.*, 1995.

[146] Y. Liu, M. Gibbs, C. L. Perkins, J. Tolentino, M. H. Zarghami, J. Bustamante, and M. Law. Robust, functional nanocrystal solids by infilling with atomic layer deposition. *Nano Lett.*, 2011.

[147] R. L. Cicero, M. R. Linford, and C. E. D. Chidsey. Photoreactivity of Unsaturated Compounds with Hydrogen-Terminated Silicon(111). *Langmuir*, 2000.

[148] M. Woods, S. Carlsson, Q. Hong, S. N. Patole, L. H. Lie, A. Houlton, and B. R. Horrocks. A kinetic model of the formation of organic monolayers on hydrogen-terminated silicon by hydrosilation of alkenes. *J. Phys. Chem. B*, 2005.

[149] S. Calder, A. Boies, P. Lei, S. Girshick, and J. Roberts. Photo-Assisted Hydrosilylation of Silicon Nanoparticles: Dependence of Particle Size on Grafting Chemistry. *Chem. Mater.*, 2011.

[150] P. E. Colavita, B. Sun, K. Y. Tse, and R. J. Hamers. Photochemical grafting of n-alkenes onto carbon surfaces: The role of photoelectron ejection. *J. Am. Chem. Soc.*, 2007.

[151] H. Deutsch, H. Kersten, S. Klagge, and A. Rutscher. On the temperature dependence of plasma polymerization. *Contrib. to Plasma Phys.*, 1988.

[152] H. Kersten and G. M. W. Kroesen. On the temperature dependence of the deposition rate of amorphous, hydrogenated carbon films. *J. Vac. Sci. Technol. A*, 1990.

[153] A. von Keudell and W. Möller. A combined plasma-surface model for the deposition of C:H films from a methane plasma. *J. Appl. Phys.*, 1994.

[154] C. A. J. van Gils, S. Hofmann, B. K. H. L. Boekema, R. Brandenburg, and P. J. Bruggeman. Mechanisms of bacterial inactivation in the liquid phase induced by a remote RF cold atmospheric pressure plasma jet. *J. Phys. D. Appl. Phys.*, 2013.

[155] R. J. Hunter. *Zeta potential in colloid science: Principles and applications*. Academic Press, 1988.

[156] A. Bieder, A. Gruniger, and P. R. von Rohr. Deposition of SiOx diffusion barriers on flexible packaging materials by PECVD. *Surf. Coatings Technol.*, 2005.

[157] B. E. Deal and A. S. Grove. General relationship for the thermal oxidation of silicon. *J. Appl. Phys.*, 1965.

[158] M. Tomozawa. Water Diffusion in Silica Glass and Wet Oxidation of Si: An Interpretation for the High Speed of Wet Oxidation. *J. Electrochem. Soc.*, 2011.

[159] N. Srivastava and C. Wang. Effects of water addition on OH radical generation and plasma properties in an atmospheric argon microwave plasma jet. *J. Appl. Phys.*, 2011.

[160] T. Verreycken, R. Mensink, R. V. D. Horst, N. Sadeghi, and P. J. Bruggeman. Absolute OH density measurements in the effluent of a cold atmospheric-pressure Ar–H2O RF plasma jet in air. *Plasma Sources Sci. Technol.*, 2013.

[161] S. Zhang, W. van Gaens, B. van Gessel, S. Hofmann, E. van Veldhuizen, A. Bogaerts, and P. Bruggeman. Spatially resolved ozone densities and gas temperatures in a time modulated RF driven atmospheric pressure plasma jet: an analysis of the production and destruction mechanisms. *J. Phys. D. Appl. Phys.*, 2013.

[162] K. Wende, P. Williams, J. Dalluge, W. V. Gaens, H. Aboubakr, J. Bischof, T. von Woedtke, S. M. Goyal, K.-D. Weltmann, A. Bogaerts, K. Masur, and P. J. Bruggeman. Identification of the biologically active liquid chemistry induced by a non-thermal atmospheric pressure plasma jet. *Biointerphases*, 2015.

[163] C. E. Melton. Cross Sections and Interpretation of Dissociative Attachment Reactions Producing OH, O, and H in H2O. *J. Chem. Phys.*, 1972.

[164] R. Ono and T. Oda. Measurement of hydroxyl radicals in an atmospheric pressure discharge plasma by using laser-induced fluorescence. In *Ind. Appl. Conf. 1998. Thirty-Third IAS Annu. Meet. 1998 IEEE*, 1998.

[165] B. R. Locke and K.-Y. Shih. Review of the methods to form hydrogen peroxide in electrical discharge plasma with liquid water. *Plasma Sources Sci. Technol.*, 2011.

[166] J. F. M. van Rens, J. T. Schoof, F. C. Ummelen, D. C. van Vugt, P. J. Bruggeman, and E. M. van Veldhuizen. Induced Liquid Phase Flow by RF Ar Cold Atmospheric Pressure Plasma Jet. In *IEEE Trans. Plasma Sci.*, volume 42, 2014.

[167] M. L. Kremer. The Fenton reaction. Dependence of the rate on pH. *J. Phys. Chem. A*, 2003.

[168] J. Rimstidt and H. Barnes. The kinetics of silica-water reactions. *Geochim. Cosmochim. Acta*, 1980.

[169] P. V. Brady and J. V. Walther. Kinetics of quartz dissolution at low temperatures. *Chem. Geol.*, 1990.

[170] Y. Chabal. Hydride formation on the Si(100):H2O surface. *Phys. Rev. B*, 1984.

[171] J. Zhao, A. Wang, P. Altermatt, and M. A. Green. Twenty-four percent efficient silicon solar cells with double layer antireflection coatings and reduced resistance loss. *Appl. Phys. Lett.*, 1995.

[172] J. Zhao, A. Wang, M. A. Green, and F. Ferrazza. 19.8% efficient "honeycomb" textured multicrystalline and 24.4% monocrystalline silicon solar cells. *Appl. Phys. Lett.*, 1998.

[173] S. Strehlke, S. Bastide, and C. Lévy-Clément. Optimization of porous silicon reflectance for silicon photovoltaic cells. *Sol. Energy Mater. Sol. Cells*, 1999.

[174] S. Strehlke, S. Bastide, J. Guillet, and C. Levyclement. Design of porous silicon antireflection coatings for silicon solar cells. *Mater. Sci. Eng. B*, 2000.

[175] K. L. Chopra. *Thin Film Phenomena*. McGraw-Hill, 1969.

[176] A. Feldman, E. N. Farabaugh, W. K. Haller, D. M. Sanders, and R. A. Stempniak. Modifying structure and properties of optical films by coevaporation. *J. Vac. Sci. Technol. A Vacuum, Surfaces, Film.*, 1986.

[177] W. Shockley and H. J. Queisser. Detailed Balance Limit of Efficiency of p-n Junction Solar Cells. *J. Appl. Phys.*, 1961.

[178] T. Tiedje, E. Yablonovitch, G. Cody, and B. Brooks. Limiting efficiency of silicon solar cells. *IEEE Trans. Electron Devices*, 1984.

[179] C. Strumpel, M. McCann, G. Beaucarne, V. Arkhipov, A. Slaoui, V. Svrcek, C. Delcanizo, and I. Tobias. Modifying the solar spectrum to enhance silicon solar cell efficiency—An overview of available materials. *Sol. Energy Mater. Sol. Cells*, 2007.

[180] J. Kurtin. Improved Solar Cell Efficiency Through the Use of an Additive Nanostructure-Based Optical Downshifter: Final Subcontract Report. Technical Report May, 2011.

[181] V. Svrcek, A. Slaoui, and J. Muller. Silicon nanocrystals-a luminescence convertor applied to silicon solar cells. In *Proc. 3rd World Conf. Photovolt. Energy Convers.*, volume 3, pages 2734 – 2737. 2003.

[182] F. Sgrignuoli, G. Paternoster, A. Marconi, P. Ingenhoven, A. Anopchenko, G. Pucker, and L. Pavesi. Modeling of silicon nanocrystals based down-shifter for enhanced silicon solar cell performance. *J. Appl. Phys.*, 2012.

[183] F. Meinardi, A. Colombo, K. A. Velizhanin, R. Simonutti, M. Lorenzon, L. Beverina, R. Viswanatha, V. I. Klimov, and S. Brovelli. Large-area luminescent

solar concentrators based on 'Stokes-shift-engineered' nanocrystals in a mass-polymerized PMMA matrix. *Nat. Photonics*, 2014.

Appendix A

Ellipsometry

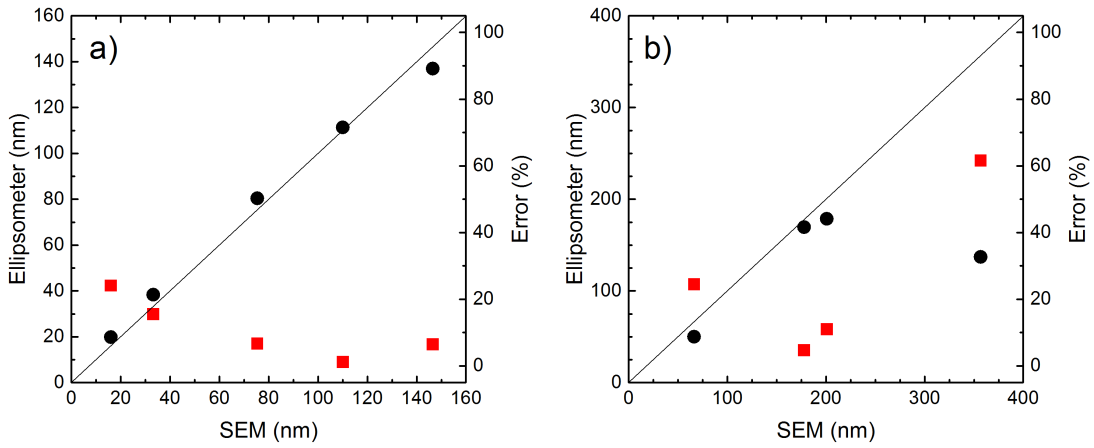

Figure A.1: Fitting accuracy of Bruggeman effective medium approach (BEMA) for thicknesses of (a) spin-cast films and (b) impacted films.

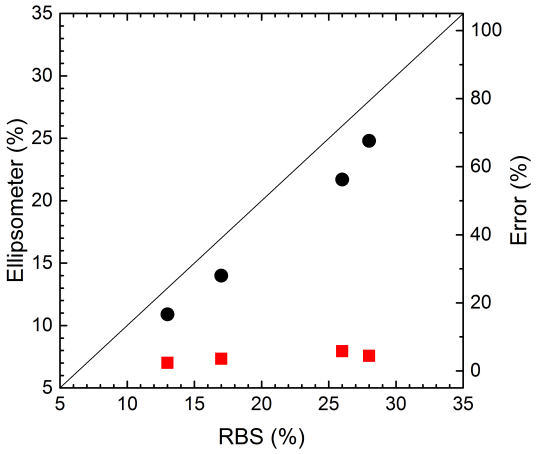

Figure A.2: Fitting accuracy of BEMA for density measurements.